5-2016

Light Echoes and Late-Time Emissions of Type IA Supernovae

Dina Drozdov
Clemson University, ddrozdo@g.clemson.edu

Light Echoes and Late-Time Emissions of Type Ia Supernovae

A Dissertation
Presented to
the Graduate School of
Clemson University

In Partial Fulfillment
of the Requirements for the Degree
Doctorate of Philosophy
Physics

---

by
Dina Drozdov
May 2015

Accepted by:
Dr. Mark D. Leising, Committee Chair
Dr. Dieter Hartmann
Dr. Jeremy King
Dr. Catalina Marinescu

Abstract

Type Ia supernovae have many applications in astronomy, yet with fundamental properties still not fully understood, new methods for investigating the environment of a supernova need to be developed. A light echo is produced from the scattering of light from a bright source and can be used to analyze the dust in the vicinity of the supernova and learn invaluable information about the source. These techniques can put constraints on explosion and progenitor models. Although light echo detections from Type Ia supernovae are rare, with only seven total extragalactic detections, this could be due to the lack of thorough late-epoch monitoring. Since key information is determined from even a single light echo detection, light echo searches should be undertaken in the future to supplement our understanding of supernovae.

As part of our collaborative campaign for studying the emission of supernovae at late epochs, we have added two light echoes to a small sample size of Type Ia supernova light echo detections: SN 2009ig in NGC 1015 and a dual echo from SN 2007af in NGC 5584. Both echoes were observed with the *Hubble Space Telescope* and allow for the most detailed images of Type Ia supernova light echoes to date. Three filters (F555W, F814W, and F350LP) captured the echoes obtained with the *Wide Field Camera 3*, and since both host galaxies were imaged as part of the same observing program, these cases will be the best comparable light echo pairs. We also further investigate the light echoes from SN 2006X in NGC 4321 and SN 1998bu in NGC 3368 from *Hubble Space Telescope* archival images.

Analyses performed on the images gives crucial insight into the dusty environment of the host galaxy and the surroundings of the supernova. The outer echo from SN 2007af was created from an interstellar dust sheet located ∼800 pc in front of the supernova, while the inner echo could be from interstellar or circumstellar origin. A circumstellar light echo could imply a single degenerate progenitor. The dust is closer to the supernova for the echo in SN 2009ig. Exploring the color of the

echoes gives implications on the dust type, and both light echo cases have atypical color evolution from model predictions, which suggests abnormal dust is involved. The echoes from SN 2006X and double echo from SN 1998bu show the evolution of the echoes over a long time period, which can be compared to past findings by multiple teams. The echoes show remarkable similarity to other Type Ia echo detections, and with more discoveries, the transition of light echoes from normal emission can be investigated, which could further probe the supernova ejecta. Using a process we developed, we calculate the magnitude differences between *Hubble Space Telescope* and standard filters in the case of normal supernovae. We conclude by comparing all light echo detections to date and discussing the future goals of this work.

Table of Contents

List of Tables

List of Figures

Chapter 1

Introduction

Type Ia supernovae (SNe Ia) are used extensively in astronomy due to their high intrinsic luminosities and have led to the discovery of the accelerated expansion of the universe (Riess et al., 1998; Perlmutter et al., 1999). With very nearby SNe Ia exploding in recent years, the most detailed study of these objects has resulted in a deeper physical understanding. SN 2011fe (D = 6.4 Mpc $\pm$ 0.2 Mpc) and SN 2014J (D = 3.5 $\pm$ 0.3 Mpc) have pushed the field forward with the unique opportunity to observe these objects from X-ray to radio wavelengths (Brown et al., 2012; Dittmann et al., 2014; Tsvetkov et al., 2013; Marion et al., 2015). Extensive monitoring helps to constrain the progenitor system, galactic chemical evolution, and allows for a more comprehensive picture of the explosion, which is invaluable to improve the use of SNe Ia as standardizable candles.

On the other end of the spectrum, late observations probe the supernova interior. The optically thinning layers in the nebular epochs permits direct analysis of the core. By studying the late-light curves, energy deposition and the escape of positrons can be investigated and compared to theoretical predictions of elemental abundances. These are also the most suitable epochs to search for light echoes, which results in a distinct plateau feature in the light curve $\sim$10 magnitudes fainter than the source at peak (Patat, 2005). Without the SN emission, the telltale rings of an echo are easily distinguished from the background. Echoes can be used as a diagnostic tool for studying the surroundings of the supernova and can put constraints on the progenitor system and explosion mechanism.

1.1 Late-Epoch Behavior of Type Ia Supernovae

My Ph.D. research began with monitoring Type Ia supernovae out to late epochs in optical and near-infrared wavelengths. At >100 days after the explosion, the ejecta become optically thin enough for the core to be studied. Total masses of elements in the ejecta can be measured, which are vital to compare against the predicted element abundance yields from deflagration and delayed-detonation models (Nomoto et al., 1984). Milne et al. (1999) and Chan and Lingenfelter (1993) report that the explosion of a SN produces electrons that thermalize from ionization and excitation and later recombine.

The decay products of the SN explosion dictate the decline of the light curve. ^{56}Ni has a lifetime (τ) of 8.8 days, while ^{56}Co has a much longer lifetime of 111 days. Thus, at >100 days, the SN luminosity has decreased dramatically. Between 100 – 200 days after the SN explosion, the ejecta become transparent to gamma rays. Deposition of positron kinetic energy in the SN ejecta powers the light curve decline (Lair et al., 2006). Although SNe Ia are extensively used as cosmological tools due to the homogeneity of their light curves, prolonged monitoring has revealed subtle differences and subclasses in these seemingly uniform objects. This has dramatic implications on their application to cosmology and needs to be further investigated.

Late-epoch observations are key to investigate if positrons escape the SN ejecta or if they are trapped, which leads to annihilations and deposition of energy into the ejecta. By simulating the decay products of the SN explosion and comparing with the observable spectra and light curves of SNe Ia (see Figure 1.1), the energy deposition rate in the SN ejecta can be probed. Sollerman et al. (2004) models decline rates with and without photoionization compared to observational data from seven Type Ia supernovae. These models represent two treatments of UV photons. No variation between the small sample is seen at late-epochs, and the simulations suggest that models that include positron trapping best replicate the observations (Lair et al., 2006).

Studying SNe Ia at late-epochs is important in understanding the nature of the explosion and differentiate between the subclasses. These studies are also at a crucial epoch to detect light echoes, which could further probe the explosion mechanism.

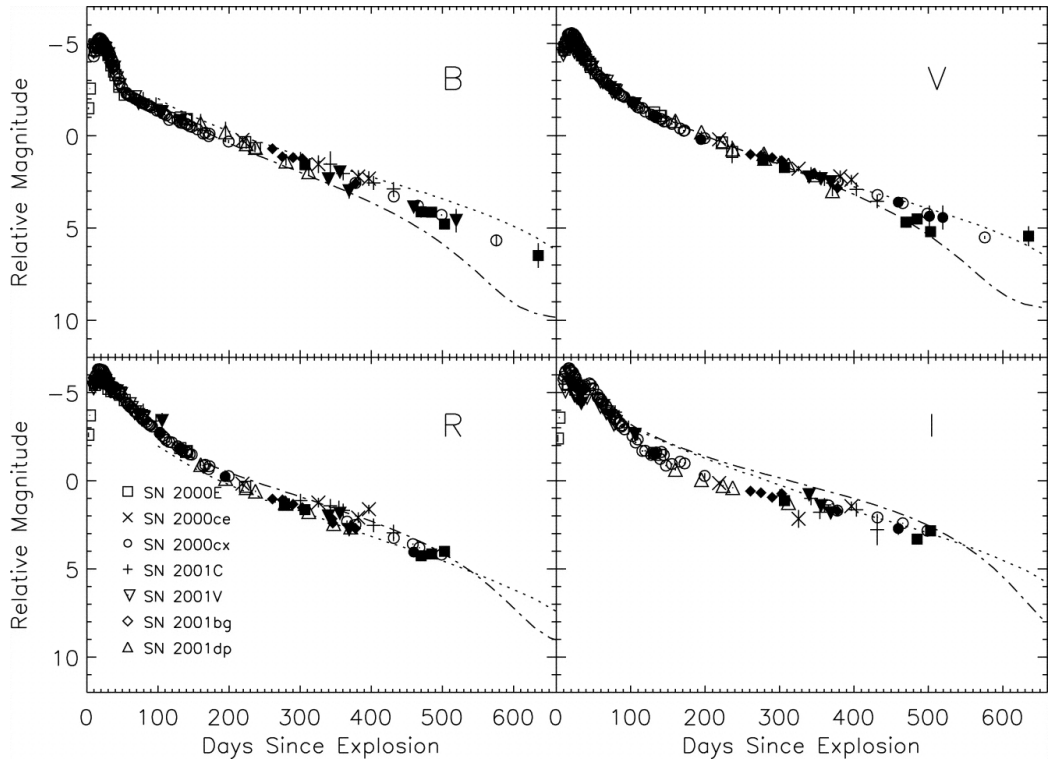

Figure 1.1: Late $BVRI$ light curves of Type Ia supernovae are compared to Sollerman et al. (2004) radiation transport models including photoionization (dotted line) and without (dash-dotted curve) (Lair et al., 2006).

1.2 Light Echoes in Type Ia Supernovae

In this section, I will briefly review the light echo phenomenon. For a more in-depth discussion, please refer to Drozdov (2013). Light echoes are produced when the light from a bright source scatters off dust and reflects back to the observer at some later time due to the extra distance traveled. In the single scattering scenario, the scattering surface is the iso-delay surface of the light (ellipsoid), which can be approximated as a paraboloid since the distance from the SN to the observer is much greater than the distance between the dust and the source. In this geometry, the SN is located at the focus of the paraboloid. The echo is created when dust (we assume a dust sheet for our analysis) intersects the t paraboloid, which produces a light echo ring with the SN explosion site located at the center of the ring. An inclined dust sheet relative to the line-of-sight will result in an echo ring with the SN position located off-center. The basic geometry of a light echo is shown in Figure 1.2.

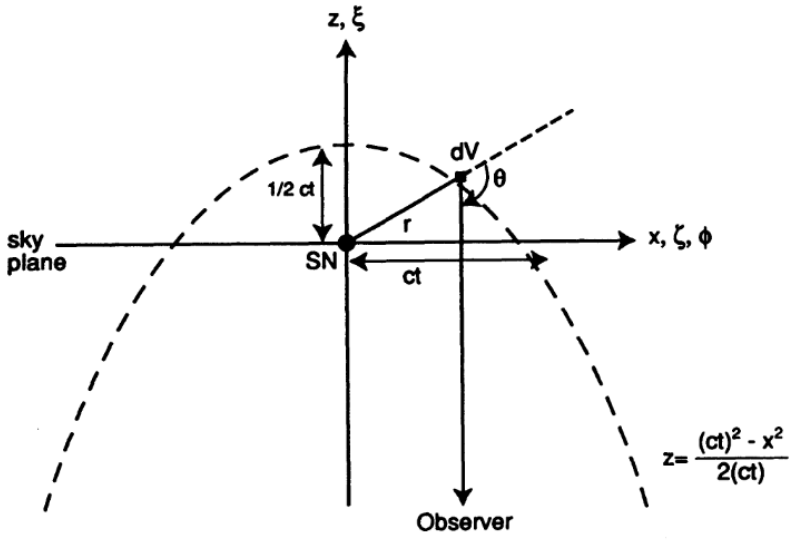

Figure 1.2: The schematic for the geometry of a light echo, showing the t paraboloid and the equation for the dust sheet distance away from the SN (labeled z here), where x is $D\theta$ (distance to observer x angular size of echo) (Sparks, 1994).

Light echoes in Type Ia supernovae, as opposed to other supernovae, are easiest to detect because of the bright luminosity of these objects. That being said, <10 extragalactic cases have been discovered in the past two decades. A bias could be attributed to the lack of late-time observations of SNe Ia. Most teams focus on early observations to constrain dust parameters, progenitor, and hence, explosion models. As for SN Ia light echoes, all except one detection was discovered >300 days past maximum. Light echoes are much easier to detect after this epoch, when the intrinsic SN emission from the decay of ^{56}Ni $\rightarrow$ ^{56}Co $\rightarrow$ ^{56}Fe has faded, and the $\sim$10 magnitude difference between peak–echo is apparent. Patat (2003); Patat (2005) argues that light echoes should be $\sim$10 magnitude fainter than the source at peak due to typical dust densities, echo geometries, and the distance between the SN and the observer. Our late-epoch monitoring put us in a unique position to not only study SNe Ia at nebular epochs, but also monitor nearby, peculiar cases for the emergence of a light echo at late-times. We chose nearby cases because the $\sim$10 magnitude difference would be $V = \sim$23 mag at the faintest, which could still be detected with medium-class ground-based telescopes. For SNe located near the dusty spiral arms of their host galaxies, we require galaxy subtraction images, which we obtain over two years past peak light. These images are also used for the search of light echoes.

Recently, a light echo was detected in Type Ia SN 2014J (Crotts, 2014). Peak data suggests an unusual dust law of $R_V = 1.46$ and color excess of $E(B - V) = 1.23 \pm 0.01$ mag, which results in an extinction of A_V of 1.80 mag (Marion et al., 2015). The extinction of the SN, and the close proximity of the host galaxy, M82, prompted observers to search for an echo. At only 234 days past maximum, this is the earliest light echo detection to date. The echo was detected in short exposures obtained with the WFC3 from program 13626: P.I. A. Crotts. 576s of F438W, 560s of F555W, and 512s of F814W were used to determine magnitudes of the echo in B, V, and I of 16.9, 16.7, and 16.8, respectively. Considering the early detection of the light echo, the magnitudes are suspect to SN emission contamination. Crotts (2014) concludes that a 300 pc away dust sheet created the outer echo, with a possible 80 pc away dust sheet producing an inner echo. Future observations will be able to confirm the echo discovery and provide further analysis. The light echo is only $\sim$6 mag fainter than the SN at peak in V, and even with extinction correction, this echo is a strange case compared to the other reported SNe Ia echoes (see Chapter 6 for further discussion).

1.3 Light Echoes as Tools

Light echoes probe the environment and provide valuable information about the dust, progenitor, and the nature of the source. Light echoes can be used to classify historical supernovae by comparing the light echo spectra with SN templates (Rest et al., 2005, 2008, 2011, 2012). The spectrum of an echo is the span of light around peak brightness being averaged through the spatial extent of the dust. Thus, echo spectra are compared to templates averaged over a range at peak for comparison (Krause et al., 2008) Using polarization measurements, a purely geometric estimate of the host galaxy distance is possible. Light echoes are powerful tools in investigating the interstellar (ISM) and circumstellar (CSM) dust around the source, which has direct implications on the progenitor of the system. The size of echoes, combined with the time since peak brightness, and the distance of the host galaxy allows one to determines the distance between the source and the dust. In the case of SNe Ia, another method to study the nature of the progenitor is of great interest in understanding the explosion mechanism(s) involved. By monitoring the color of echoes, the dust type and grain size can be inferred. The size of an echo evolves in time, and with multiple epochs of observations, the growth can be characterized and compared to the predicted value. In select cases, multiple echoes form, which further probe the surroundings.

1.3.1 Distance to Host Galaxy

Host galaxy distances are important for determining the Hubble constant, H_o, accurately for cosmological purposes. Light echoes have been used as a way to estimate the distance to the host galaxy geometrically (Sparks, 1994, 1996; Sparks et al., 1999; Bond et al., 2003), but uncertainties in the angular diameter of the echoes limit the utility of that technique.

In the latest Planck results (Planck Collaboration et al., 2014), the Hubble constant was constrained to 67.3 ± 1.2 km s^{-1} Mpc^{-1}, while the value determined from fitting Type Ia supernovae with Cepheid variables to calibrate the magnitude-redshift relation was 73.8 ± 2.4 km s^{-1} Mpc^{-1} (Riess et al., 2011). Measurements of the Hubble constant using SNe Ia are prone to errors due to poorly understood fundamentals and rely on consistency tests and calibrations such as metallicity dependence of Cepheid period–luminosity relation and calibrating the color–decline rate–luminosity of SNe Ia. Also, photometric transformations can induce systematic errors in the analysis. Therefore, a geometric way to have a secondary estimate of the host galaxy distances is highly desirable.

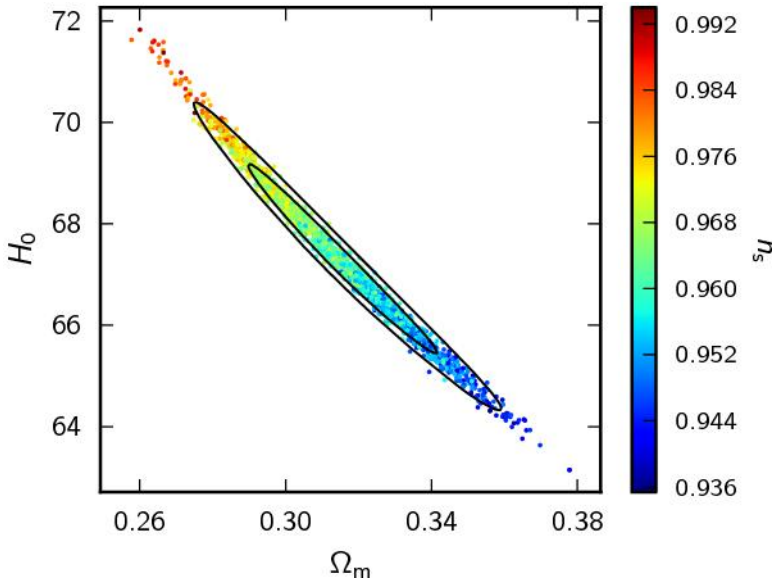

Figure 1.3: The matter density parameter–H_o constaints colored by the spectral index value n_s from Planck Collaboration et al. (2014). The figure shows the 68% and 95% contours illustrating the improvement of the recent data release.

Estimating the distance to host galaxies of SNe using light echoes is direct and does not rely on secondary indicators for calibrations. Polarization is maximum at 90° scattering, and the scattering angle is related to the angular distance of the SN. Where the paraboloid intersects the

plane of the sky at the SN position, light is scattered at 90°. This intersection forms a degree of polarization ring with apparent diameter $2ct$, where t is the time since the SN exploded, and c is the speed of light. The distance to the host galaxy is simply $D = ct/\phi_0$, where ϕ_0 is the angular diameter of the ring of polarization (Sparks, 1994; Boffi et al., 1999).

In theory, measuring the polarization is simple and should be possible with host galaxies <30 Mpc (Sparks, 1994). However, there are many practical limitations. The optical depth of the dust and the brightness of the SN (which depends on host galaxy distance) are crucial in resolving the ring of polarization. Since echo detections are rare, the luminosity may not be sufficient to resolve the polarized ring. To detect the polarization, 8 – 10m class telescopes are necessary for galaxies beyond the Local Group (Romaniello et al., 2005). Both high resolution polarized and unpolarized images of the light echo must be taken. A blue band filter is preferred for these observations since scattered light tends toward bluer wavelengths. This type of observing program was undertaken in 2003 and 2006 to observe the light echoes in SN 1998bu, which will be discussed in Section 4.2.

Sparks et al. (1999) reported the polarization measurement results of the light echo in SN 1991T. *HST* observations using the Wide Field and Planetary Camera 2 (WFPC2) and Faint Object Camera (FOC) obtained images using both unpolarized images and images produced with three double Rochon prism polarizers, oriented 60° to one another. The total flux for each polarizer was compared to determine if a polarization measurement was detected, with only a total integrated degree of polarization of ∼4% captured. This, they report, is expected with the circular symmetric pattern typically produced from the scattering by a single, central source, resulting in a cancellation of polarization (Figure 1.4). However, some emission (polarization levels of up to ∼30%) was detected at the center of the echo, which is consistent with a host galaxy distance of ∼15 Mpc. The host galaxy distance derived from Cepheid calibrations was 14.1 ± 0.9 Mpc (Saha et al., 2001), showing the success (albeit with high uncertainty) of the light echo analysis.

1.3.2 Progenitor

Type Ia supernovae are extensively used in cosmology to constrain the energy density of the universe, but despite some well-characterized empirical relations, the underlying physics remains partially understood. Even the explosion mechanism of the SN is still debated. New techniques to investigate the progenitor system for SNe Ia are needed. Light echoes can be used to determine the distance between the dust and the SN. With the high luminosity of these exploding stars, this

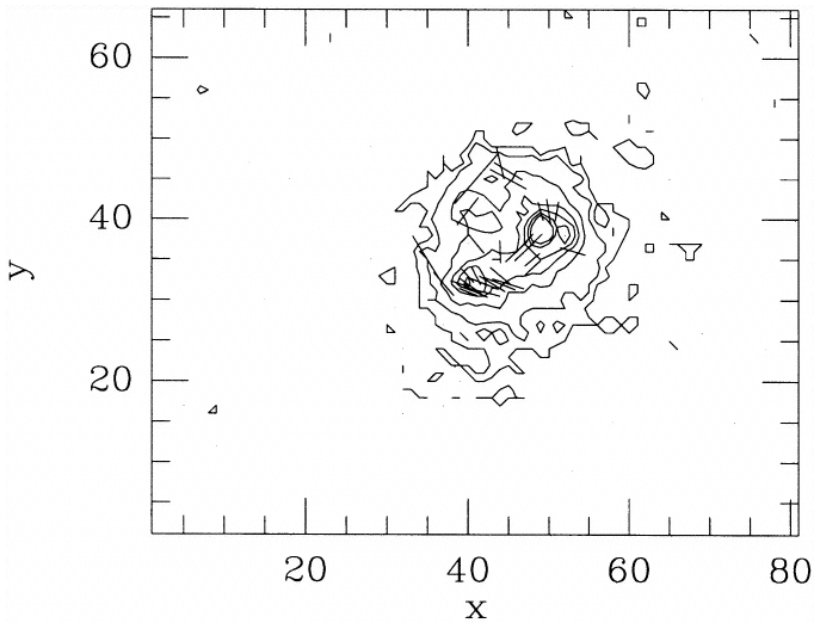

Figure 1.4: The polarization electric vectors of the light echo from SN 199T superimposed on a contour map of the echo. This illustrates the circular symmetry in the polarization. Polarization levels of ∼30% are derived from the center (Sparks et al., 1999).

distance can be hundreds of parsecs away, implying an interstellar material origin. The angular size of other echoes has been shown to be consistent with a much closer distance to the SN and possibly of circumstellar material origin.

Two leading theories have emerged to explain the explosion of SNe Ia: the single-degenerate scenario (SD) and the double-degenerate scenario (DD). The SD scenario consists of a carbon-oxygen white dwarf binary system with a red giant, main sequence star, or subgiant companion. The companion sheds material onto the white dwarf, and once the mass approaches the Chandrasekhar limit (∼1.44 $M_{\odot}$), a thermonuclear runaway is triggered from the unstable conditions. In the DD scenario, two white dwarfs merge, which triggers the thermonuclear explosion by the same method. There are also other theories of triple systems that we will leave for the reader to explore.

Circumstellar light echoes could be used as evidence of the SD progenitor scenario (Wang et al., 2008; Garnavich et al., 2001). Patat et al. (2006) argues that the SN explosion itself would destroy nearby dust, which would make CSM echoes highly unlikely. Also, if the dust could survive the explosion, to be sufficient to create an echo would require optically thick conditions. This could be the reason that CSM light echoes (<10 pc) are not as commonly found (Sugerman, 2003; Patat

et al., 2007; Förster et al., 2013). The basic geometry of a circumstellar echo is shown in Figure 1.5. A circumstellar light echo has been argued for SN 1998bu (Garnavich et al., 2001), SN 2006X (Wang et al., 2008), and SN 2007af (Drozdov et al., 2014). In this dissertation, we present further analysis and comparisons of the CSM echoes of SN 2007af and SN 1998bu. Since the circumstellar aspect of the echoes is a controversial result, we also investigate other possible explanations for the echoes.

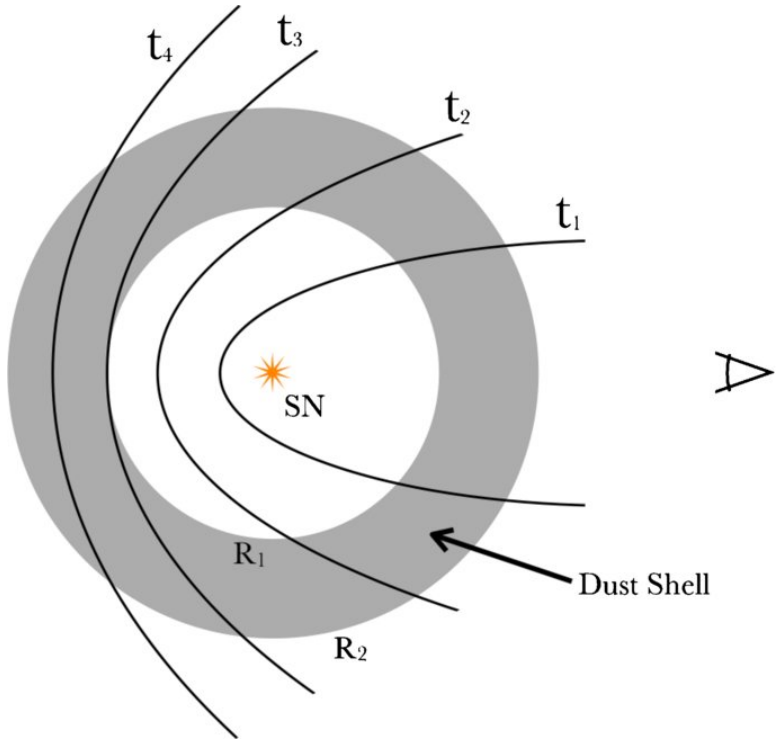

Figure 1.5: Schematic from Miller et al. (2010) of a typical circumstellar envelope around a mass-losing star that could produce a light echo. Although this figure represents the geometry of an infrared echo for Type II SN 2006gy, it is still applicable for Type Ia SN CSM echoes. A dust shell surrounds the SN and could produce an echo from forward or backscattered light off dust surrounding the source. As time grows, the echo evolves.

1.3.3 Dust Probe

A direct way to study the dust around supernovae is to image the light reflecting off of dust (i.e. a light echo). As mentioned previously, the ISM versus CSM nature of the echo can have immense implications on the progenitor of the system. The distance the dust is away from the SN is of great interest to study the mass-loss of the progenitors. As mentioned in Drozdov (2013), the color of the echo can also be used to determine the type of dust that created the echo and also put

constraints on the dust grain size.

The degree of symmetry of the explosion can be investigated with light echoes (Rest et al., 2012) using 3-D mapping of the dust. If multiple echoes are detected, the surroundings of the source are viewed from multiple angles. Optical spectra of three distinct Cas A light echoes (Figure 1.6) probed different regions in the SN photospheres. This is the first study of this kind. The time-weighted spectra revealed that two of the echoes were indistinguishable from prototype Type II SN 1993J, while the third had blueshifted He I and Hα features ($\sim$4000 km s^{-1}) in the time-weighted spectra. These features translate to a higher ejecta velocity in this direction, suggesting an asymmetry to the explosion of the SN in the year 1681 $\pm$ 19.

As described in Tylenda (2004), the inclination of the dust sheet can be determined by the distance the light echo ring is offset from the center of the SN position. Using the same axis convention as shown in Figure 1.2, the z axis is the direction of the line of sight, the y axis is in the vertical direction, and the x axis is along the horizontal. If we assume a thin sheet of dust with normal vector ($\hat{n}$) in the (x,z) plane intersecting the z axis at angle α, then the sheet is expressed mathematically by Equation 1.1, where a = tanα. Using the geometry of a paraboloid, the echo shape is described by Equation 1.2, where c is the speed of light.

$$z = z_0 - ax \tag{1.1}$$

$$x^2 + y^2 = (ct)^2 + 2z_0ct - 2axct \tag{1.2}$$

The light echo has a ring with radius $\zeta = \sqrt{(1+a^2)(ct)^2 + 2z_0ct}$. The center of the ring has coordinates x_c = -act, y_c = 0. The offset between the SN position and the echo center grows in time at a constant velocity of $|a|c$ in the opposite direction of the slab projected normal on the sky.

1.3.4 Echo Evolution

If the dust sheet is extensive and continues to intersect the t paraboloid, the angular size of the echo will grow in time. If multiple observations spanning years or even decades (in the case of

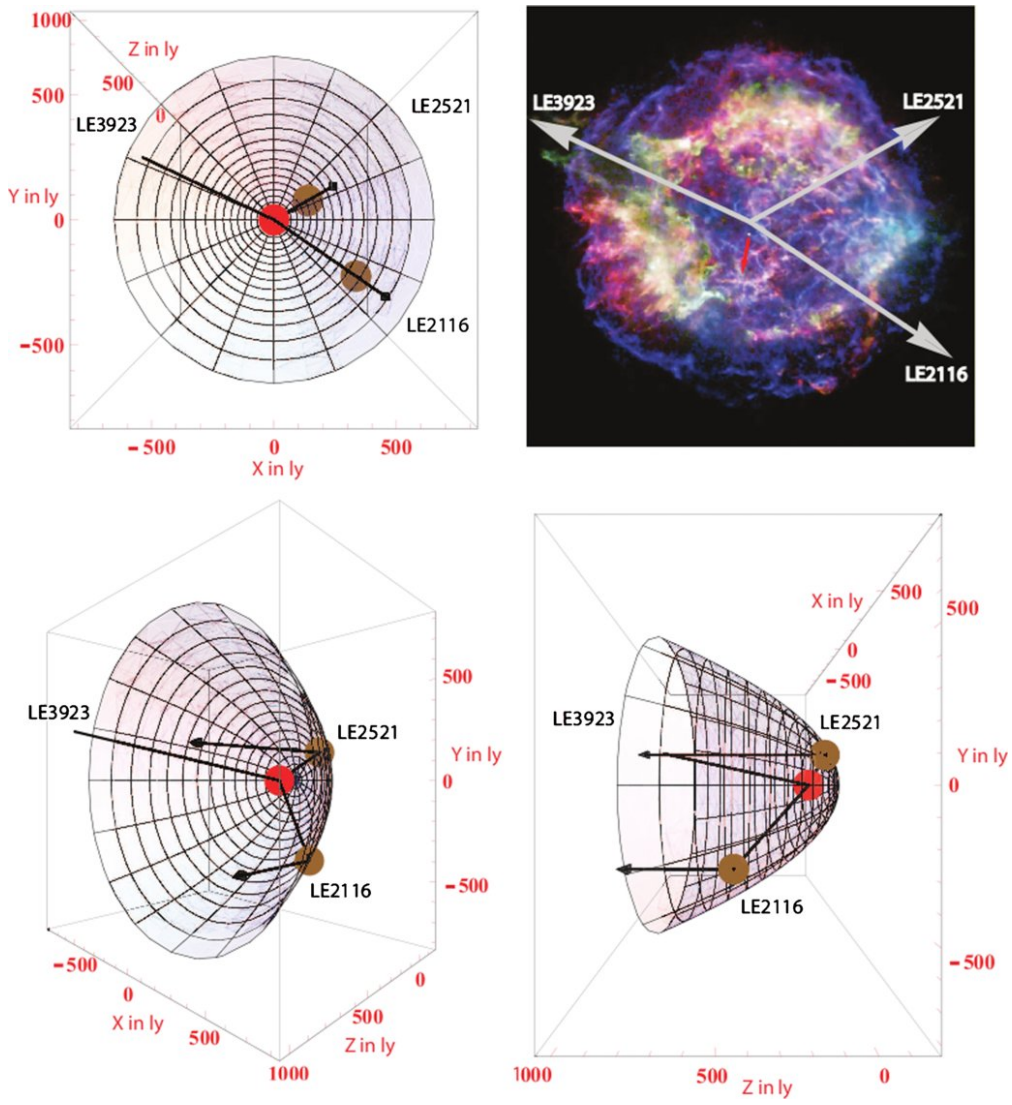

Figure 1.6: Rest et al. (2012) reports the asymmetry of the Cas A SN explosion determined from three light echoes that probe separate regions. The paraboloid of the light echo is shown from various angles with the SN (in red) at the focus. The brown circles are the scattering material, with the black arrows showing the path of the light to the observer from the SN. LE3923 was created from dust >2000 ly away from the SN. Thus, the full path is not shown. The top right panel is a *Chandra* X-ray image (Hwang et al., 2004) with the light paths superimposed in grey. The red arrow refers to apparent motion of the X-ray compact object located near the center of the supernova remnant.

SN 1998bu) are obtained of the light echo, a detectable growth can be observed. This, in turn, can be compared to the predicted growth (see Equation 1.3), where θ is the angular size of the echo in arcseconds, d is the distance between the dust and SN, t is the time since peak (in yrs), c is the speed of light, and D is the distance to the SN. Following convention, we use t to refer to the time since

B maximum. The equation holds in the assumption of a dust sheet. For a shell of dust surrounding the source, change the positive sign to negative.

$$\theta = \frac{\sqrt{2ctd + (ct)^2}}{D} \tag{1.3}$$

Figure 1.7 shows the measured and predicted echo growth of the variable eruptive star V838 Monocerotis (Crause et al., 2005). Here, both the shell and dust sheet models were compared to the actual measurements, showing the small difference in the two year timespan of the observations. Figure 1.8 shows the visual expansion of the echo of V838 Mon from Crause et al. (2005). Multiple epochs of V838 Mon from 2002 – 2004 in $BVRI$ show the impressive expansion of the light echo. The angular size of the echo is indicated by the black horizontal bar shown in the V panel of images.

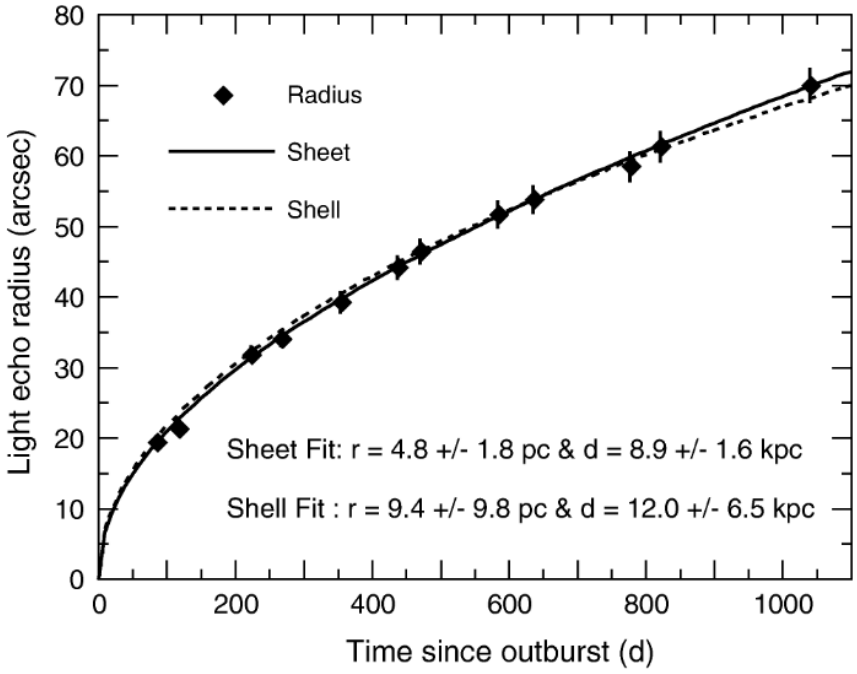

Figure 1.7: The prolonged observations of V838 Mon show the agreement between the observed light echo radius ($''$) and the predicted angular size models for a thin sheet (solid line) and shell model (dashed line) (Crause et al., 2005).

The dissertation is organized as follows: early- and light echo observations of SN 2007af, SN 2006X, SN 1998bu, and SN 2009ig are described in Chapters 2, 3, 4, and 5, respectively. We compare

these results with all other Type Ia supernova light echo detections in Chapter 6. Chapter 7 presents our conclusions and the work that will continue after the completion of the dissertation. Finally, we discuss the non-negligible magnitude differences between *Hubble Space Telescope* and standard filters for the use of Type Ia supernovae in the appendix at the end of the dissertation.

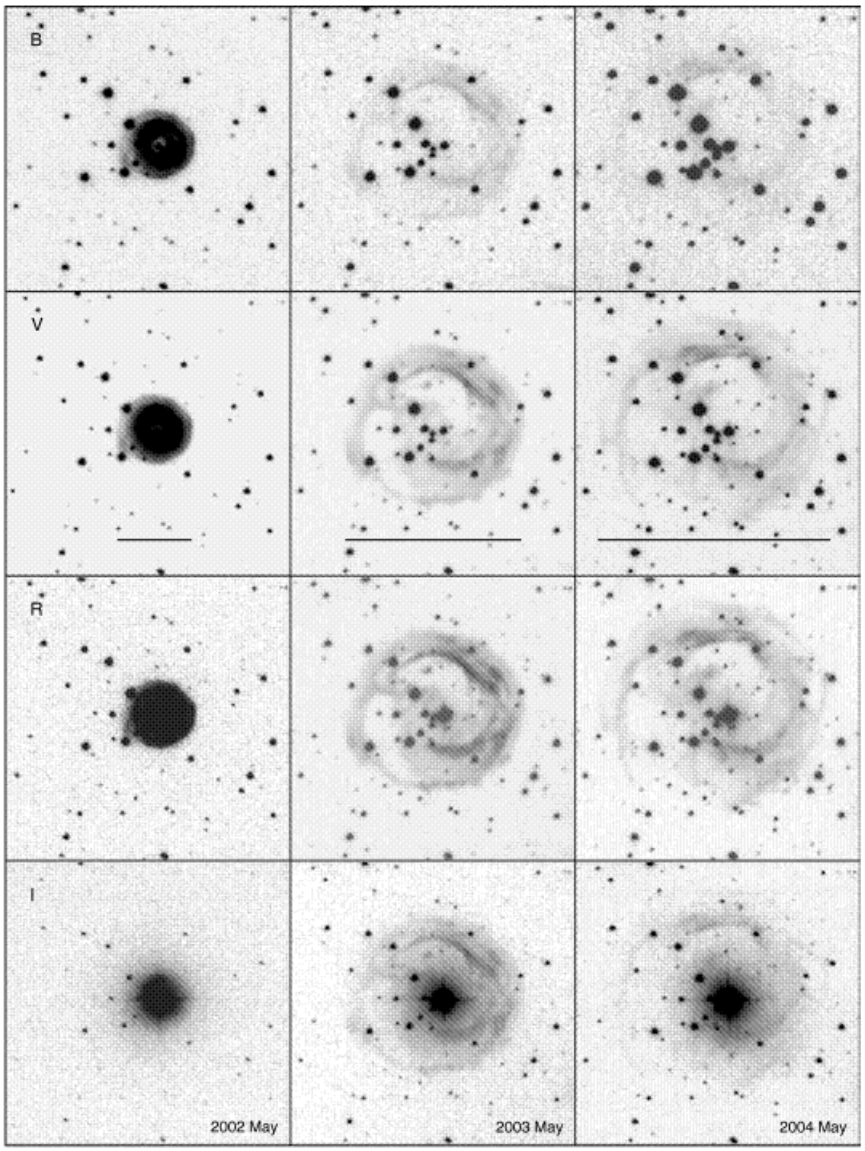

Figure 1.8: The 2.5″ x 2.5″ $BVRI$ images of the evolution of the echo of V838 Mon taken with the South African Astronomical Observatory CCD on 2002 May 1, 2003 May 21, and 2004 May 7. The echo diameter is shown with the horizontal bar in the second row panels (Crause et al., 2005).

Chapter 2

SN 2007af

The light echo from SN 2007af was extensively detailed in Drozdov (2013). Here, we provide background information and report the updated results of our analyses. These findings have recently been published in the Astrophysical Journal (Drozdov et al., 2014). We report on the continued analysis and results from Steward Observatory, Kitt Peak National Observatory, and *Hubble Space Telescope* of the light echoes discovered in data obtained three years after maximum.

SN 2007af, a normal Type Ia supernova, was discovered by K. Itagaki on 2007 March 1.84 (UT dates are used throughout) at $\alpha = 14h22m21.03s$, and $\delta = -0°23'37.6''$ well before maximum. As reported in Simon et al. (2007), SN 2007af peaked on 2007 March 14.76 $\pm$ 0.12d (JD = 2454174.26). The SN location (offset $40''$ west and $22''$ south from the center of NGC 5584) made for an ideal candidate for multi-epoch monitoring. The line-of-sight extinction estimate from Simon et al. (2007) was $A_V = 0.39 \pm 0.06$ mag using an extinction law of $R_V = 2.98 \pm 0.33$. Due to the low extinction and the normal behavior at peak, SN 2007af was considered an unlikely candidate for a light echo.

2.1 Ground-based Observations

Our continued monitoring of Type Ia supernovae out to late-epochs using Steward Observatory and Kitt Peak National Observatory resources has resulted in an unprecedented opportunity to detect light echoes. While most teams focus on gathering peak information about SNe Ia, we monitor the subtle differences in the late-time behavior. With our ground-based monitoring, we

have detected and provided the ground-based compliments to two light echoes: SN 2007af and SN 2009ig.

2.1.1 Steward Observatory Observations

SN 2007af was monitored with the Montreal 4K imager (Mont4K) on the 1.5m Kuiper telescope and the 90Prime Imager on the 2.3m Bok telescope. The 1.5m Kuiper telescope is located on Mount Bigelow in the Santa Catalina Mountains. The Mont4K optical imager is equipped with a Fairchild 4000 x 4000 pixel CCD with a $9'.7$ x $9'.7$ field of view. The telescope features a primary focal ratio of $f/13.5$ Cassegrain focus. The optical imager used on the Bok telescope at Kitt Peak, 90Prime, is a prime focus, wide-field imager, which utilizes a mosaic array of four 4000 x 4000 pixel CCDs and images an area of 1.0 square degrees. Aperture photometry was performed using Landolt standard stars (Landolt, 1992), and the images were reduced using standard IRAF[1] procedures. The late-epoch Steward observations were analyzed after template subtraction using both *HST* images and images obtained from NASA/IPAC Extragalactic Database (NED)[2]. Photometry was rerun on all Steward Observatory images, and low quality observations (including late-epoch) were discarded. The updated photometry can be seen in Table 2.1.

Table 2.1: Optical Photometry from Steward Observatory

JD (days)	B	err(B)	V	err(V)	R	err(R)
2454208.9	16.20	0.01	14.99	0.01	14.54	0.01
2454229.5	16.71	0.01	15.69	0.01	15.35	0.01
2454230.5	16.70	0.01	15.74	0.01	15.44	0.01
2454231.5	16.79	0.01	15.73	0.01	15.46	0.01
2454246.5	16.88	0.01	16.06	0.01	15.87	0.01
2454257.5	17.03	0.01	16.57	0.01	16.20	0.01
2454481.5	20.39	0.01	20.38	0.04	20.42	0.41
2454509.5	...	...	20.25	0.04	20.89	0.07
2454539.5	...	...	20.83	0.07	21.32	0.08
2454540.5	...	...	20.78	0.03	...	...
2454562.5	21.25	0.07	21.54	0.08	21.51	0.08
2454908.5	...	...	22.76	0.46	...	

[1]The Image Reduction and Analysis Facility (IRAF) is publicly distributed by the National Optical Astronomy Observatory (NOAO) in Tucson, AZ. NOAO is operated by the Association of Universities for Research in Astronomy, Inc. in cooperation with the National Science Foundation.

[2]The NASA/IPAC Extragalactic Database (NED) is operated by the Jet Propulsion Laboratory, California Institute of Technology, under contract with the National Aeronautics and Space Administration.

Figure 2.1: Monitoring of SN 2007af with the Steward Observatory Bok telescope (foreground) and Mayall-4m (top of the hill) was completed at Kitt Peak National Observatory

2.1.2 Mayall-4m Observations

On March 21, 2014, we obtained optical images of SN 2007af with MOSAIC on the Mayall-4m at Kitt Peak National Observatory. Unfortunately, NGC 5584 was a late rising target, and we were only able to capture the echo in B after a total integration time of 8100s (see Figure 2.2). The V band images were taken during twilight, compounded with the faintness of the echoes, resulted in a non-detection. Reduction on these images was completed using routine IRAF procedures. Galaxy subtraction was performed using a template of NGC 5584 taken from NED. Aperture photometry with various apertures sizes was performed using field stars of known magnitude (from previously calibrated observations). The best fit resulted in a B band magnitude of 24.47 ± 0.61. The high error bars are due to the faintness and extended nature of the echo. When including this detection on the light curve (see Figure 2.3), we moved the observation (shown with a black filled circle) to the epoch of the HST observations for direct comparison.

2.1.3 Light Curve

Early- and late-epoch observations complete the light curve (Figure 2.3) and are plotted against the dashed line of normal Type Ia SN 1992A (Suntzeff, 1996). The late-epoch SN 1992A template was extrapolated using typical decline rates. At early epochs, the light curve shows no deviation from the normal template, and since little dust was detected at peak along the line of

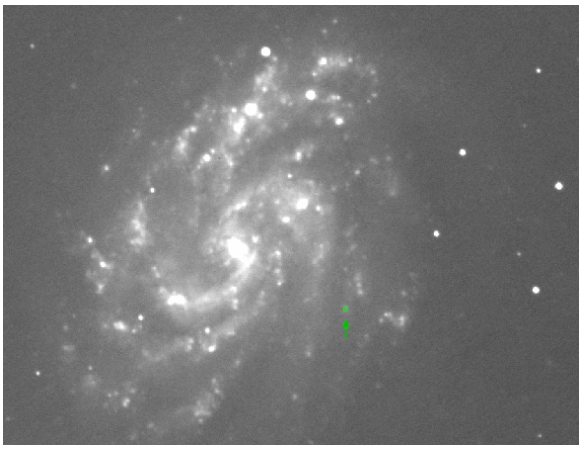

Figure 2.2: Ground-based B band image of NGC 5584 taken with MOSAIC on the Mayall-4m at Kitt Peak National Observatory on March 21, 2014 (7 years after peak). The SN location is marked with a green circle.

sight, this SN was considered a poor candidate for an echo. The normal peak behavior of SN 2007af is in sharp contrast to the late plateau. The 2009 March 18.2 (JD = 2454908.5) observations, two years past explosion, show the SN had declined considerably less than SN 1992A at a comparable epoch. The emission from Type Ia supernovae during that epoch is thought to be due to the energy deposition from positrons created in ^{56}Co $\rightarrow$ ^{56}Fe decays (Suntzeff, 1996; Milne et al., 1999). The obvious flattening of the SN 2007af light curve compared to the decline rate from intrinsic emission is attributed to the existence of a light echo. Patat (2005) argued that light echoes should be 10 – 12 magnitudes fainter than the SN at peak due to typical number density of dust particles, which is consistent with the observational sample. For thick dust shells, the change in magnitude can exceed this value. A light echo 10 magnitudes fainter than peak will reveal itself at 450+ days post-maximum.

The distinct flattening is present in B, V, and I, suggesting that an echo was captured in the HST images (in VEGA magnitudes), the ground-based Steward Observatory late-epoch observation in V, and the extremely late-epoch ground-based Kitt Peak Observatory B observation. SN 2007af was well observed in the transition from intrinsic to light echo emission. At over 1000 days after peak, the SN is $\sim$4 magnitudes brighter than predicted from intrinsic emission.

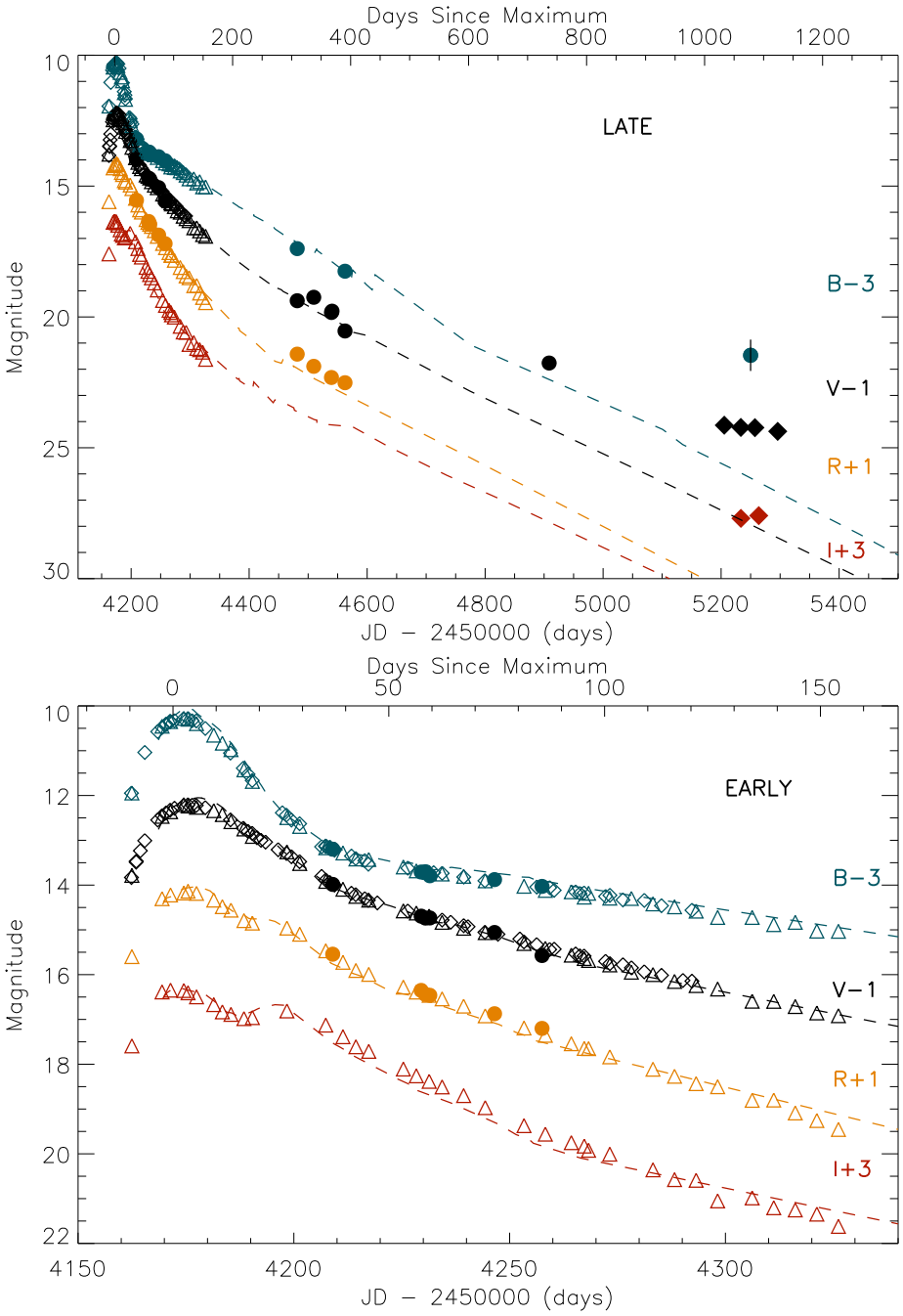

Figure 2.3: Early (lower panel)- and complete (upper panel) $BVRI$ light curves of SN 2007af plotted against normal SN 1992A (dashed line) (Suntzeff, 1996). The light echo dominates at late-times. The *HST* images are labeled with black diamonds (F555W) and red diamonds (F814W) in VEGA magnitudes. Steward observations and late-epoch Mayall-4m B observation are distinguished with filled circles. The Mayall-4m data point was moved to its present location on the light curve for presentation purposes and shows the continued presence of the echo. The early data was taken from CfA3 (BV-open diamonds) and KAIT ($BVRI$-open triangles) (Hicken et al., 2009; Simon et al., 2007).

2.2 Space-based Observations

The *HST* images reveal the light echo visually (Figure 2.4). These ∼1000 days post explosion images show a ring-like object and extended central source at the location of the SN, which we propose as outer and inner light echoes.

2.2.1 *HST* Observations

To use high-redshift SNe Ia in cosmology, the absolute magnitudes of SNe Ia must be calibrated. The best calibrations of SNe Ia use Cepheid variable stars in the host galaxies of low-redshift SNe Ia, which are calibrated with parallax and main sequence fitting, two nearby rungs of the distance ladder. Cepheid variable monitoring is one of the techniques used to measure the H_o, the present expansion rate of the universe. The "Supernovae and H_o for the Equation of State" (SHOES) project aimed to measure the expansion rate to <5% precision using SNe Ia and Cepheids. SNe Ia chosen for this cosmological study had to fit the following criteria: have modern photometric data (e.g. CCD), have observations before peak, low reddening ($A_V < 0.5$ mag), be spectroscopically classified as normal, and have *HST* optical observations of Cepheid variables in the SN host galaxy (Riess et al., 2011).

NGC 5584 was discovered to have a wealth of Cepheids and was observed with the WFC3 during *HST* Cycle 17 as part of *HST* program 11570: P.I. A. Riess. NGC 5584 was observed in the F160W (wide H), F350LP (unfiltered long pass), F555W (wide V), and F814W (wide I) filters from January – April 2010, three years after the explosion of the SN. The individual exposures were 400 – 700s in length with a total exposure time equaling 4926s. Integer and half-pixel dithering were enabled between exposures to characterize the point spread function (PSF).

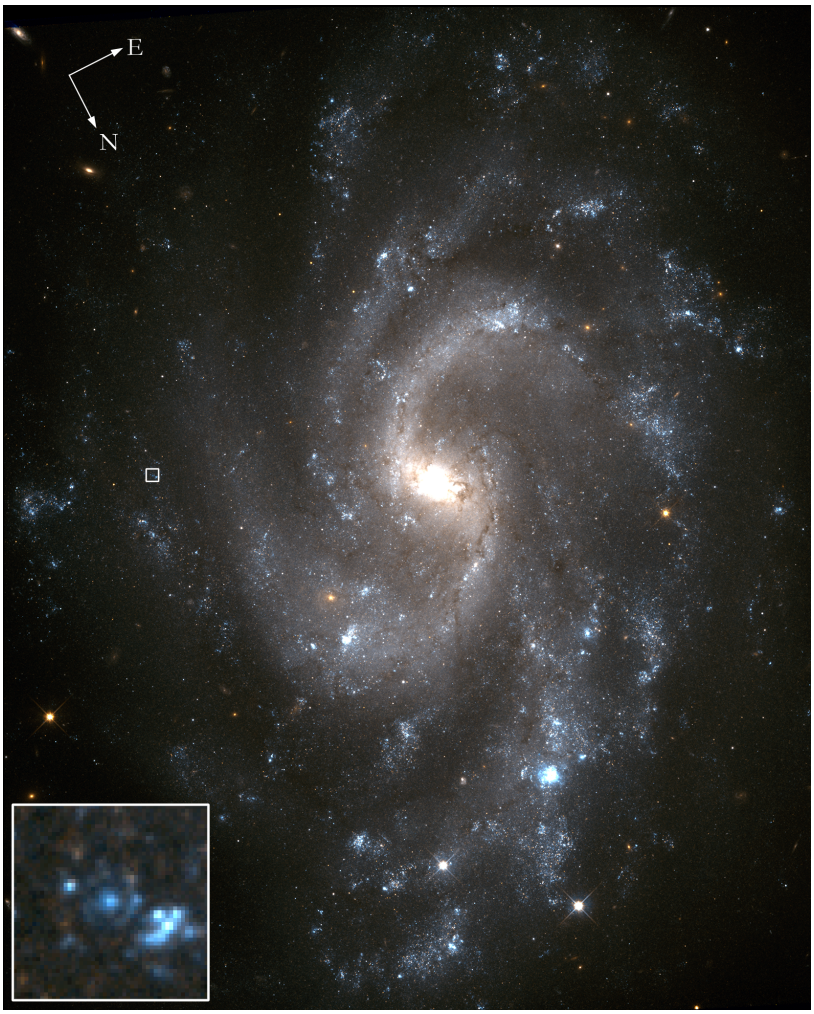

Figure 2.4: Color composite image of NGC 5584 and the combined light echo image of SN 2007af (inset panel) from *HST* WFC3. The SN location (box) is shown in NGC 5584, and the 2″ x 2″ close up of the region shows both echoes in the center of the box, nestled in between the white stellar source middle left and group of white sources bottom right. The images are the result of stacking the individual monthly observations in all filters. A ring (outer echo) surrounds the bright central region, which we propose as a secondary light echo (inner echo).

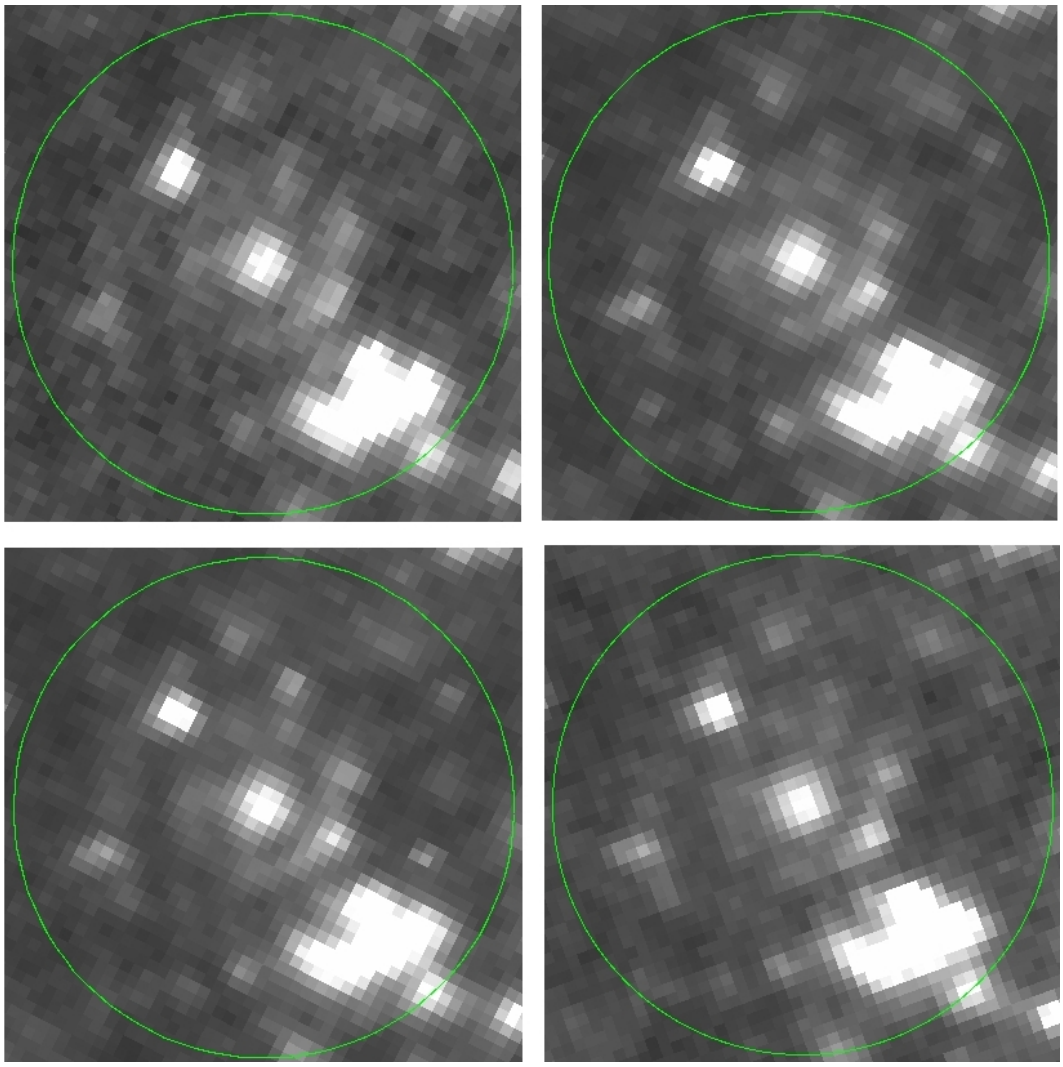

Figure 2.5: Time evolution of the light echoes from SN 2007af in the broad-band F350LP filter. Upper left panel is the observation taken in January 2010, upper right is February 2010, bottom left is March 2010, and bottom right is the observation from April 2010. The sequence of images shows the separation between the outer ring (center of green circle) and the bright central region, which we propose is a second light echo.

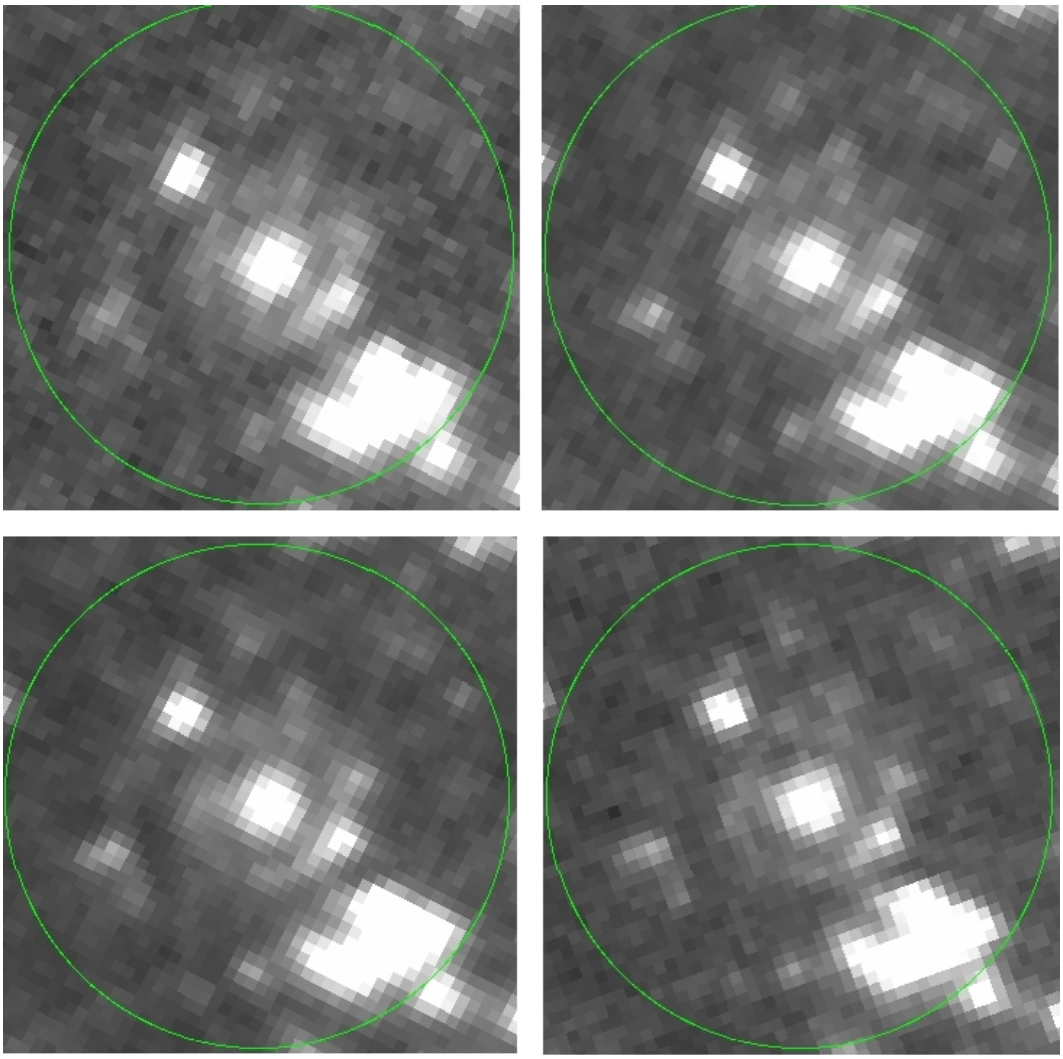

Figure 2.6: Time evolution of the light echoes from SN 2007af in the F555W filter following the same chronological sequence.

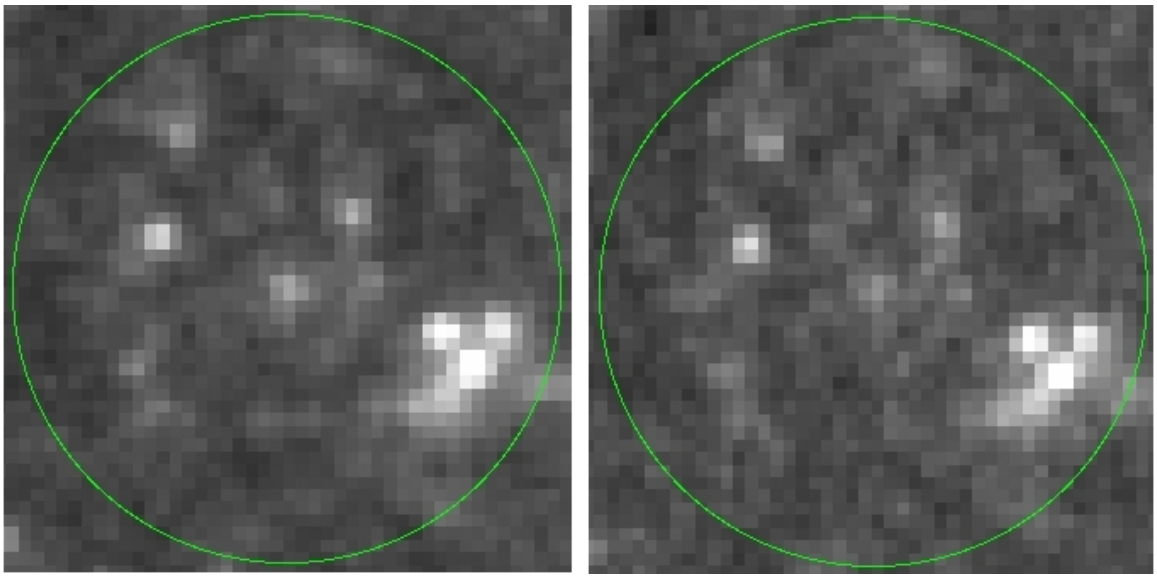

Figure 2.7: Time evolution of the light echo from SN 2007af in the F814W filter. The left panel is the February epoch, and the right panel is the March observation. The faint echoes are nestled in the center of the green circles. These echoes are much more difficult to discern since scattering at these wavelengths is not as efficient as at shorter wavelengths.

The Cepheid campaign began in January 2010, 2.8 years after the SN peak brightness. Thirty-nine images were stacked to improve the signal-to-noise ratio in four filters, with the light echoes detected in all but the F160W(IR) filter (Figure 2.8). The echoes are clearly weaker in the F814W filter than in F350LP and F555W. The echoes are faint, and in particular, the surface brightness of the outer feature is very low. The region contains a number of other emission features, both stellar and otherwise. We characterized the echoes by fitting defined shapes convolved with the PSF's of the images (see Figure 2.9).

In this analysis, we select a limited region around the SN location, determine the PSF size from a number of stars (typically twenty), subtract stellar objects near the SN, and perform non-linear least-squares fits of two shapes plus background to a region typically twenty-five pixels square around the SN. The PSF's are assumed to be azimuthally symmetric radial gaussians and are found to be consistent with $0.''11$ full-width half-maximum (FWHM). We tried a variety of different shapes for the echo features. Fits of elliptical functions did not yield significant eccentricity, regardless of axis orientations, so we quote only fits for azimuthally symmetric functions. For the central source, we tried a flat plateau and exponentials, but no shape fit significantly better than a two dimensional radial gaussian, so we use that. For the outer annular echo, we use a radial function that falls off as

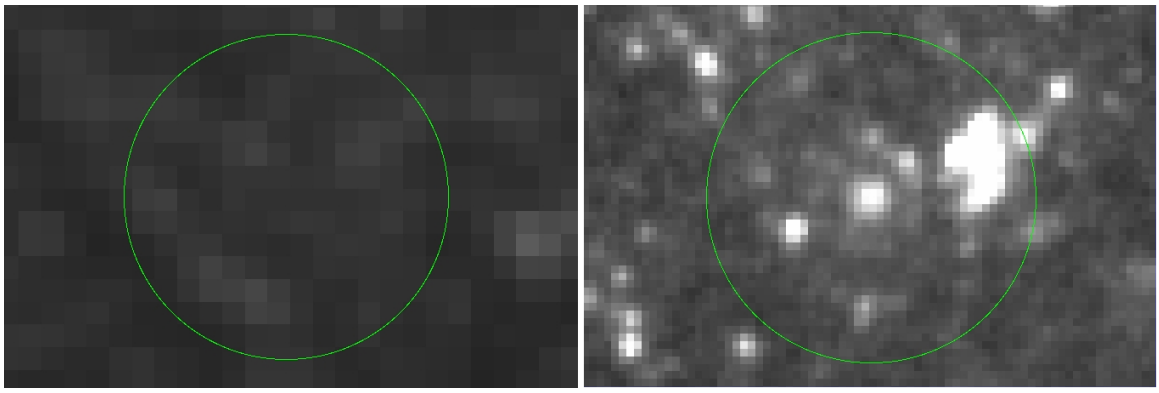

Figure 2.8: The comparison of the F160W image (left panel) with the F350LP March observation (right panel) centered on the same position, illustrating the lower resolving capabilities.

a gaussian from a radius of maximum.

Our general fit has ten parameters: a constant background, central gaussian amplitude and width, gaussian annulus amplitude, peak radius, and width, and two coordinates of the center of each of the echo shapes. Convergence is unpredictable with all parameters free because of correlations among them, so we generally constrain some of them. If we try to determine the locations of the centroids of the echoes by fixing the widths of the two echoes, we always find the coordinates of both echo centers are consistent with the location of the SN and with each other, strengthening the argument of two separate echo detections. The locations are within one-half pixel of the SN position with a one-sigma uncertainty of typically 0.2 pixels using the world coordinate system coordinates of the echo centers in the *HST* images compared to the coordinates of the SN position. To determine the intensities and widths of the features, we constrain the coordinates of the centers of the two to be the same for both. Also, the two widths and the annulus radius are highly correlated for our quoted sizes and fluxes, so we fix the annulus FWHM at the mean best-fit value ($0.''16$) and allow the central source FWHM and annulus peak radius to vary.

Where there are non-stellar features in the fit region that are unrelated to the SN echoes, we exclude those points from the fits. The models are convolved with the PSF's and fit to the data. The resulting least-squares fits are typically not formally good fits, with reduced χ^2 typically 1.5 to 2.0 for 450 degrees of freedom. The central echo is generally well fit, but the outer echo is not smooth and not very well fit by a smooth azimuthally symmetric echo due to the faintness of the echo and contamination by artifacts. Still, the fits capture well the sizes and brightnesses of the

echo components. The intrinsic angular radii measurements for the outer (θ_{OE}) and inner echoes (θ_{IE}) can be found in Table 2.2 for each filter.

Light echo rings should grow with time if produced by a continuous dust sheet scattering the light. Unfortunately, the four month timespan combined with the uncertainty in the angular size of both echoes meant that we were unable to resolve the expected growth in angular radius. To confirm the growth of both echoes, subsequent *HST* imaging would be necessary. Ground-based observations can confirm that the source is still present, but space-based images are necessary to resolve the details of those observations.

Table 2.2: Angular Sizes of Echoes

Filter	JD (days)	$\theta_{OE}(''$)	$\theta_{IE}(''$)
F350LP	2455205.43	0.34 ± 0.01	0.13 ± 0.02
F350LP	2455233.52	0.32 ± 0.01	0.10 ± 0.02
F350LP	2455257.48	0.33 ± 0.01	0.11 ± 0.02
F350LP	2455296.04	0.33 ± 0.01	0.13 ± 0.02
F555W	2455205.35	0.32 ± 0.01	0.12 ± 0.02
F555W	2455233.44	0.31 ± 0.01	0.11 ± 0.02
F555W	2455244.37	0.32 ± 0.01	0.11 ± 0.02
F555W	2455257.35	0.32 ± 0.01	0.10 ± 0.01
F555W	2455295.96	0.32 ± 0.01	0.11 ± 0.02
F814W	2455233.57	0.35 ± 0.01	0.09 ± 0.03
F814W	2455263.82	0.32 ± 0.01	0.08 ± 0.03

To independently confirm the extent of the central echo, the FWHM of the source was determined using the radial profile task (r mode, which uses a radial profile Gaussian fit) in IMEXAMINE in IRAF (Tody, 1986). The analysis confirmed an extended FWHM for all echo images, although only an estimate could be made for the poorly constrained F814W filter. The measured FWHM were all consistent, within uncertainties. The average FWHM of the local stars was 2.63 ± 0.4 pixels compared to the average inner echo FWHM of 4.03 ± 0.3 pixels. Thus, the inner echo has a FWHM 1.53 times extended relative to the local stars in the field. This test illustrates the broadened feature of the source and definitively refutes the notion that the central component is simply a background star. The broadening can be interpreted as nebulosity caused by a light echo, but an extended non-echo source cannot be eliminated.

2.2.2 Light Echo Magnitude

Light echo magnitudes were determined using the fits mentioned previously and are consistent with the values obtained from estimating by eye the sizes of circular apertures and summing the counts enclosed. We spent considerable time refining the method of determining the magnitude of the light echoes and converting the magnitudes into the same system as earlier observations. This combined effort results in the most significant changes since Drozdov (2013).

The counts were converted to VEGA magnitudes using WFC3 header keyword PHOTFLAM, the mean flux density that produces one count per second in observing mode, and the filter zeropoints provided in the instrument handbook.[3] The values used in our conversions can be found in Table 2.3, where VEGA_{mag} refers to the zeropoint to convert to VEGA magnitudes. Magnitude zeropoints represent the magnitude corresponding to a (flat-field corrected) count rate of 1 electron s^{-1}, and they are used to convert instrumental to astrophysical units. The VEGA zeropoints are in the SYNPHOT standard magnitude system, for which Vega, by definition, has a magnitude of zero for all wavelengths. The Vega magnitude of a star with flux F is -2.5 $\log_{10}$ (F/F_{Vega}) where F_{Vega} is the calibrated spectrum of Vega in SYNPHOT.

Table 2.3: *HST* Photometry Parameters

Filter	PHOTFLAM (erg cm^{-2} s^{-1} $\AA^{-1}$)	VEGA_{mag} (mag)
F350LP	5.30E-20	26.79
F555W	1.87E-19	25.82
F814W	1.54E-19	24.68

The magnitudes of the inner and outer echoes listed by filter and date are listed in Table 2.4. The total magnitude of the echoes (in VEGA magnitudes) was used in plotting the *HST* observations on the light curve of SN 2007af (Figure 2.3) since the ground-based observations would not resolve two separate components.

The magnitude difference between the inner and outer echoes changes with filter. For the F350LP filter, there is a ∼0.6 mag difference between the outer and inner echo values and ∼0.7 mag difference in the F555W filter. However, for the F814W band, this value increases to ∼1.0 mag. Even with the lower sensitivity in the wide *I* filter, this noticeable change implies a change in

[3] http://www.stsci.edu/hst/wfc3/phot_zp_lbn.
[4] All magnitudes listed are in VEGA magnitudes.

Table 2.4: Light Echo Magnitudes[4]

Filter	JD (days)	Magnitude$_{OE}$	Magnitude$_{IE}$	Magnitude$_{Total}$	Δm
F350LP	2455205.43	24.48 ± 0.07	25.20 ± 0.20	24.03	...
F350LP	2455233.52	24.61 ± 0.07	25.37 ± 0.19	24.17	...
F350LP	2455257.48	24.55 ± 0.07	25.33 ± 0.19	24.12	...
F350LP	2455296.04	24.83 ± 0.09	25.34 ± 0.22	24.30	...
F555W	2455205.35	24.51 ± 0.06	25.11 ± 0.17	24.02	11.21
F555W	2455233.44	24.59 ± 0.07	25.20 ± 0.20	24.10	11.36
F555W	2455244.37	24.60 ± 0.06	25.22 ± 0.18	24.12	11.29
F555W	2455257.35	24.58 ± 0.06	25.26 ± 0.17	24.11	11.32
F555W	2455295.96	24.83 ± 0.08	25.21 ± 0.18	24.25	11.30
F814W	2455233.57	25.06 ± 0.16	25.96 ± 0.37	24.67	11.51
F814W	2455263.82	24.82 ± 0.12	26.25 ± 0.45	24.56	11.40

dust reflecting properties. This behavior seems inconsistent for two light echoes created in the same manner, which could suggest a different mechanism for producing the inner echo.

2.3 Physical Model

Light echoes are effective probes of the surrounding material, and simple applications yield ample information about the source. From the geometry of the echoes, a distance between the scattering medium and SN can be inferred, and the color of the echoes reveals information about the scattering effects and dust properties.

2.3.1 Dust Distance

Analytical treatment of the light echo phenomenon (see Couderc (1939) for more rigorous derivation) states that a dust sheet intersecting the paraboloid of constant time delay creates a circular ring echo centered on the source solely dependent on the time (t) since peak light, the speed of light c, and the distance to the SN (D), assuming a dust sheet perpendicular to the line of sight. The distance the dust sheet lies in front of the SN can be simply determined using Equation 2.1, where θ is the angular radius of the light echo.

$$d \approx \frac{D^2\theta^2 - (ct)^2}{2ct} \tag{2.1}$$

The foreground distance between the dust sheet and the SN for the outer echo was determined using $D = 24$ Mpc to NGC 5584 (Simon et al., 2007). For comparison, the distance estimate based on a joint analysis of the Cepheid and SN data by Riess et al. (2011) yields $D = 23 \pm 0.7$ Mpc after correction for the revised maser distance to NGC 4258 (Humphreys et al., 2013). The dust sheet distances can be found in Table 2.5. The average distance from the SN to the dust sheet is 790 ± 60 pc, implying that ISM dust produced the echo.

The inner echo is consistent with both a CSM and ISM sheet and represents the smallest and largest dust distances allowed by the previous analysis. From our analysis, we cannot eliminate the CSM geometry possibility. The inner echo dust distance was calculated assuming a circumstellar sheet (d_{IECSM}(pc)). Using the proposed solution of backscattered light, a dust sheet located behind the SN exists at a location determined solely by the time delay of the echo. The initial light from the SN traveled outward, backscattered off the dust sheet behind the explosion site, and returned back toward the observer. Therefore, half of the time delay determines the distance to the dust sheet. The average inner echo distance from the SN to the sheet is 0.45 ± 0.01 pc in this scenario. Alternatively, the results for the ISM dust sheet scenario are listed in the last column using the same labeling convention. The inner echo SN-foreground dust sheet distance results in an average of 90 ± 20 pc.

Table 2.5: Dust Sheet Distances

Filter	JD (days)	d_{OE}(pc)	d_{IECSM}(pc)	d_{IEISM}(pc)
F350LP	2455205.43	891	0.43	130
F555W	2455205.35	790	0.43	110
F555W	2455233.44	721	0.44	90
F350LP	2455233.52	769	0.44	74
F814W	2455233.57	920	0.44	60
F555W	2455244.37	761	0.45	89
F350LP	2455257.48	800	0.46	88
F555W	2455257.35	752	0.46	88
F814W	2455263.82	748	0.46	46
F350LP	2455296.04	772	0.47	119
F555W	2455295.96	726	0.47	85

A schematic for the dust geometry (not to scale) for the January epoch in the F555W filter can be seen in Figure 2.10 for a CSM inner echo. Because the distance from the SN to Earth is much greater than the distance between the SN and the dust, we can approximate the geometry of

the phenomenon by a paraboloid. The SN is located at the focus of the paraboloid, and the echo rings are created from the intersection between the dust sheet and the paraboloid (Patat, 2005). The orange shaded region shows the intersection that results in the outer echo, and the blue shaded region is the intersection causing the inner echo. Figure 2.11 shows the same epoch but with an ISM origin for both echoes.

2.3.2 Dust Color Analysis

Using the Patat (2005) model, the initial light is treated as a flash. The signal received by the observer at a later time t is the sum of photons from the SN in the range of time from 0 – t. The global flux measured by the observer is the echo flux combined with the photons that reached the observer on the direct path from the SN, which is then extinction corrected (using values derived at peak). The light echo flux in a particular passband is given by $F = L_o n_o C_{scat} \Delta \mathrm{t}_{SN} \mathrm{e}^{-\tau_{eff}} G(t)$, where L_o is the SN signal, n_o is the number density of scattering particles, and C_{scat} is the scattering cross-section of the dust grains. The flash duration is $\Delta \mathrm{t}_{SN}$, τ_{eff} is the weighted optical depth for the LE at a given time, and $G(t)$ is a wavelength- and time-dependent function related to the dust geometry.

The color of an echo can be predicted using the single scattering model taken from Patat (2005). The predicted color of the echo (Equation 2.2) was determined by folding the F555W and F814W WFC3 transmission filters with a peak Branch normal SN Ia spectrum (Nugent et al., 2002) scattered with Draine (2003) dust cross-sections and weighted by the flash duration in each band. These are compared to the Vega spectrum folded with the same filter transmission functions. The observed and theoretical colors are written in terms of F555W – F814W (V – I). A normal SN Ia peak spectrum was used because reddening corrections are then unnecessary, and the peak SN 2007af spectrum did not extend to the blueward wavelengths of the F555W transmission filter. The flash durations were estimated using the peak light curve of SN 2007af. We chose the flash duration to be the number of days, centered around maximum, within one magnitude of the peak value. The flash durations of V and I were estimated at 0.08 yr (30 days) and 0.11 yr (40 days), respectively. The I band had a longer flash duration due to the second maximum in the light curve.

$$(V - I) \approx -2.5 log \frac{F_V F_I^{Vega}}{F_V^{Vega} F_I} \tag{2.2}$$

Some dust parameters used are listed in Table 2.6 for illustration, where the third column is the scattering cross section for forward scattering ($\theta = 0°$), and the fourth column values are for backward scattering ($\theta = 180°$)[5]. We use the dust parameters for three types of dust: Milky Way (MW), Large Magellanic Cloud (LMC), and Small Magellanic Cloud (SMC) bar. C_{scat} corresponds to the differential scattering cross section per H atom, which determines the scattering properties of a particular dust mixture. The values listed are the ones closest to the central wavelength for F555W and F814W and merely illustrate the relation between forward and backscattering cross section. For our analysis, we integrated over all wavelengths.

Table 2.6: Dust Parameters[6]

Dust Type	Wavelength (Å)	$\theta = 0°$ $C_{scat}(cm^2)$	$\theta = 180°$ $C_{scat}(cm^2)$
MW $R_V = 3.1$	5470	1.68E-22	7.30E-24
MW $R_V = 3.1$	8020	6.27E-23	5.88E-24
LMC $R_V = 2.6$	5470	5.32E-23	1.51E-24
LMC $R_V = 2.6$	8020	1.96E-23	1.10E-24
SMC Bar $R_V = 2.9$	5470	2.38E-23	9.81E-25
SMC Bar $R_V = 2.9$	8020	8.85E-24	6.39E-25

Table 2.7: Comparison Between Peak, Echo Color, and Model Predictions

Observed			Theoretical	
Epoch	$(V - I)$ (mag)	Dust Type	$\theta = 0°$	$\theta = 180°$
Peak	-0.327	MW $R_V = 3.1$	-1.124	-0.291
Outer Echo	-0.317 ± 0.104	LMC $R_V = 2.6$	-1.122	-0.561
Inner Echo	-0.904 ± 0.304	SMC Bar $R_V = 2.9$	-1.127	-0.545

The actual echo colors using the averages measured in each filter was compared to the predicted model colors (Table 2.7). Also listed is the peak dereddened color of SN 2007af (-0.327 mag), which was obtained by integrating the peak SN spectrum over the filter responses compared to the Vega spectrum folded with the filter responses. The results of the Patat (2005) model color for forward and backward scattering calculations for the three dust types are listed in the last two columns. All values listed are in the VEGA magnitude system.

Forward scattering replicates the inner echo color at the far uncertainty limit, but does not discriminate between dust types due to large uncertainties. The outer echo color does not match predictions, and thus, abnormal dust must be considered. It is interesting to note that the outer

[5]ftp://ftp.astro.princeton.edu/draine/dust/mix/

[6]$\theta = 0°$ corresponds to forward scattering, and $\theta = 180°$ is backscattering.

echo color has not changed drastically from the direct peak light, but that is not the case for the inner echo. Dust grains are not expected to isotropically scatter light from an echo. Small angle scattering is more efficient. Thus, forward scattering is the preferred mechanism, which is consistent with the inner echo. We also tried a secondary method of predicting the echo color by binning the light curve and summing over time bins, with similar results.

Recently, lower R_V value have been reported for Type Ia supernovae (Hicken et al., 2009; Goobar, 2008). Scattered light (which causes echoes) tends to reduce the ratio of total-to-selective extinction in the optical (Wang, 2005). The ratio is significantly lower at longer wavelengths than 3000Å. Abnormal dust has been cited for adopting a lower R_V value (1.48 ± 0.06) in the case of SN 2006X (Wang et al., 2008). Goobar (2008) published simulations that yielded values from $R_V = 1.5$ – 2.5, on the basis that lower values originate from the semi-diffusive propagation of the photons near the location of the SN explosion. Eighty SNe Ia were observed with E(B – V) ≤ 0.7 mag. From this study, an average reddening law of $R_V = 1.75 \pm 0.27$ was derived. Focusing on the 69 SNe with color excess, E(B – V) < 0.25 mag, produced a total-to-selective ratio value of $R_V \sim 1$, signifying the reddening in SNe Ia may be more complex than previously thought (Nobili and Goobar, 2008). The selective extinction of SN 2007af determined from peak information (E(B – V) = 0.14 mag) fits well under both color excess limits (Simon et al., 2007). In future work, more R_V values need to be considered in our light echo color analysis.

Patat (2005) proposed that LE luminosity is inversely proportional to SN-dust distance (d) and directly proportional to the optical depth. The peak-to-echo magnitude relationship in the single scattering approximation is shown in Equation 2.3. The multiple scattering approximation to Δm is given in Equation 2.4 and follows an exponential decay. These relationships hold for d measured in ly.

$$\Delta m \approx -2.5 log(0.3\frac{\tau}{d}) \qquad (0 < \tau \leq 1) \tag{2.3}$$

$$\Delta m \approx -2.5 log(\frac{0.3}{d} e^{-\tau}) \qquad (\tau > 1) \tag{2.4}$$

Peak magnitude extinction correction was performed using ratios of total-to-selective extinction of $R_V = 2.6 \pm 0.1$ and $R_I = 1.48 \pm 0.1$. The inner echoes have not been extinction corrected because the dust associated with the outer echo would be the dominant cause of the extinction of peak light. The optical depth was calculated using the ISM distances for the inner echo and outer echo. The V optical depths are 0.15 and 0.01 for the outer and inner echoes, respectively. For I, the values are 0.16 and 0.01. From the large dispersion in the values, it is clear that the dust sheet for the inner echo must be optically thin. Because of the low optical depth, SN 2007af fits well within the single scattering approximation.

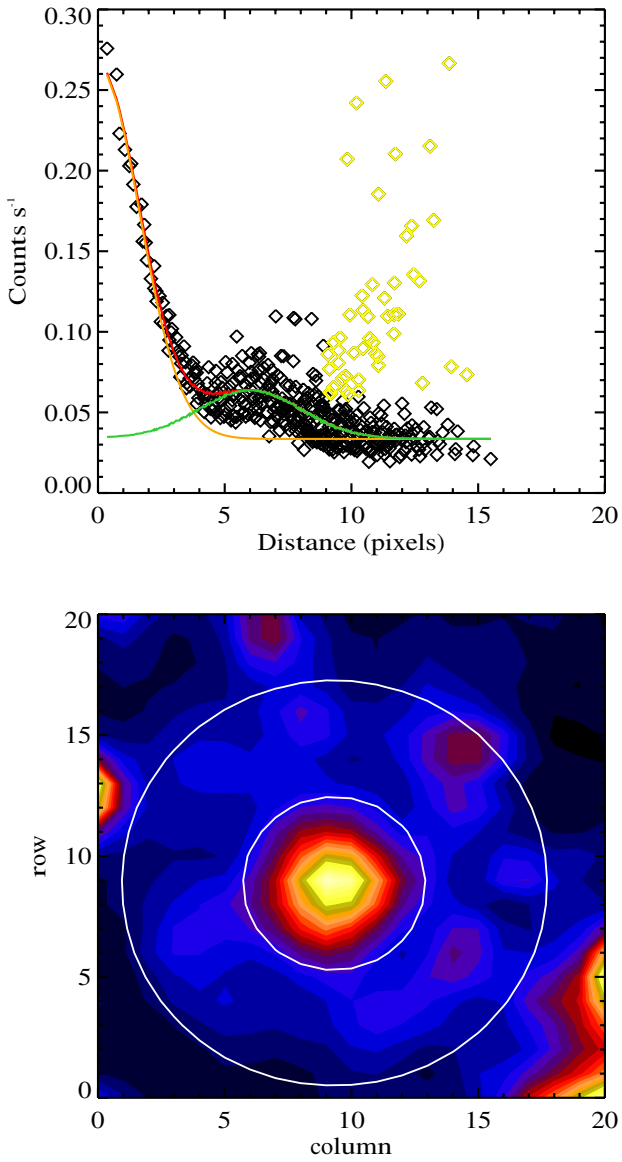

Figure 2.9: An example of the fit of our echoes in the F350LP filter. The top panel shows the count contributions in our crowded field. The yellow diamonds are high points outside the outer echo that have been omitted from the fit, the green line is the outer echo contribution, the orange line is the inner echo contribution, and red is inner and outer echo combined. The bottom panel shows both echoes, where the white circles are 50% contours of the outer echo. The axes for the top panel are counts versus distance from the centers of the two echoes (pix), while the bottom panel's axes are pixel numbers from an arbitrary point on the CCD.

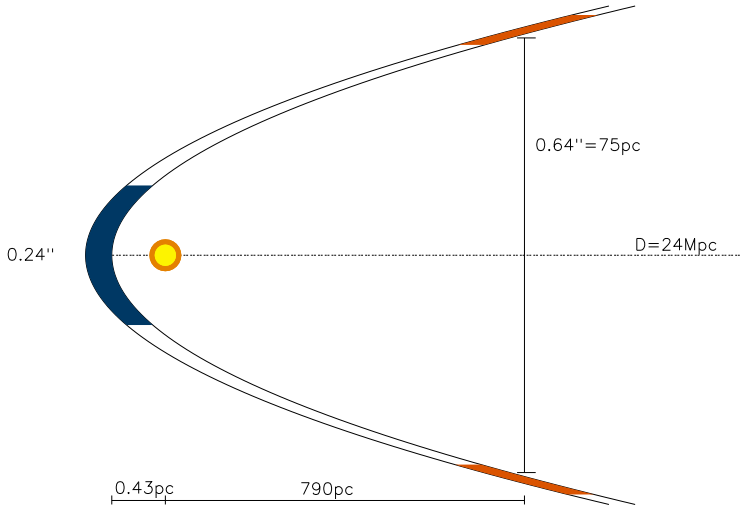

Figure 2.10: The geometry of the dust that produced the inner echo (blue) and outer light echo (orange) of SN 2007af (not to scale) in the backscattering, CSM scenario. This figure focuses on the January F555W epoch of the light echo, with $\theta_{IE} = 0.12''$, and $\theta_{OE} = 0.32''$. The figure shows the foreground dust sheet for the outer echo and a secondary dust sheet 0.43 pc behind the SN (shown in yellow).

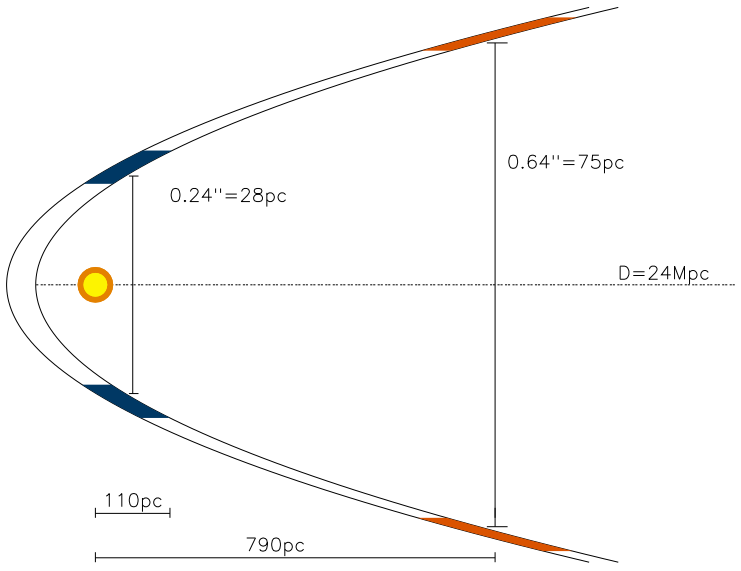

Figure 2.11: The geometry of the dust that produced the inner echo (blue) and outer light echo (orange) of SN 2007af (not to scale) for the forward scattering, ISM scenario. The outer echo for the January epoch (F555W) was created from a dust sheet 790 pc away from the SN, and the inner echo dust sheet was located 110 pc in front of the SN (shown in yellow).

Chapter 3

SN 2006X

SN 2006X was discovered on 2006 February 7.10 by Suzuki and Magliardi (2006) in Sbc galaxy NGC 4321 (M100) at $\alpha = 12^h22^m53^s.90$ and $\delta = +15°48'32''.90$ (Figure 3.1). The host galaxy distance is 15.2 Mpc, and the SN was located 12″ W and 48″ S of the center (Wang et al., 2008). SN 2006X was spectroscopically classified as a redder SN 2002bo-like Type Ia supernova (Benetti et al., 2004) discovered 1 – 2 weeks premaximum by Quimby et al. (2006). High Si II (6355Å) levels were present in the spectra with a line velocity of 20,700 km s^{-1}.

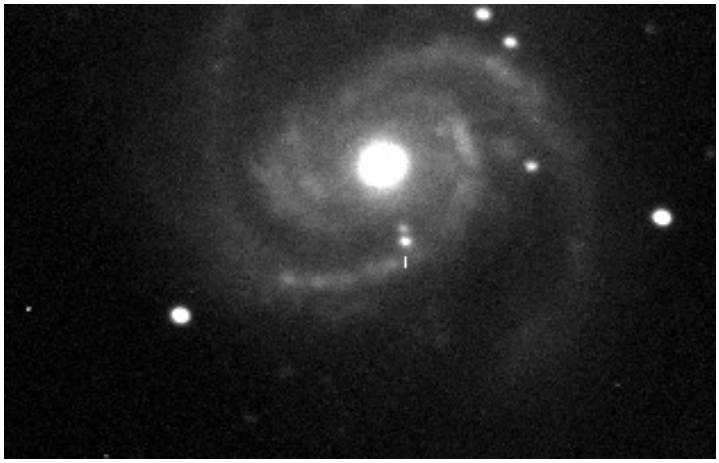

Figure 3.1: Discovery image of SN 2006X (above white hash) in host galaxy NGC 4321 (Suzuki and Magliardi, 2006).

3.1 Early Epoch Observations and Reductions

$BVRI$ early epoch observations of SN 2006X (-11.27 d – +116.32 d) were reported in Wang et al. (2008). Three telescopes were used for this survey: the 0.8m THCA-NAOC Telescope (TNT) at Beijing Xinglong Observatory in China, the 0.76m Katzman Automatic Imaging Telescope (KAIT) at Lick Observatory, and the 1.3m telescope at Cerro Tololo Inter-American Observatory (CTIO) in Chile. The TNT observations were taken with a 1340 x 1300 pixel CCD with a field of view of $11.5'$ x $11.2'$ ($0.52''$ pix^{-1}). KAIT observations utilized an Apogee AP7 camera with a field of view of $6.6'$ x $6.6'$ ($0.79''$ pix^{-1}). CTIO observations were obtained using ANDICAM, a dual-channel optical/near-infrared camera, with an optical field of view of $6.3'$ x $6.3'$ ($0.37''$ pix^{-1}). Host galaxy subtraction was performed from template images of NGC 4321 taken with KAIT and TNT taken 2007 March 14 and 16, one year after discovery, to minimize SN–galaxy light contamination for early-epoch photometry. Magnitudes were obtained by performing PSF-fitting photometry on the SN and standard stars using the IRAF DAOPHOT package and Landolt transformations (Landolt, 1992).

Polynomial fit to the B band light curve resulted in a maximum brightness of 15.40 ± 0.03 mag on 2006 February 19.93 ± 0.35 d. V peak of 14.04 ± 0.02 mag was reached on 2006 February 22.80 ± 0.29 d. At maximum light, $B - V = 1.36 \pm 0.04$ mag. The I filter peaked at 13.29 ± 0.02 mag. Taking reddening into account, $\Delta m_{15}(B) = 1.17 \pm 0.05$ mag. Twelve days after maximum $B - V = 1.83 \pm 0.05$ mag, which is much redder than typical SNe Ia with similar $\Delta m_{15}(B)$ values, suggesting significant line-of-sight reddening. See Tables 3.1 and 3.2 for photometry results from this team.

BV observations of SN 2006X from the Carnegie Supernova Project (CSP) were also added to the light curve (Contreras et al., 2010). Photometric monitoring was obtained at the Las Campanas Observatory (LCO) in Chile. Follow-up observations were obtained with the SITe3 CCD camera on the Swope 1m telescope. The du Pont Telescope was used for host galaxy template observations taken at least a year after maximum for galaxy subtraction. Forty-one optical epoch observations were taken as part of the survey (Table 3.3). The optical images were reduced with IRAF using the CCDPROC task. Magnitudes were derived differentially with local stars on a minimum of three photometric nights using Landolt standard stars (Landolt, 1992). Instrumental magnitudes of local stars and the SN were obtained with PSF fitting.

Table 3.1: SN 2006X Early Epoch Optical Observations

JD	B (mag)	err(B) (mag)	V (mag)	err(V) (mag)	R (mag)	err(R) (mag)	I (mag)	err(I) (mag)
2453774.90	17.111	0.023	15.679	0.019	14.832	0.019	14.745	0.020
2453775.33	17.005	0.018	15.566	0.014	14.721	0.013	14.489	0.017
2453775.85	16.701	0.020	15.421	0.019	14.574	0.015	14.416	0.021
2453776.19	16.626	0.019	15.320	0.014	14.476	0.013	14.318	0.017
2453776.86	16.484	0.021	15.146	0.020	...	...	...	...
2453776.96	16.386	0.054	15.154	0.018	14.327	0.021	14.150	0.024
2453777.38	16.297	0.015	15.012	0.014	14.207	0.012	13.925	0.016
2453778.38	16.060	0.018	14.797	0.015	14.032	0.013	13.731	0.017
2453778.75	15.994	0.019	14.813	0.018	14.043	0.014	13.781	0.022
2453779.80	15.778	0.020	14.545	0.020	...	...	...	...
2453780.39	15.741	0.017	14.469	0.015	13.786	0.013	13.443	0.017
2453782.40	15.633	0.041	14.343	0.017	13.660	0.013	13.300	0.019
2453783.80	15.389	0.020	14.166	0.020	13.619	0.015	13.298	0.015
2453784.27	15.441	0.014	14.146	0.014	13.552	0.013	...	...
2453784.76	15.406	0.020	14.178	0.020	13.586	0.015	13.297	0.015
2453785.25	15.431	0.015	14.094	0.014	13.521	0.013	13.283	0.016
2453786.19	15.407	0.014	14.059	0.014	13.499	0.012	13.290	0.016
2453787.78	15.418	0.028	14.070	0.023	13.518	0.015	13.354	0.015
2453787.84	15.466	0.015	14.068	0.017	13.524	0.013	13.409	0.018
2453788.27	15.441	0.014	14.024	0.014	13.477	0.012	13.323	0.016
2453788.82	15.494	0.015	14.054	0.020	13.513	0.014	13.412	0.022
2453789.25	15.499	0.014	14.013	0.014	13.476	0.013	13.338	0.016
2453789.85	15.553	0.015	14.063	0.017	13.526	0.015	13.444	0.018
2453790.23	15.542	0.014	14.025	0.014	13.507	0.012	13.376	0.016
2453790.78	15.585	0.032	14.111	0.020	13.570	0.015	13.468	0.015
2453790.83	15.618	0.015	14.062	0.014	13.543	0.041	13.496	0.030
2453792.23	15.685	0.014	14.063	0.014	13.579	0.012	13.461	0.016
2453793.23	15.771	0.016	14.085	0.014	13.620	0.013	13.508	0.017
2453793.83	15.805	0.020	14.126	0.018	13.712	0.015	13.645	0.015
2453795.34	15.943	0.015	14.186	0.014	13.784	0.012	13.643	0.016
2453797.39	16.136	0.015	14.335	0.014	13.949	0.013	13.749	0.017
2453799.39	16.338	0.015	14.428	0.014	14.040	0.013	13.757	0.017
2453799.74	16.473	0.031	14.488	0.041	14.048	0.015	13.938	0.023
2453800.32	16.462	0.016	14.516	0.014	14.078	0.012	13.742	0.016
2453801.22	16.562	0.016	14.562	0.014	14.083	0.012	13.729	0.016
2453802.23	16.654	0.019	14.610	0.015	14.082	0.013	...	...
2453802.73	16.790	0.020	14.682	0.017	14.103	0.015	13.864	0.015
2453803.22	16.760	0.018	14.631	0.014	14.084	0.013	13.661	0.017
2453806.16	17.240	0.045	14.777	0.016	14.096	0.013	13.603	0.017
2453806.74	17.303	0.030	14.899	0.020	14.138	0.015	13.740	0.015
2453808.25	17.243	0.095	14.821	0.017	...	...	13.575	0.018
2453810.31	17.506	0.104	14.930	0.020	14.135	0.015	...	...
2453810.70	17.743	0.108	15.045	0.018	14.200	0.015	13.650	0.015

Table 3.2: SN 2006X Early Epoch Optical Observations Continued

JD	B (mag)	err(B) (mag)	V (mag)	err(V) (mag)	R (mag)	err(R) (mag)	I (mag)	err(I) (mag)
2453813.23	17.697	0.024	15.120	0.014	14.214	0.012	13.518	0.016
2453813.82	17.729	0.042	15.221	0.017	14.313	0.014	13.603	0.018
2453814.71	17.945	0.054	15.388	0.015	14.433	0.015	13.709	0.015
2453815.24	17.884	0.022	15.245	0.014	14.350	0.013	13.566	0.018
2453816.80	17.878	0.039	15.454	0.016	14.538	0.015	13.792	0.025
2453817.19	17.948	0.018	15.432	0.014	14.510	0.012	13.741	0.016
2453818.15	18.030	0.023	15.509	0.014	14.588	0.013	13.818	0.016
2453818.72	18.091	0.033	15.607	0.033	14.722	0.015	13.976	0.015
2453820.17	18.166	0.020	15.631	0.014	14.735	0.012	13.976	0.016
2453821.77	99.999	9.999	15.749	0.017	14.871	0.030	14.170	0.043
2453823.20	18.132	0.035	15.769	0.015	14.884	0.013	14.156	0.016
2453824.16	18.188	0.029	15.814	0.015	14.949	0.013	14.215	0.016
2453824.77	18.206	0.030	15.923	0.042	15.116	0.015	14.371	0.011
2453825.10	18.278	0.052	15.839	0.017	14.987	0.013	14.265	0.017
2453827.18	18.306	0.043	15.885	0.016	15.091	0.013	14.377	0.017
2453828.20	18.261	0.028	15.922	0.015	15.088	0.013	14.429	0.017
2453829.25	18.210	0.110	15.984	0.034	15.153	0.014	14.475	0.018
2453830.15	18.287	0.027	15.997	0.015	15.171	0.013	14.516	0.016
2453833.24	18.315	0.043	16.080	0.017	15.285	0.013	14.651	0.017
2453836.60	18.471	0.086	16.288	0.025	15.445	0.022	14.913	0.053
2453838.14	...	...	...	...	15.382	0.037	14.824	0.027
2453841.65	18.523	0.053	16.440	0.014	15.689	0.013	15.176	0.010
2453843.72	18.443	0.054	16.386	0.019	15.670	0.015	15.173	0.028
2453845.13	18.487	0.023	16.440	0.015	15.695	0.013	15.171	0.017
2453846.63	18.444	0.032	16.541	0.014	15.771	0.013	15.299	0.015
2453850.19	18.492	0.062	16.538	0.023	15.826	0.015	15.300	0.022
2453852.65	18.519	0.041	16.699	0.019	15.947	0.015	15.576	0.018
2453852.68	18.506	0.070	16.645	0.018	15.949	0.013	15.514	0.021
2453854.08	18.555	0.038	16.670	0.018	16.015	0.014	15.561	0.018
2453858.62	18.599	0.040	16.868	0.033	...	...	...	...
2453859.04	18.598	0.064	16.780	0.025	16.139	0.016	15.748	0.020
2453864.66	18.818	0.105	16.962	0.054	...	...	...	...
2453866.07	18.589	0.229	16.931	0.053	16.368	0.023	15.978	0.024
2453870.07	18.622	0.061	17.091	0.024	16.488	0.016	16.096	0.020
2453873.58	18.662	0.023	17.249	0.011	...	...	...	...
2453879.16	18.719	0.147	17.314	0.043	16.721	0.026	16.494	0.040
2453881.60	18.773	0.020	17.419	0.010	...	...	...	...
2453884.16	18.719	0.147	17.314	0.043	16.721	0.026	16.494	0.040
2453894.08	19.025	0.179	17.643	0.032	17.279	0.023	16.878	0.041
2453901.08	18.886	0.054	17.789	0.029	17.462	0.023	17.064	0.045
2453903.03	19.033	0.199	17.969	0.028	17.527	0.016	17.383	0.021

Table 3.3: CSP Early Epoch Optical Observations

JD	B (mag)	err(B) (mag)	V (mag)	err(V) (mag)
2453775.69	16.690	0.007	15.487	0.005
2453778.86	15.895	0.007	14.796	0.006
2453780.87	15.598	0.009	14.514	0.006
2453783.73	15.396	0.007	14.263	0.006
2453784.83	15.366	0.007	14.207	0.006
2453785.80	15.352	0.008	14.171	0.008
2453786.83	15.349	0.006	14.138	0.006
2453788.84	15.406	0.007	14.111	0.006
2453790.81	15.495	0.007	14.113	0.006
2453795.78	15.891	0.006	14.326	0.004
2453798.81	16.212	0.007	14.544	0.006
2453799.80	16.308	0.006	14.609	0.004
2453802.78	16.636	0.008	14.776	0.006
2453804.77	16.837	0.008	14.863	0.006
2453805.73	16.925	0.011	14.911	0.006
2453809.75	17.249	0.023	15.094	0.008
2453815.73	17.723	0.014	15.481	0.007
2453818.78	17.894	0.015	15.712	0.007
2453819.75	17.960	0.013	15.777	0.008
2453824.76	18.099	0.013	15.981	0.006
2453831.72	18.181	0.014	16.206	0.009
2453832.77	18.207	0.013	16.235	0.007
2453835.66	18.237	0.016	16.319	0.007
2453838.71	18.260	0.041	16.411	0.008
2453841.72	18.335	0.022	16.496	0.009
2453845.65	18.296	0.014	16.560	0.007
2453850.66	18.360	0.014	16.704	0.006
2453853.66	18.405	0.013	16.795	0.007
2453858.61	18.486	0.026	16.920	0.009
2453862.68	18.499	0.021	17.018	0.009
2453866.61	18.480	0.023	17.108	0.009
2453870.65	18.602	0.034	17.217	0.009
2453872.64	18.604	0.018	17.251	0.010
2453886.56	18.812	0.009	17.614	0.007
2453890.60	18.892	0.024	17.656	0.010
2453891.60	18.862	0.025	17.693	0.011
2453893.56	18.922	0.017	17.742	0.007
2453894.58	18.879	0.027	17.767	0.009
2453897.55	18.942	0.016	17.816	0.007
2453898.56	18.960	0.016	17.837	0.008
2453906.46	19.194	0.021	17.975	0.013

Lastly, we use BV observations performed on 24 photometric nights (-10 d – +91d) taken from Yamanaka et al. (2009) for completing the light curve of SN 2006X (Table 3.4). Two telescopes were used for this monitoring: the 0.6m reflector equipped with an ST-9 imager at Nishi-Harima Astronomical Observatory (NHAO) and the 0.51m telescope equipped with a CCD camera at Osaka Kyoiku University (OKU). Data reduction was performed using standard IRAF procedures, and magnitudes were determined from aperture photometry. Color excesses of E($B - V$) = 1.26 ± 0.17 mag, E($V - R$) = 0.64 ± 0.13 mag, and E($V - I$) = 1.23 ± 0.26 mag were determined.

Table 3.4: Early Epoch Optical Observations

JD	B (mag)	err(B) (mag)	V (mag)	err(V) (mag)
2453777.61	16.03	0.13	14.88	0.03
2453778.65	15.54	0.13	14.61	0.01
2453783.61	15.39	0.02	14.16	0.01
2453787.65	15.32	0.09	13.96	0.02
2453790.66	15.54	0.05	14.04	0.01
2453792.73	...	...	14.03	0.01
2453793.65	15.71	0.09	14.13	0.02
2453793.77	...	...	14.29	0.01
2453796.72	16.06	0.08	14.34	0.02
2453800.80	16.43	0.02	14.64	0.01
2453801.56	16.44	0.08	14.64	0.04
2453801.61	...	...	14.65	0.05
2453802.76	16.52	0.17	14.72	0.01
2453811.62	...	...	15.02	0.04
2453813.81	...	...	15.21	0.02
2453814.62	...	...	15.24	0.06
2453818.64	...	...	15.52	0.04
2453825.61	...	...	15.88	0.10
2453828.58	...	...	15.93	0.09
2453828.71	...	...	15.96	0.04
2453832.63	...	...	15.98	0.06
2453850.54	...	...	16.65	0.05
2453876.62	...	...	17.29	0.15

3.2 HST Observations

NGC 4321 was extensively observed for a variety of reasons with the *Hubble Space Telescope*, providing ample pre- and post-explosion images. SN 2006X featured an extended tail in B, suggesting the presence of an echo, which was discovered and further monitored in multiple observing programs

(GO 10991 and GO 11171: P.I. Arlin Crotts). These programs included three epochs of SN 2006X (+87d, +304d, and +680d). The first epoch images were taken on 2006 May 21 with short exposures to avoid SN saturation. The Advanced Camera for Surveys High Resolution Channel (ACS HRC) observed 1480s in F435W, 1080s in F555W, and 1080s in F775W. On 2006 December 24, 920s in F435W, 520s in F555W, and 520s in F775W were observed. The last epoch occurred on 2008 January 4, and the Wide Field Planetary Camera 2 (WFPC2) was used for these observations. 1000s in F380W, 1000s in F439W, 2000s in F555W, 1000s in F702W, and 1000s in F791W were imaged. The closest available bands were chosen at each epoch of observation for comparison.

Standard *HST* pipeline procedures processed and reduced the images. After a proprietary period, these images became publicly available on the MAST archive.

3.2.1 Light Echo Observations

Two teams reported on the light echo observed in SN 2006X (Wang et al., 2008; Crotts and Yourdon, 2008). Searching the MAST archive revealed images from 2009 November 12 – 13 of SN 2006X. 270s of F775W (SDSS i'), 970s of F475W (SDSS g') and 970s of F555W (wide V) were observed as part of *HST* program 11646; P.I. A. Crotts. Surprisingly, this observing program (which also provided some of the observations for SN 1998bu, which I will discuss in Chapter 4), was entitled "Light Echoes as Probes of Supernova Type Ia Environments," but the results were never published. The light echo is located $\sim 1''$ from the published SN position. No efforts to improve the WCS on the images were undertaken.

3.2.2 Light Echo Magnitudes

The magnitudes of SN 2006X from the HST ACS images from Wang et al. (2008) (W08) were measured using both the Dolphot method (Dolphin, 2000) and Sirianni procedure (Sirianni et al., 2005). For the values quoted in Table 3.5 in the 308d epoch, the method used for magnitude determination was PSF subtraction (2 – 10 pixels), where the error listed is from the scatter of the stellar PSF. At least one bright, unsaturated stellar source was included in the Crotts and Yourdon (2008) observations for PSF comparison for magnitude determination.

For the photometry of the 2009 observations of SN 2006X, we first searched the literature for suitable standard stars in our field of view, but did not find any candidates. Since the light

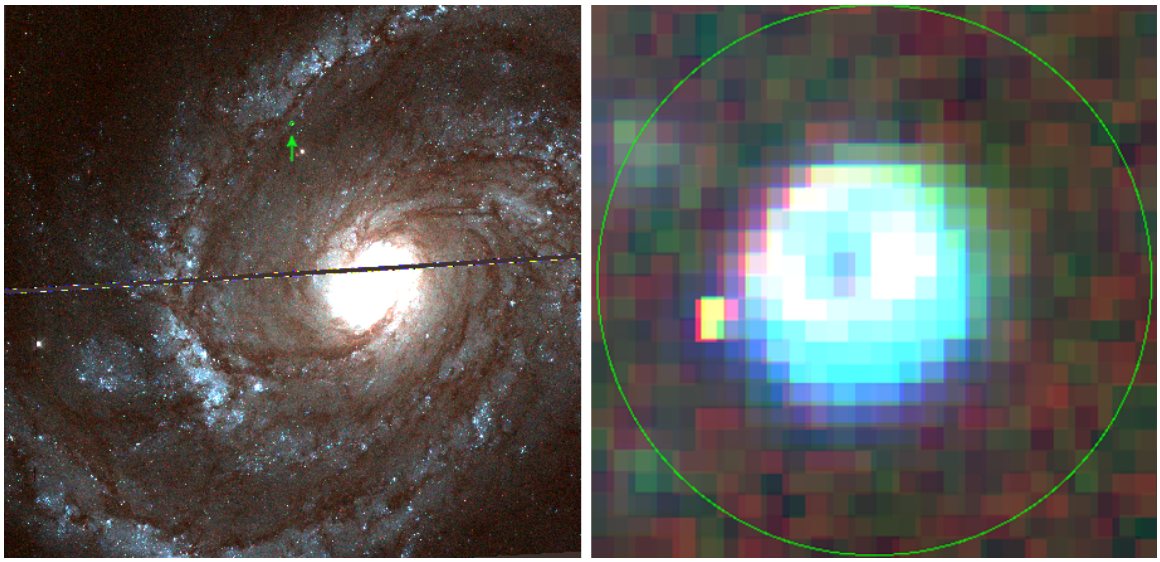

Figure 3.2: The color composite image of NGC 4321 (left panel) and 0.5″ x 0.5″ close up of the light echo (right panel). The green arrow points to the SN location (green circle) in the host galaxy image.

echo appeared as an extended object, we chose to perform aperture photometry using DAOPHOT in IRAF. Using DAOfind (see Figure 3.3), the coordinates of stellar sources were written out to a file (.coo.1). Since *HST* produces very deep and detailed images, hundreds of sources were found in each image. We manually compared the coordinates of suitable stellar sources in our images (determined with IMEXAMINE) with the entries in the coordinate file to produce a final coordinate file (Figure 3.4). The last line shows the x and y coordinates (in pixels) of the echo location. The same coordinate file was used for all three photometry calibrations.

Afterward, aperture photometry was performed using the task PHOT with various aperture sizes. The background counts were characterized from this analysis and subtracted from the counts inside the aperture ($flux = sum$ - $area$*$msky$), where sum is the total number of counts including background in the aperture, $area$ is the area of the aperture in square pixels, and $msky$ is the background estimate (per pixel). The counts were converted to VEGA magnitudes using the appropriate VEGA zeropoints from the WFC3 Instrument Manual (in the same manner as mentioned in the previous chapter). The VEGA magnitude zeropoint values (VEGA_{zpt}) used in our conversions were 25.778 mag for F475W, 25.816 mag for F555W, and 24.474 mag for F775W. We used Equation 3.1 for our magnitude determination since the magnitude calculation in the .mag files includes an extra factor of 2.5log(exptime), which has already been accounted for in the *HST* calibrations. This pro-

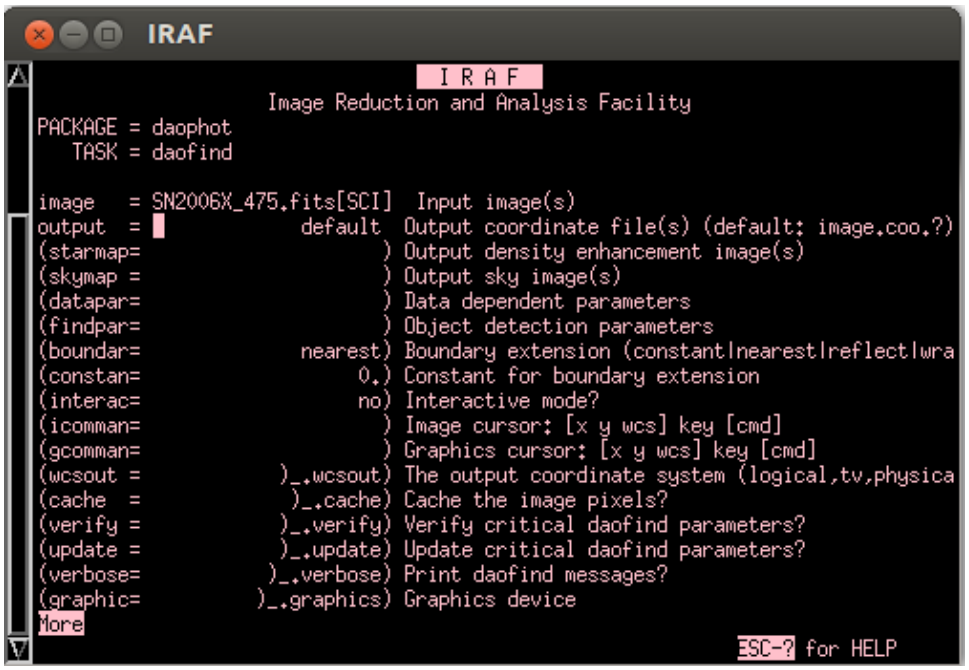

Figure 3.3: Running DAOfind on the F475W observation of SN 2006X. This produces a file with the coordinates of all the stellar sources in the image.

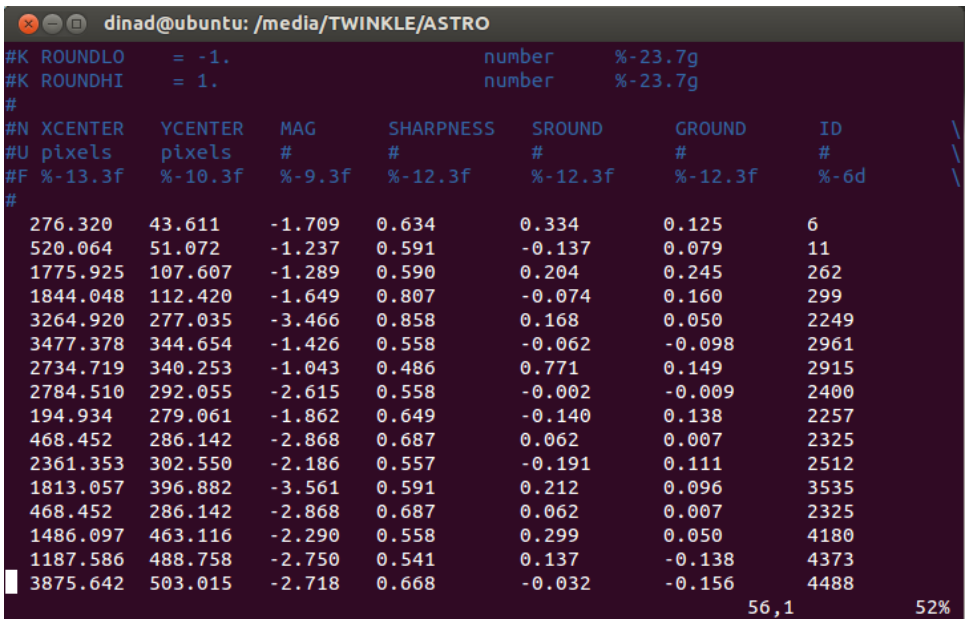

Figure 3.4: An excerpt from the coordinate file of stellar sources used in the magnitude determination of the light echo in all three filters.

cedure was also used for SN 1998bu and SN 2009ig. Table 3.5 shows the multi-epoch comparisons of the light echo magnitudes among the three teams. Epochs are relative to B-band maximum.

$$-2.5log(flux) + VEGA_{zpt} \tag{3.1}$$

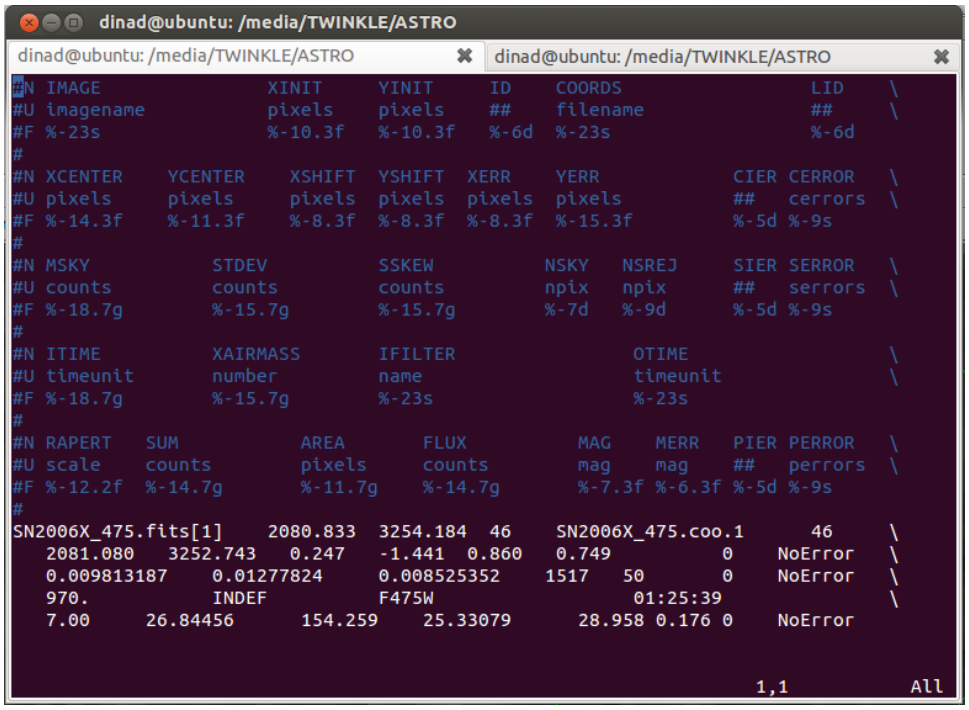

Figure 3.5: An excerpt from the photometry file for the F475W band image of SN 2006X. Note, we only used the flux values listed for our photometry determinations, not the magnitude.

Table 3.5: Light Echo Photometry Comparisons

Epoch (days past maximum)	F475W (mag)	F555W (mag)	F775W (mag)
308	22.7 ± 0.1	21.9 ± 0.3	22.1 ± 0.9
683	...	22.0 ± 0.1	...
1362	22.3 ± 0.1	21.9 ± 0.1	21.7 ± 0.1

3.2.3 Light Curve

Figure 3.6 shows the $BVRI$ light curves of SN 2006X including early- and late-epoch light echo observations plotted over normal SN 1992A (dashed line) (Suntzeff, 1996). Our 2009 *HST* images are labeled with filled blue (F475W), black (F555W), and red diamonds (F775W). The W08 and Crotts and Yourdon (2008) echo observations are shown in filled circles. Early SN 2006X observerations, taken from the literature, complete the light curve: Wang et al. (2008) ($BVRI$-open triangles), Contreras et al. (2010) (BV-open diamonds), and Yamanaka et al. (2009) (BV-open squares).

Unlike SN 2007af, the SN 1992A template required significant manipulation to fit the light curves. This is due to the highly reddened nature of the supernova. W08 reported the $E(B-V)_{host}$ = 1.42 ± 0.04 mag using an abnormal dust law of R_V = 1.48 ± 0.06. The light curve shows the plateau in the magnitudes in BVI attributed to the light echo. The data points at ∼300 days past maximum from W08 are the light echo values and not the SN emission magnitudes. Those were emitted from the light curve to eliminate confusion.

3.3 Light Echo Geometry

The light echo from SN 2006X was analyzed at three epochs, which allows for more detailed analysis. Comparisons can be made between dust sheet distance derivations. Most importantly, the evolution of the size of the echo can be investigated. In this section, we compare and contrast the findings of the three teams in relations to the angular size and geometry of the echoes.

3.3.1 Angular Size and Dust Sheet Distance

The angular size of the light echo from SN 2006X at an epoch of 308d past maximum was determined by W08 using the analysis of the radial profile and the PSF subtracted image. A ring of size ∼0.08″ with possible width of ∼0.03″ was found. This team proposed a CSM component from a possible emission within 2.0 pixels and extending upwards to 5 pixels. Using ct = 0.27 pc, a distance between the dust sheet and the SN was determined to be ∼27 – 170 pc.

On the contrary, Crotts and Yourdon (2008) found no evidence of a CSM component in their observations 680d past maximum. They subtracted a point source from the images, which left a circular residual (light echo). The pixel brightness increased from the SN location out to a radius

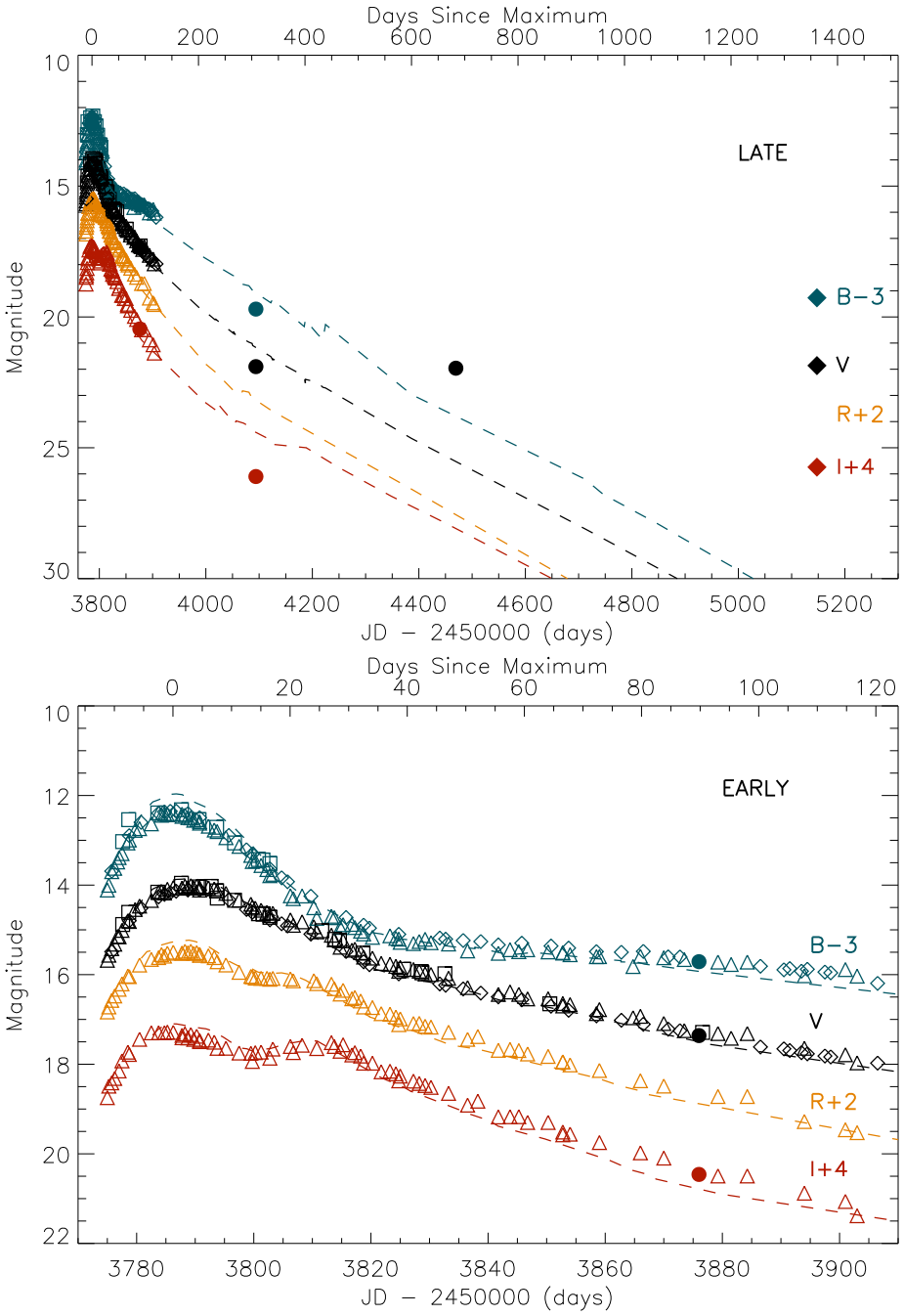

Figure 3.6: Early (lower panel)- and complete (upper panel) $BVRI$ light curves of SN 2006X plotted over normal SN 1992A (dashed line) (Suntzeff, 1996). The 2009 *HST* images are labeled with filled blue (F475W), black (F555W), and red (F775W) diamonds. The earlier epoch light echo observations are distinguished by filled circles (Wang et al., 2008; Crotts and Yourdon, 2008). The W08 light echo observation is plotted in place of the SN observation at the same epoch. Early SN 2006X observations were taken from the literature: Wang et al. (2008) ($BVRI$-open triangles), Contreras et al. (2010) (BV-open diamonds), and Yamanaka et al. (2009) (BV-open squares).

of 0.075″. To determine the angular radius of the light echo, they convolved a infinitesimally thin annular ring of constant radius with the PSF and subtracted it from the image. This resulted in a ring radius of 1.65 ± 0.1 pixels = 0.075″ ± 0.005 (see Figure 3.7). From this geometry, a dust sheet distance of 26.3 pc was determined. Note, this is a significantly different method of measuring the angular size than our and the W08 analyses. Thus, those results feature a smaller angular size and distance.

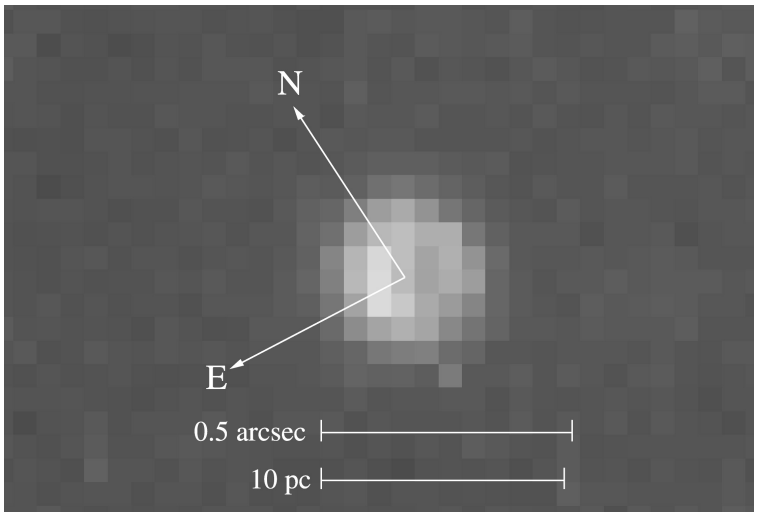

Figure 3.7: The WFPC2 PC image of the light echo of SN 2006X at 680d past maximum (Crotts and Yourdon, 2008). This image is 4000s of exposure, summing the median-summed images from the F555W, F702W, and F791W filters. The echo ring extends to 11 pc in diameter.

For the 2009 images of the light echo (t > 5yrs past maximum), we utilized IMEXAMINE in IRAF to estimate the angular size (see Figure 3.8). Then, we adjusted the green circular region using the analysis software Chandra Interactive Analysis of Observations (CIAO) (Fruscione et al., 2006) and ds9 to determine the angular extent of the echo. This was done with care to not include the artifact on the bottom left. The size of the light echo was constant in each filter. The echoes showed remarkable similarity in the F475W and F555W filters, while the F775W filter showed more structure (Figure 3.9). The angular size comparisons are in Table 3.6. Note the $\theta(''){*}$ refers to the PSF subtracted angular size of the echo. Figure 3.10 shows the growth of the echo over time, which is consistent with the model. As mentioned above, the middle data point from Crotts and Yourdon (2008) was determined using a different method and has only been included on the plot for completeness.

Using a distance of 15.2 Mpc to NGC 4321, ct = 1.14 pc, and Equation 2.1, the distance between the dust sheet and SN was determined. The average distance determined was 80 ± 5pc. The dust sheet distance comparisons are listed in Table 3.7. The geometry of the echo can be seen in Figure 3.11.

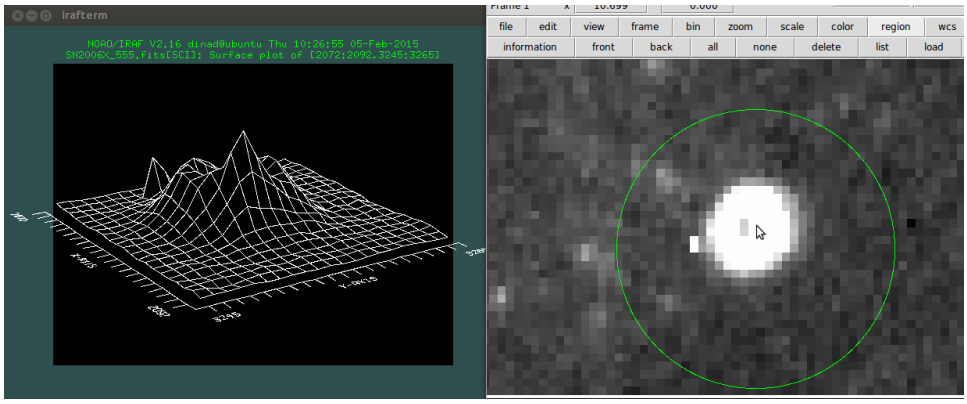

Figure 3.8: The surface plot of the SN 2006X light echo in 2009 from the IRAF package IMEXAMINE.

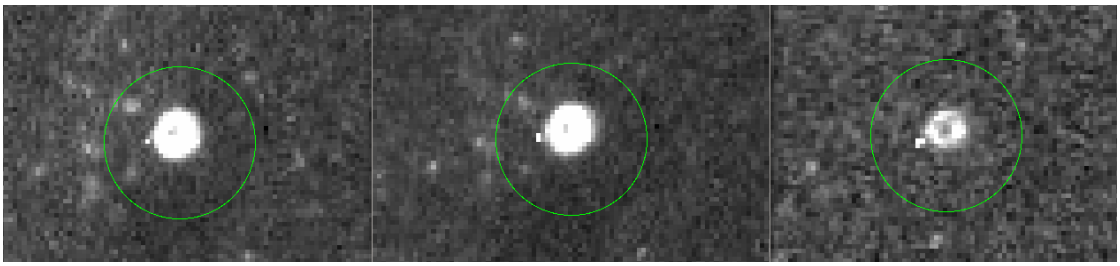

Figure 3.9: The light echo in F475W (left panel), F555W (middle panel), and F775W (right panel). Visually, the light echo in the first two filters are similar, while the F775W image has a defined ring structure. The artifact in the bottom left edge of the echo is present in each filter.

3.4 Dust Analysis

SN 2006X was extremely reddened at peak, and an abnormal dust was considered to describe the color. Using peak information from Wang et al. (2008), $R_V = A_V/E(B-V)$, and $E(\lambda - V) = A_\lambda - A_V$, the extinction laws for B, V, and I were found and are listed in Table 3.8. Δm_{obs} refers to the light echo-peak magnitude difference, and Δm_{corr} is the echo–peak magnitude corrected using $\Delta m_{corr} = \Delta m_{obs} + A_\lambda$.

Table 3.6: Angular Size Comparisons

Filter	R(pix)	$\theta('')$	$\theta('')$*	t(yrs)
F435W, F555W, F775W	2 – 5	...	0.05 – 0.13	0.84
F555W	1.65	...	0.075 ± 0.005	1.87
F475W	6.08	0.24 ± 0.01	0.19 ± 0.01	3.73
F555W	6.17	0.24 ± 0.01	0.19 ± 0.01	3.73
F775W	5.54	0.22 ± 0.01	0.17 ± 0.01	3.73

Table 3.7: Dust Sheet Distances

Filter	t(yrs)	d(pc)
F435W, F555W, F775W	0.84	∼27 – 170
F555W	1.87	26.3 ± 3.2
F475W	3.73	85.4 ± 9.6
F555W	3.73	85.4 ± 9.6
F775W	3.73	68.3 ± 8.3

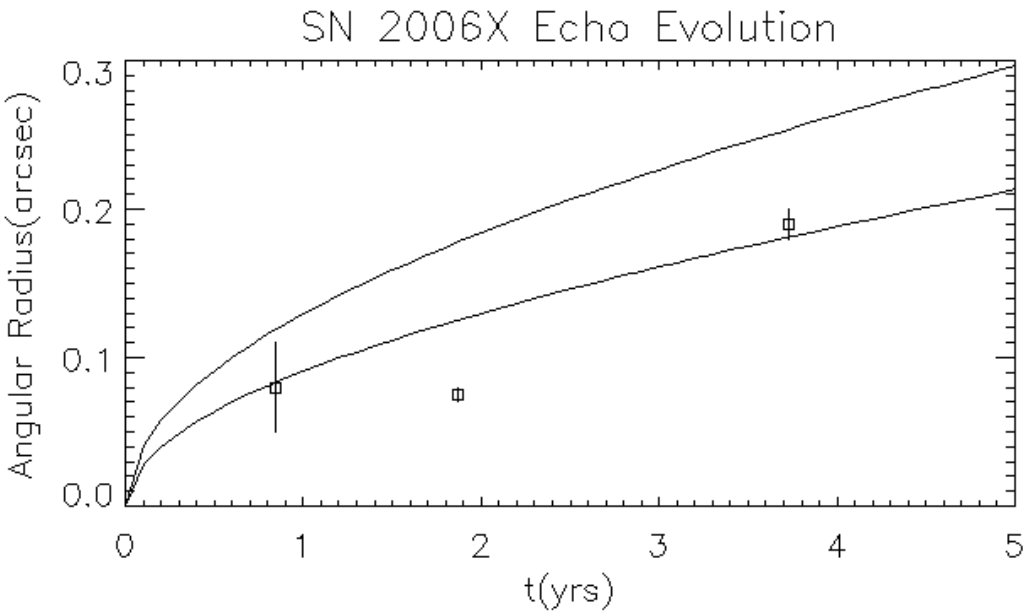

Figure 3.10: The angular size of the light echo from SN 2006X is plotted versus time and shows the agreement of the angular sizes to the model. The two curves represent the upper and lower limits of the dust distance derive from our analysis. The middle point refers to the Crotts and Yourdon (2008) angular size, which was determined by a different method than the other two. We only include this observation for completeness and comparison.

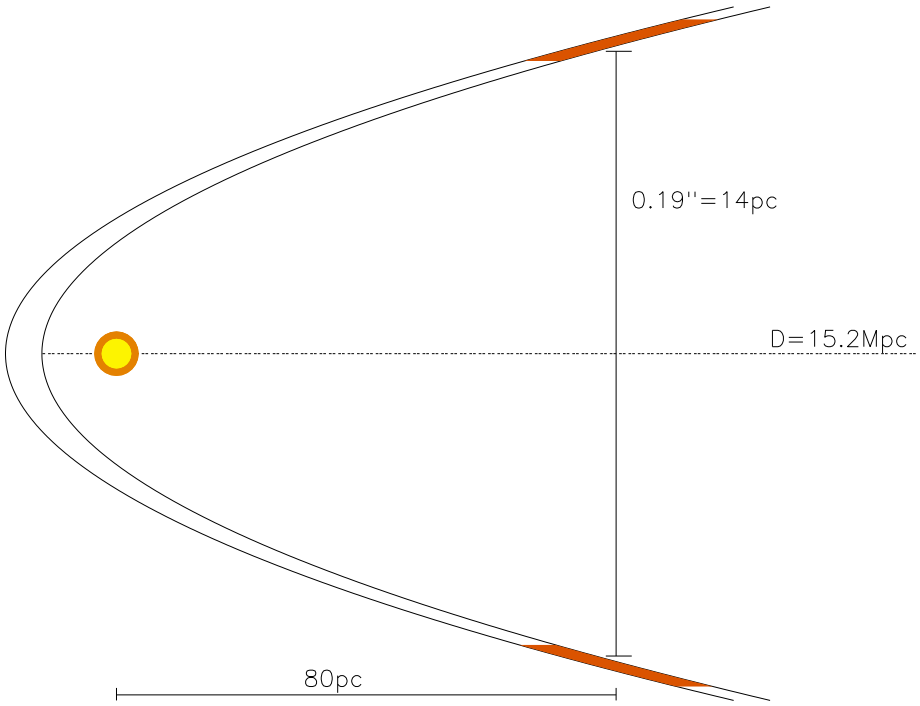

Figure 3.11: At nearly four years after the explosion of the SN, the distance between the dust and SN 2006X is estimated to be 80 pc (not to scale). Following the same labeling convention, the orange coloring refers to the intersection of the dust sheet with the time paraboloid that created the light echo seen at this epoch.

3.4.1 Optical Depth

Optical depths were calculated using the corrected change in magnitude and the distance between the dust sheet and the SN. Due to the highly reddened nature of the SN at peak, both single (τ_{ss}) and multiple scattering (τ_{ms}) were used in this analysis. For single scattering, optical depth can be calculated by Δm $\sim$ -2.5log(0.3$\frac{\tau}{d}$). For multiple scattering, Δm $\sim$ -2.5log($\frac{0.3}{d}e^{-\tau}$) was utilized with the values in Table 3.9. The last column refers to the total optical depth (scattering and absorption included) in each wavelength calculated from $A_\lambda = 1.086\tau_\lambda$.

Table 3.8: Observed and Corrected Peak-Echo Magnitudes

Filter	Δm_{obs} (mag)	A_λ	Δm_{corr}
B	6.90 $\pm$ 0.10	3.52	10.42 $\pm$ 0.10
V	7.86 $\pm$ 0.10	2.10	9.96 $\pm$ 0.10
I	8.41 $\pm$ 0.10	0.84	9.25 $\pm$ 0.10

Table 3.9: Optical Depth of Dust

Filter	τ_{ss}	τ_{ms}	τ_λ^{Tot}
F475W	0.11	3.86	3.24
F555W	0.07	2.21	1.93
F775W	0.16	1.82	0.77

3.4.2 Light Echo Color

For our light echo color analysis, we expanded on the Patat (2005) model to predict the light echo colors in *HST* filters for various scattering angles. This was the same method used for the light echo color predictions in SN 2007af (Drozdov et al., 2014). We will describe the code in detail in this subsection.

The inputs of the code are the transmission filter throughputs, the peak SN spectrum, a comparison spectrum (we used the standard star, Vega), and dust cross-sections for various dust types and scattering angles (Draine, 2003). To output a color in *HST* filters, the specific transmission functions were utilized (obtained from the appropriate instrument handbook). These filter response functions describe the percent of photons that pass through the filter at those wavelengths, and we show the curves for the WFC3 F475W (blue), F555W (green), and F775W (red) filters overplotted

on the normalized peak SN 2006X spectrum in Figure 3.12. Since the HST filters are wider than standard filters, this method provides much more accurate colors for HST observations than the method outlined in (Patat, 2005).

The SN 2006X peak spectrum was downloaded from the Asiago Supernova Catalogue taken only +2 days after maximum light (2006 February 21) and covered a wavelength range from 3293 – 10535Å(Barbon et al., 1999). The spectrum was obtained on the Lick Shane 3.0-m telescope using the Kast Double Spectrograph and Camera on 2006 February 21 at Lick Observatory (W08). For the code to produce a theoretical color for the echo, the peak spectrum had to cover the wavelength range of the transmission throughputs. In the case of SN 2006X, that meant a spectrum with a range of at least 3900 – 8600Å. The filter responses, peak, and Vega spectrum were all interpolated to create smooth curves on the same grid. As is clear from Figure 3.12, the transmission curves poorly fit the spectrum at bluer wavelengths. In particular, the F475W (blue) and F555W (green) transmission curves cover a wavelength range filled with broad absorption features. Note that we also ran the code with a spectrum taken on the day of maximum brightness (with shorter wavelength range), but the results did not change significantly (<0.01 mag).

The transmission filter responses are folded into the Vega and SN peak light spectra in whichever filter is chosen for the color. The SN spectrum is then scattered using 0°, 90°, and 180° dust cross-sections (σ) from Draine (2003) and integrated over all wavelengths. The cross sections vary for the different dust types, and we use LMC ($R_V = 2.6$), SMC Bar ($R_V = 2.87$), and MW ($R_V = 3.1$) dust in our analysis. The SN peak spectrum is weighted by the flash durations (Δt) of the filters chosen and corresponds to the span of time (in the respective filter) on both sides of maximum light for the light curve for the SN to decline by one magnitude. Since the explosion of a SN is not a delta function, we must characterize the width of the light curve at peak to accurately predict the light echo color, and thus, we need to scale the SN spectrum by the flash duration. The flash durations of SN 2006X in each filter were estimated using the light curve and photometric observations listed in Wang et al. (2008). SN 2006X was a broad SN, and the flash durations are as follows: 22.4 days (0.061 yr) in B, 33.3 days (0.091 yr) in V, and 47.3 days (0.130 yr) in I. The theoretical light echo colors were determined by comparing the SN scattered spectrum weighted with the flash durations in each filter with the Vega scattered spectrum and summing over all wavelengths. Then, we simply calculate the colors by taking -2.5*log of each sum. The echo colors were calculated with Equation 3.2, where B and V can be substituted for any desired HST or standard filter.

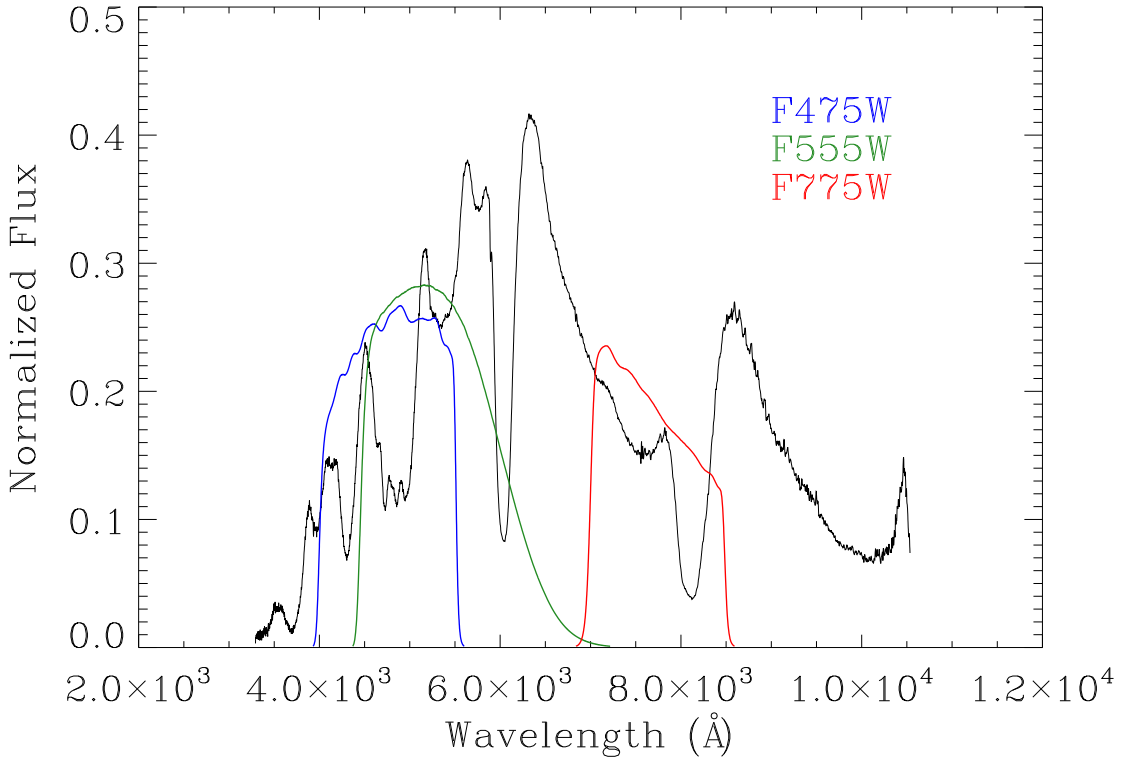

Figure 3.12: The normalized SN 2006X spectrum is shown (black line) with the *HST* filter transmission curves (from the WFC3 instrument handbook) superimposed (Barbon et al., 1999). The F475W (blue), F555W (green), and F775W (red) filter responses cover a regime with large absorption features, especially in the bluer filters, which translated in a color not replicable by the code.

$$(B-V)_{echo} = -2.5log\left[\frac{\int f_{\lambda}^{SN} T_{\lambda}^{B} \sigma_{\lambda} \Delta t^{B} d\lambda \int f_{\lambda}^{Vega} T_{\lambda}^{V} d\lambda}{\int f_{\lambda}^{SN} T_{\lambda}^{V} \sigma_{\lambda} \Delta t^{V} d\lambda \int f_{\lambda}^{Vega} T_{\lambda}^{B} d\lambda}\right] \tag{3.2}$$

The peak colors in HST filters are also predicted in our code using the same method without scattering the SN spectrum and scaling by the flash durations.

$$(B-V)_{peak} = -2.5log\left[\frac{\int f_{\lambda}^{SN} T_{\lambda}^{B} d\lambda \int f_{\lambda}^{Vega} T_{\lambda}^{V} d\lambda}{\int f_{\lambda}^{SN} T_{\lambda}^{V} d\lambda \int f_{\lambda}^{Vega} T_{\lambda}^{B} d\lambda}\right] \tag{3.3}$$

Table 3.10 reports the color evolution of SN 2006X in B – V and V – I from peak light, 12 days after peak (Wang et al., 2008), to light echo epochs in F475W – F555W and F555W – F775W (W08) in sequential order. As is evident by the values, SN 2006X had an extreme color at peak due to line-of-sight reddening. In the last two rows of the table, we compare light echo colors from our analysis to the photometry from W08. Although, the same HST filters were used in both campaigns, the magnitudes are quite different, yet consistent within the extreme uncertainty limits of W08.

Table 3.10: SN 2006X Color Evolution

Epoch	Observed (B – V) (mag)	Observed (V – I) (mag)
Peak	1.36 ± 0.03	0.75 ± 0.03
12d	1.83 ± 0.05	0.60 ± 0.04
Light Echo$_{W08}$	0.80 ± 0.30	-0.20 ± 0.90
Light Echo	0.40 ± 0.14	0.20 ± 0.14

Tables 3.11 and 3.12 show the results of folding the respective filters into the scattered peak spectrum of SN 2006X and comparing to the Vega spectrum. In the tables, the observed peak color (at the same +2d epoch as the spectrum) from Wang et al. (2008) is first compared to the predicted peak color (model) using Equation 3.3. Then, the observed light echo color is shown and compared to the results using 0°, 90°, and 180° single scattering. The F475W – F555W peak and light echo predictions poorly match the observed values. From the spectrum itself, the large number of broad absorption features at lower wavelengths have a drastic impact on the code and cause the large dispersion between the observed and predicted values. Although the peak and light echo color

was not replicable by our analysis, Table 3.13 shows the large magnitude differences between the B and F475W and V and F555W filters, respectively. Thus, perhaps the dispersion between the theoretical and observed values can be explained by the different filter responses between ground- and space-based observations.

Table 3.11: F475W – F555W Echo Color Predictions

	LMC R_V = 2.6 (mag)	SMC Bar R_V = 2.87 (mag)	MW R_V = 3.1 (mag)
Peak Color	Observed $B - V = 1.35 \pm 0.04$		Model F475W – F555W = 0.600
Light Echo Color		0.4 ± 0.1	
0° Predictions	0.806	0.790	0.786
90° Predictions	0.928	0.899	0.957
180° Predictions	0.778	0.830	0.889

While the observed and theoretical $B - V$ color agreed poorly, the same pattern does not hold for the results for $V - I$. Again, if we look at the peak SN 2006X spectrum, the filter responses are a better fit at redder wavelengths. The theoretical peak colors match the observations exactly, and even the theoretical scattering predictions matches the light echo color of 0.2 ± 0.1 mag. In the single scattering scenario, the light echo color is consistent with 0° scattering. Since the different dust types produce virtually the same color, we cannot discriminate between them.

Table 3.12: F555W – F775W Echo Color Predictions

	LMC R_V = 2.6 (mag)	SMC Bar R_V = 2.87 (mag)	MW R_V = 3.1 (mag)
Peak Color	Observed $V - I = 0.72 \pm 0.03$		Model F555W – F775W = 0.750
Light Echo Color		0.2 ± 0.1	
0° Predictions	0.208	0.209	0.209
90° Predictions	0.811	0.713	0.867
180° Predictions	0.688	0.698	0.910

Table 3.13 compares the *HST* and standard Bessell filters to show the magnitude difference between the ground and space standard filters for SN 2006X. Using the same code, we simply substitute B and V with Bessell and equivalent *HST* filters in the color equation (Equation 3.2), respectively. Here, we do not scale the SN spectrum by the flash duration, since they are assumed to be the same for these cases. The peak and scattering predictions are reported and show the large differences (∼0.4 mag in some cases) between the filters, illustrating the significant impact of a highly reddened SN. Again, we see the same pattern that the redder filters show much smaller differences between standard and *HST* filters, but even in the F775W filter, the peak magnitude

difference between the filters is 0.2 mag. In the future, not only must the code be amended to take extinction into account, but multiple scattering must also be considered. Since the reddening (as reported from peak information) is such a large value, the probability of the light being scattered multiple times before reaching the observer is a highly likely scenario and must be included.

Table 3.13: *HST* vs. Bessell Filters

Filter Names	Scattering Angle	Peak (mag)	$R_V = 2.6$ (mag)	$R_V = 2.87$ (mag)	$R_V = 3.1$ (mag)
B – F475W	0°	0.456	0.283	0.261	0.260
B – F475W	90°	0.456	0.370	0.341	0.389
B – F475W	180°	0.456	0.167	0.232	0.275
V – F555W	0°	-0.280	-0.225	-0.218	-0.217
V – F555W	90°	-0.280	-0.257	-0.249	-0.264
V – F555W	180°	-0.280	-0.188	-0.215	-0.232
I – F775W	0°	-0.198	0.007	0.002	-0.006
I – F775W	90°	-0.198	-0.128	-0.110	-0.122
I – F775W	180°	-0.198	-0.172	-0.138	-0.167

While there is only a ∼0.1 mag difference between the different dust types, lower R_V values do seem to fit the observed values better. This is consistent with the findings of Wang et al. (2008), which report a value of $R_V = 1.5$. For future work, we will need to consider these extreme dust types to try to replicate the light echo observed color.

Chapter 4

SN 1998bu

SN 1998bu was discovered by Villi et al. (1998) on 1998 May 9.9, located 60″ north of the center of NGC 3368 (M96). Images taken April 21.9 did not show the supernova, constraining the explosion time. A more precise location of $\alpha = 10^h46^m46^s.03$, $\delta = +11°50'07''.10$ was determined by M. Aoki using a 0.43-m reflector. The position of the SN was 4″.3 east and 55″.3 north of the center of the host galaxy. The distance to host galaxy is D = 10.5 Mpc (Lee and Jang, 2013). SN 1998bu was one of the first Type Ia supernovae to be extensively monitored in $UBVRIJHK$ due to its early detection and close proximity. Before SN 1998bu, only four SNe Ia had both Cepheid distances and extensive light curves, which made SN 1998bu a major event in the study of supernovae.

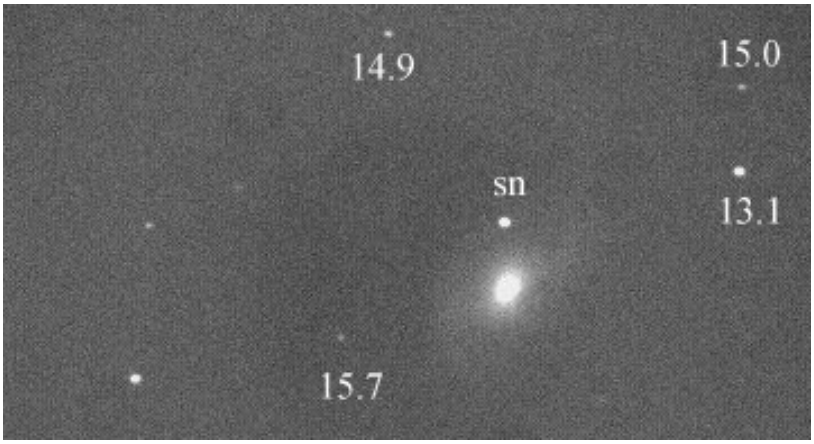

Figure 4.1: Discovery image of SN 1998bu in M96 taken on May 9th, 1998 (Villi et al., 1998).

4.1 Early Observations

The first optical campaign of SN 1998bu reported was from Suntzeff et al. (1999). Munari et al. (1998) obtained an echelle spectrum on May 12 that indicated some reddening from the strong Na I D interstellar absorption feature. The optical observations of SN 1998bu were first obtained with the Tek2048 No. 3 CCD on the 0.9-m telescope at CTIO on 1998 May 16 through July 14. Weather was not ideal during these observations due to the 1998 El Niño weather at the time, which resulted in time loss and poor seeing. The CCD used was a thinned, anti-reflection coated front-side illuminated CCD with a plate scale of $0''.40$ per pixel. Standard procedures were used to reduce the images. Bad pixel masks were created during observing to use during reductions. The CCD images were processed through DAOPHOT and ALLSTAR. Aperture photometry using an aperture diameter of 14 pixels was performed using DAOGROW with Landolt field stars (Landolt, 1992). Local standards were measured on 11 photometric nights. Since this data was reported early, no subtraction images were available, but the errors assuming a uniform galaxy brightness at the position of the SN were small. B maximum occurred ∼1–2 days before V and R maximum, while I maximum occurred before U maximum. Table 4.1 shows the summary of observations from Suntzeff et al. (1999).

Numerous (356) photometric measurements and 29 spectra of SN 1998bu were compiled by Jha et al. (1999) between 1998 May 11 and July 15 (see Tables 4.2 and 4.3). B maximum occurred on 1998 May 19.3 (JD 2450952.8 ± 0.8) at 12.22 ± 0.03 mag. The value of V maximum was 11.88 ± 0.02 mag. The measured extinction toward the supernova was $A_V = 0.94 \pm 0.15$ mag. Spectra taken by Meikle and Hernandez (2000) on May 12.9 and Ayani et al. (1998) on May 14.5 classified the object as a Type Ia supernova discovered a week before maximum light. SN 1998bu was a fortuitous discovery of a SN whose host galaxy Cepheid distance was already measured with *HST*, and thus, it was extensively monitored.

Using the Center for Astrophysics resources, SN 1998bu was monitored with the F. L. Whipple Observatory 1.5-m Tillinghast reflector, FAST spectrograph, and photometrically with the F. L. Whipple Observatory 1.2-m reflector in optical and near-infrared wavelengths using STELIRCAM. Most of the optical photometric observations were obtained with the f/8 Cassegrain focus 1.2-m telescope + 4Shooter CCD mosaic camera, which consists of a 2 x 2 array of back-side illuminated, anti-reflective coated Loral CCD detectors. The plate scale of $0''.335$ resulted in a total sky coverage

Table 4.1: SN 1998bu Early Optical Observations

JD	B (mag)	err(B) (mag)	V (mag)	err(V) (mag)	R (mag)	err(R) (mag)	I (mag)	err(I) (mag)
2450947.59	12.434	0.005	12.183	0.005	11.862	0.006	11.696	0.007
2450948.56	12.353	0.008	12.092	0.004	11.807	0.005	11.662	0.005
2450949.55	12.299	0.010	12.024	0.005	11.774	0.007	11.667	0.007
2450950.58	12.241	0.007	11.960	0.003	11.747	0.007	11.667	0.010
2450951.55	12.218	0.004	11.926	0.003	11.735	0.007	11.689	0.006
2450951.53	12.207	0.004	11.921	0.003	11.729	0.005	11.686	0.004
2450953.48	12.202	0.006	11.880	0.004	11.701	0.006	11.718	0.006
2450954.53	12.232	0.019	11.903	0.008	11.716	0.029	11.747	0.045
2450957.52	...	...	...	...	...	...	11.815	0.015
2450959.47	12.450	0.016	11.998	0.009	11.855	0.017	11.982	0.019
2450960.46		...	12.075	0.006	11.959	0.015	12.087	0.007
2450964.45	12.872	0.009	12.323	0.006	12.279	0.007	12.349	0.017
2450965.50	12.972	0.011	12.390	0.006	12.346	0.008	12.380	0.009
2450968.46	13.316	0.012	12.570	0.009	12.432	0.013	12.341	0.015
2450971.46	...	...	12.711	0.007	12.453	0.008	12.286	0.008
2450972.50	...	...	12.751	0.004	12.450	0.006	12.242	0.007
2450975.48	...	...	12.919	0.004	12.487	0.006	12.181	0.005
2450978.49	...	...	13.071	0.005	12.551	0.007	12.124	0.007
2450983.47	14.825	0.011	13.426	0.009	12.861	0.024	12.298	0.009
2450984.48	14.869	0.011	13.505	0.007	12.938	0.007	12.374	0.008
2450987.52	15.010	0.019	13.679	0.010	13.153	0.019	12.562	0.018
2450988.45	15.069	0.008	13.725	0.004	13.208	0.007	12.696	0.006
2450997.48	15.291	0.015	14.041	0.006	13.608	0.008	13.214	0.010
2450997.50	15.315	0.015	14.051	0.006	13.612	0.007	13.214	0.007
2450998.46	15.326	0.007	14.071	0.004	13.637	0.004	13.263	0.006
2450999.48	15.346	0.007	14.102	0.004	13.684	0.005	13.320	0.006
24501000.48	15.345	0.014	14.121	0.007	13.713	0.009	13.356	0.009
24501002.47	15.383	0.014	14.189	0.007	13.785	0.008	13.461	0.008
24501003.50	15.404	0.015	14.200	0.007	13.810	0.009	13.521	0.008
24501004.46	15.410	0.014	14.222	0.008	13.839	0.010	13.562	0.009
24501005.45	15.436	0.014	14.257	0.008	13.884	0.010	13.607	0.010
24501006.46	15.444	0.014	14.285	0.007	13.910	0.009	13.654	0.008
24501007.45	15.467	0.013	14.321	0.006	13.953	0.008	13.700	0.007
24501008.45	15.486	0.013	14.349	0.007	13.984	0.007	13.762	0.011

of 0.15 deg^2. The observations were taken in a 2 x 2 binned mode and had a typical seeing of $1''.5 - 2''$. More optical observations were obtained by various telescopes and instruments including KPNO telescopes and KAIT. The observations were reduced using standard procedures in the IRAF CCDPROC package. Differential photometry was performed using six field stars for comparison. Landolt standard fields were observed to calibrate the comparison stars (Landolt, 1992). Photometry of SN 1998bu was determined using aperture photometry of the SN and field stars. To improve photometry, a template of the background host galaxy flux was subtracted from the flux of the SN (Jha et al., 1999).

Finally, Hernandez et al. (2000) reported the last major $UBVRI$ observing program of SN 1998bu (Table 4.4). The bulk of the data was obtained using the 82cm Instituto de Astrofisica de Canarias Telescope (IAC80) on Tenerife, and the 1-m Jacobus Kapteyn Telescope (JKT) at La Palma Observatory. Other observations were obtained at the 2.6-m Nordic Optical Telescope (NOT) and the 3.5-m WIYN telescope at KPNO. Monitoring began at -5 days and spanned 53 days (see Table 4.4). The IAC80 images were taken with the 1024 x 1024 CCD camera with a plate scale of $0''.43$ per pixel and total field of view of $7''.3$ x $7''.3$. The JKT observations also utilize a 1024 x 1024 CCD camera with a plate scale of $0''.33$ per pixel and total field of view of $5''.6$ x $5''.6$. WIYN is equipped with a 2048 x 2048 CCD with a plate scale of $0''.20$ per pixel and total field of view of $6''.5$ x $6''.5$.

The IAC80 data was reduced using standard IRAF procedures. Data from the other telescopes were reduced using the Starlink package CCDPACK. Aperture photometry was used to determine SN magnitudes. The SN and standard star flux was measured using a circular aperture. Then, the background flux was estimated and subtracted using a concentric annulus. The SN magnitudes were compared to the magnitudes of the standard stars, which were calibrated with Landolt field stars (Landolt, 1992).

4.2 Light Echo Observations

Five hundred days after maximum, the light curve of SN 1998bu featured a plateau attributed to a light echo (Cappellaro et al., 2001). Due to the substantial reddening found at peak, this SN was monitored into the nebular phase. SN 1991T showed a similar decline of ^{56}Co, and that SN also exhibited a light echo. On 1999 December 4, SN 1998bu was two magnitudes brighter than

Table 4.2: SN 1998bu Optical Observations

JD	B (mag)	err(B) (mag)	V (mag)	err(V) (mag)	R (mag)	err(R) (mag)	I (mag)	err(I) (mag)
2450944.68	...	...	12.45	0.14	12.23	0.10	11.95	0.15
2450947.63	12.47	0.11	12.15	0.02	11.86	0.04	11.72	0.04
2450948.59	...	...	12.08	0.02	11.80	0.04	11.68	0.04
2450948.65	12.41	0.09	12.09	0.02	11.80	0.04	11.70	0.04
2450949.67	12.29	0.02	11.98	0.01	11.72	0.03	11.63	0.03
2450951.58	12.28	0.07	11.90	0.02	11.71	0.04	11.68	0.04
2450951.63	...	...	11.93	0.03	11.72	0.04	11.67	0.04
2450951.67	...	...	11.91	0.03	11.80	0.09	...	...
2450951.68	12.21	0.02	11.90	0.01	11.68	0.03	11.66	0.03
2450952.62	12.29	0.07	11.87	0.02	11.70	0.04	11.70	0.04
2450952.64	...	...	11.88	0.02	11.71	0.05	11.74	0.05
2450952.66	12.21	0.02	11.86	0.01	11.66	0.03	11.71	0.03
2450952.67	....	...	11.85	0.03	11.75	0.09	11.69	0.06
2450953.63	12.34	0.11	...	...	...	...	...	...
2450953.70	12.24	0.02	11.87	0.01	11.66	0.03	11.73	0.03
2450955.64	12.28	0.02	11.86	0.01	11.65	0.03	11.79	0.03
2450955.66	12.26	0.11	11.88	0.02	11.66	0.04	11.80	0.05
2450955.68	...	...	11.85	0.03	11.82	0.06	...	...
2450956.59	12.35	0.07	11.90	0.02	11.71	0.04	11.83	0.04
2450956.64	12.32	0.02	11.87	0.01	11.67	0.03	11.80	0.03
2450956.68	...	...	11.89	0.03	11.79	0.09	11.84	0.06
2450957.63	12.36	0.02	11.92	0.01	11.72	0.03	11.87	0.03
2450957.65	12.34	0.11	11.96	0.03	11.75	0.05	11.88	0.05
2450959.68	12.50	0.02	12.01	0.01	11.82	0.03	11.98	0.03
2450960.57	12.57	0.07	12.02	0.02	11.91	0.04	12.04	0.04
2450960.69	12.56	0.02	12.04	0.01	11.89	0.03	12.05	0.03
2450961.57	12.74	0.11	12.12	0.03	12.02	0.05	...	...
2450961.60	12.64	0.07	12.07	0.02	11.99	0.04	12.10	0.04
2450962.66	12.70	0.02	12.12	0.01	12.05	0.03	12.21	0.03
2450963.64	12.81	0.03	12.21	0.02	12.15	0.03	12.26	0.04
2450963.68	12.88	0.05	12.26	0.02	12.28	0.06	12.30	0.04
2450964.63	12.94	0.03	12.28	0.01	12.21	0.03	12.30	0.03
2450964.68	12.97	0.05	12.34	0.02	...	...	12.32	0.04
2450965.64	13.03	0.02	12.35	0.01	12.29	0.03	12.31	0.03
2450965.67	13.05	0.03	12.42	0.02	...	...	12.33	0.04
2450966.60	13.10	0.07	12.42	0.02	12.35	0.04	12.29	0.04
2450967.65	13.24	0.02	12.48	0.01	...	...	...	...
2450967.66	13.24	0.02	12.50	0.01	...	...	12.35	0.03
2450968.67	13.40	0.02	12.59	0.01	12.46	0.03	12.33	0.03
2450968.68	13.36	0.02	12.55	0.01	...	...	12.33	0.03
2450968.72	13.43	0.03	12.62	0.02	12.48	0.03	12.31	0.03
2450969.59	13.51	0.11	12.62	0.02	12.43	0.05	12.26	0.04
2450969.60	13.40	0.07	12.61	0.02	12.43	0.04	12.25	0.04

Table 4.3: SN 1998bu Optical Observations Continued

JD	B (mag)	err(B) (mag)	V (mag)	err(V) (mag)	R (mag)	err(R) (mag)	I (mag)	err(I) (mag)
2450969.65	13.51	0.02	12.64	0.01	12.47	0.03	12.31	0.03
2450969.67	13.52	0.03	12.66	0.02	12.50	0.03	12.30	0.03
2450969.69	13.53	0.05	12.66	0.02	12.50	0.06	12.32	0.06
2450969.69	13.47	0.02	12.59	0.01	...	...	12.28	0.03
2450970.69	13.59	0.02	12.64	0.01	...	...	12.25	0.03
2450971.71	13.72	0.02	12.69	0.01	...	...	12.23	0.03
2450972.65	13.84	0.02	12.74	0.01	...	...	12.20	0.03
2450972.68	13.89	0.02	12.80	0.01	12.52	0.03	12.22	0.03
2450973.58	13.95	0.11	12.80	0.02	12.45	0.05	12.16	0.04
2450973.68	14.01	0.05	...	...	12.54	0.06	12.22	0.04
2450974.67	14.11	0.03	12.87	0.02	12.51	0.04	12.19	0.04
2450978.69	14.51	0.06	13.09	0.02	12.61	0.06	12.12	0.05
2450979.70	14.60	0.06	13.14	0.03	12.64	0.06	12.14	0.05
2450980.65	14.68	0.02	13.16	0.01	12.61	0.03	12.08	0.03
2450981.66	14.74	0.02	13.25	0.01	12.69	0.03	12.12	0.03
2450981.69	14.74	0.06	13.24	0.03	12.71	0.07	12.14	0.05
2450982.60	...	...	13.30	0.03	12.79	0.06	12.13	0.05
2450982.65	14.81	0.02	13.30	0.02	12.75	0.03	12.16	0.03
2450982.70	14.84	0.06	13.36	0.02	12.83	0.06	12.24	0.04
2450983.66	14.89	0.02	13.38	0.01	12.83	0.03	12.24	0.03
2450984.67	14.94	0.02	13.45	0.01	12.92	0.03	12.33	0.03
2450984.70	14.95	0.05	13.51	0.02	13.00	0.06	...	...
2450985.65	15.00	0.02	13.53	0.01	13.03	0.04	12.42	0.03
2450986.66	15.05	0.02	13.56	0.01	13.08	0.03	12.47	0.03
2450986.69	15.09	0.05	...	...	13.13	0.06	...	...
2450987.66	15.09	0.02	13.63	0.01	13.12	0.03	12.55	0.03
2450988.66	15.12	0.02	13.67	0.01	13.18	0.03	12.63	0.03
2450989.65	15.18	0.02	13.72	0.01	13.24	0.03	12.68	0.03
2450990.65	15.21	0.02	13.77	0.01	13.28	0.03	12.75	0.03
2450990.69	15.22	0.05	13.82	0.02	13.34	0.06	12.80	0.05
2450991.65	15.22	0.02	13.82	0.01	13.31	0.03	12.81	0.03
2450992.64	15.24	0.02	13.84	0.01	13.38	0.03	12.86	0.03
2450993.64	15.26	0.03	13.88	0.02	13.42	0.03	12.91	0.03
2450994.64	15.29	0.02	13.92	0.01	...	...	12.97	0.03
2450995.64	15.31	0.02	13.96	0.01	13.49	0.03	13.04	0.03
2450996.64	...	...	13.97	0.01	...	...	13.09	0.03

Table 4.4: Further SN 1998bu Optical Observations

JD	B (mag)	err(B) (mag)	V (mag)	err(V) (mag)	R (mag)	err(R) (mag)	I (mag)	err(I) (mag)
2450947.43	12.502	0.028	12.199	0.014	11.848	0.016	11.727	0.020
2450948.38	12.401	0.075	...	...	11.808	0.075	...	...
2450948.43	12.403	0.028	12.117	0.014	11.818	0.015	11.676	0.019
2450949.37	12.340	0.075	...	...	11.760	0.075	...	...
2450949.40	12.300	0.040	12.070	0.030	11.770	0.040	11.660	0.050
2450950.41	12.250	0.050	...	...	11.770	0.050	11.670	0.050
2450950.42	12.276	0.075	...	...	11.727	0.075	...	...
2450951.37	12.260	0.075	...	...	11.698	0.075	...	...
2450952.36	12.239	0.075	...	...	11.704	0.075	...	...
2450953.37	12.239	0.075	...	...	11.684	0.075	...	...
2450954.37	12.250	0.075	...	...	11.682	0.075	...	...
2450955.36	12.265	0.075	11.881	0.075	11.713	0.075	11.827	0.075
2450956.40	12.326	0.075	11.907	0.075	11.721	0.075	11.859	0.075
2450957.39	12.370	0.075	11.960	0.075	11.739	0.075	11.905	0.075
2450958.36	12.329	0.075	11.986	0.075	11.809	0.075	11.988	0.075
2450958.38	12.423	0.016	11.962	0.019	11.777	0.020	11.912	0.033
2450959.40	12.470	0.075	11.989	0.075	11.858	0.075	12.055	0.075
2450963.66	12.817	0.026	12.298	0.012	12.249	0.021	12.287	0.030
2450964.39	12.880	0.075	12.298	0.075	12.261	0.075	12.327	0.075
2450965.66	12.920	0.035	12.419	0.016	12.350	0.024	12.352	0.025
2450966.38	13.104	0.075	12.448	0.075	12.398	0.075	12.398	0.075
2450968.38	13.352	0.032	12.558	0.019	12.414	0.025	12.332	0.026
2450968.72	13.367	0.027	12.609	0.012	12.481	0.016	12.309	0.018
2450969.34	13.381	0.075	12.644	0.075	12.419	0.075	...	...
2450969.42	13.498	0.036	12.616	0.020	12.431	0.024	12.284	0.025
2450969.70	13.480	0.031	12.650	0.014	12.480	0.015	12.275	0.020
2450970.34	13.487	0.075	12.719	0.075	12.443	0.075	...	...
2450971.33	13.607	0.075	12.784	0.075	12.444	0.075	...	...
2450972.35	13.717	0.075	12.834	0.075	12.452	0.075	...	...
2450972.68	13.821	0.028	12.791	0.012	12.489	0.017	12.200	0.018
2450973.33	13.782	0.075	12.888	0.075	12.465	0.075	...	...
2450974.33	13.912	0.075	12.958	0.075	12.472	0.075	...	...
2450976.39	14.218	0.075	12.955	0.075	12.494	0.075	12.096	0.075
2450977.45	14.316	0.076	13.035	0.019	12.532	0.024	12.102	0.025
2450978.39	14.461	0.074	13.055	0.018	12.563	0.024	12.077	0.027
2450981.34	14.649	0.075	13.246	0.075	...	....	12.101	0.075
2450983.39	14.867	0.075	13.461	0.075	12.804	0.075	12.184	0.075
2450985.35	14.885	0.075	...	...	...	...	12.473	0.075
2450985.40	15.039	0.050	13.530	0.018	12.899	0.025	12.403	0.025
2450986.34	14.928	0.075	...	...	...	...	12.473	0.075
2450990.34	15.135	0.075	...	...	...	...	...	...
2450997.40	15.286	0.068	13.990	0.019	13.578	0.020	13.141	0.026
24501000.40	15.372	0.070	14.097	0.021	13.677	0.025	13.292	0.028

the radioactive decay extrapolation of the light curve.

Subsequent images over the next months showed the source maintained a constant magnitude. At the same time, the spectra featured a bluer continuum with superimposed broad absorption and emission features, which resembled photospheric epoch spectra. After the analysis on the light echo spectrum of SN 1991T (Schmidt et al., 1994), similar processes were considered for SN 1998bu. Early spectra of SN 1998bu from Hernandez et al. (2000) weighted with the integrated luminosity around each observation was compared to the light echo spectrum at 670d and showed similar features. The spectrum was corrected for reddening and co-added to create a synthetic spectrum at 670d (Cappellaro et al., 2001). The agreement between the synthetic and observed spectra strengthened the argument of a light echo as the emission source (Figure 4.2).

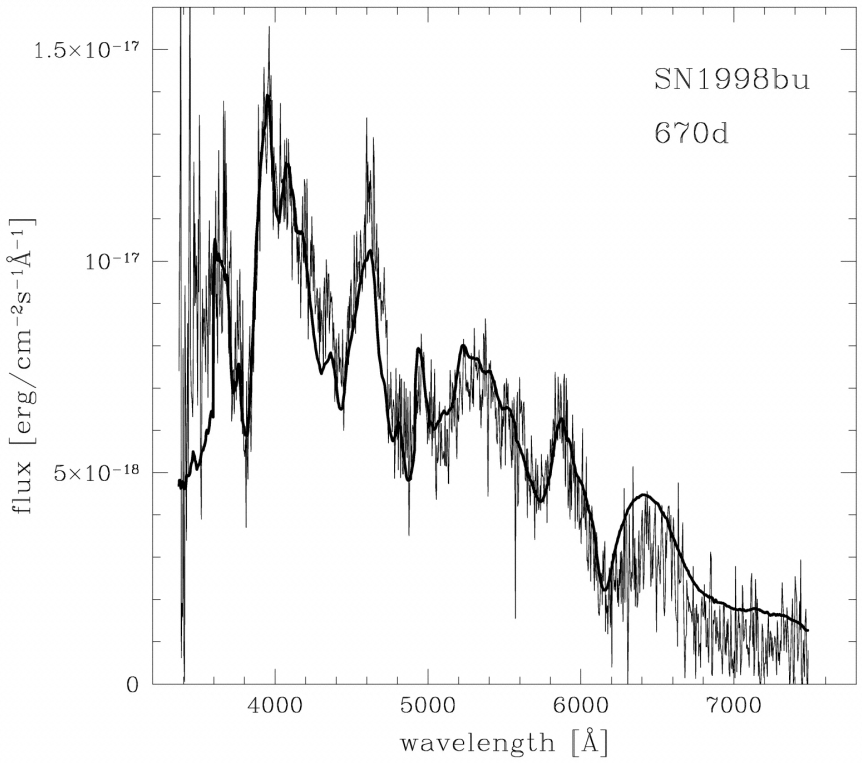

Figure 4.2: The late-epoch spectrum of SN 1998bu taken at 670d (thin line) compared with the time-integrated maximum light spectrum (Cappellaro et al., 2001).

Garnavich et al. (2001) presented further analysis of the light echo(s) of SN 1998bu. Images obtained with the *Hubble Space Telescope* Wide Field Planetary Camera 2 (WFPC2) on 2000 June 19 (762d past maximum) showed the existence of two echoes. The inner echo was shifted $0''.04$

from the center of the outer echo, suggesting an inclined dust sheet not uniformly distributed. The dust sheet that created the inner echo was determined to be <10pc from the SN and could be associated with the progenitor of SN 1998bu. Further discussion of these observations can be found in Section 4.4.

4.2.1 HST Archival Images

SN 1998bu and M96 were frequently imaged with *HST*, and we discovered several epochs of suitable light echo observations in the *HST* MAST archive for analysis. We chose four epochs for our investigation into the evolution of the echoes of SN 1998bu: 2003, 2006, 2009, and 2014. The first two epochs use the ACS (plate scale of $0''.027$ pix^{-1}) on *HST*, and the last two epochs were obtained with WFC3 (plate scale of $0''.04$ pix^{-1}). A complete list of the observations used in our analysis are in Table 4.5.

Table 4.5: HST SN 1998bu Observations

Filter	Filter Description	Date	Instrument	Exposure (s)
POL0UV, F435W	0° UV polarized Johnson *B*	2003-04-23	ACS	1708
POL60UV, F435W	60° UV polarized Johnson *B*	2003-04-23	ACS	1708
POL120UV, F435W	120° UV polarized Johnson *B*	2003-04-23	ACS	1708
F625W, CLEAR2S	SDSS *r*	2003-04-23	ACS	720
POL0UV, F435W	0° UV polarized Johnson *B*	2006-01-16	ACS	2000
POL60UV, F435W	60° UV polarized Johnson *B*	2006-01-16	ACS	2000
POL120UV, F435W	120° UV polarized Johnson *B*	2006-01-16	ACS	2000
F606W, CLEAR2S	broad *V*	2006-01-16	ACS	1600
F475W	SDSS *g*	2009-11-13	WFC3	500
F606W	broad *V*	2009-11-12	WFC3	2010
F336W	Strömgren *u*	2014-04-05	WFC3	1110
F438W	WPFC2 wide *V*	2014-04-05	WFC3	956
F555W	wide *V*	2014-04-05	WFC3	1134

In 2003, images of SN 1998bu were taken as part of *HST* Program 9299; P.I. H. Ford. The proposal, entitled "Geometric Measurement of Galaxy Distances," investigated the use of polarization measurements of SN light echoes to determine the distance of the host galaxies. SN 1991T and SN 1998bu were both imaged as part of this program, but no publications have been reported. 1708s of observation were obtained in the 0°, 60°, and 120° UV polarized F435W (Johnson *B*) filters, and 720s of exposure were obtained in the F625W (SDSS *r*) filter with a CLEAR2S aperture. An 1800s exposure image in the F250W (near UV broadband) filter with a CLEAR1S aperture was

rejected for our analysis. The observations are shown in Figure 4.5. Both of the echoes seem to be centered on the SN position, with the outer echo showing a mostly complete ring with brighter top left quadrant. The inner echo only shows the bottom portion of an arclet, and there are possible stellar artifacts located immediately adjacent to the echo.

The 2006 images of SN 1998bu were taken as part of *HST* Program 10607; P.I. B. Sugerman, entitled "Probing Circumstellar and Interstellar Dust with Scattered-Light Echoes." Again, SN 1991T and SN 1998bu, as well as Type-II SNe light echoes, were observed to put constraints on the dust around the SNe. SN 1998bu was chosen for this study because it exhibited a CSM echo (Garnavich et al., 2001). UV polarizers were also used in this program to estimate galaxy distances. 2000s of observation were obtained with the 0°, 60°, and 120° UV polarizers in the F435W filter, and 1600s were obtained in the F606W (broad V) filter with a CLEAR2S aperture. A 2000s exposure image in the F814W band with a CLEAR1S aperture was rejected due to a non-detection of the echo. The observations are shown in Figure 4.6. Visually, these echoes have grown since 2003, but are more disconnected. The bottom right part of the outer echo ring is very faint. The inner echo complete ring is visible, especially in the F606W image. However, in this epoch, the inner echo is shifted off center from the SN position. We discuss this shift in Subsection 4.4.1. A stellar artifact is featured in all four images, and the fact that the position of the feature does not change over the course of 3 years argues against it being part of the inner echo. The F606W and the 120° UV polarized F435W image seem to show a part of a secondary outer echo ring ($\theta = 0.71'' \pm 0.05$). These are the only images to show this phenomenon in the *HST* archival images. This angular size corresponds to a dust sheet of distance ∼280 pc in front of the SN.

As previously mentioned, SN 2006X and SN 1998bu were imaged with *HST* Proposal 11646; P.I. A. Crotts, investigating the environment of SNe Ia with the use of light echoes. 2010s of exposure in the F658N (N II), 2010s of exposure in the F606W (WPFC2 wide V), 500s of exposure in the F475W (SDSS g), and 350s of exposure in the F814W were acquired. Both the F658N and F814W images resulted in non-detections. A color composite of the images, including the location of the SN in relation to the host galaxy, is shown in Figure 4.3. The individual filter observations (including F814W) are shown in Figure 4.7. Again, these images feature a mostly complete outer echo ring, with a faint bottom right section. The inner echo still appears shifted off center, and the evolution of the inner echo arclet is apparent in these three years of images. In the bottom left corner, there seem to be more foreground artifacts in the outer echo that were previously not seen.

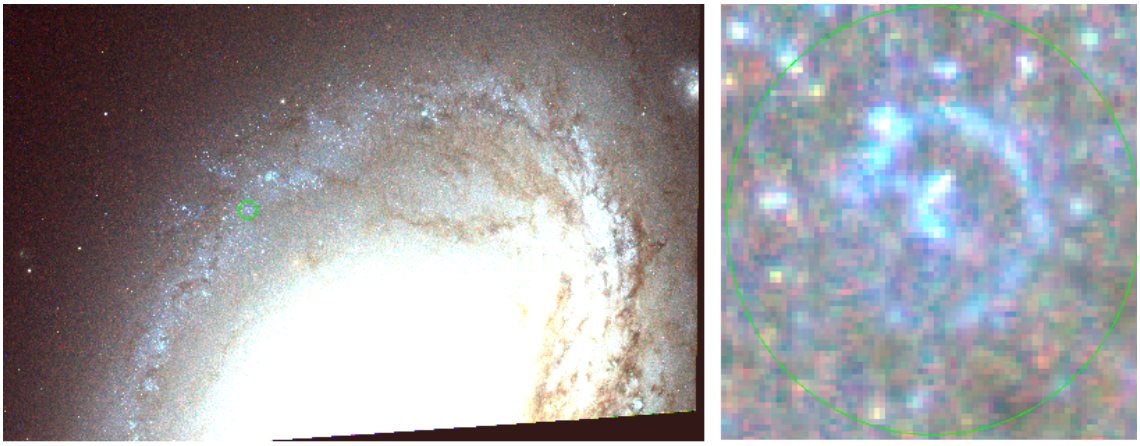

Figure 4.3: The color composite image of M96 from *HST* observations in 2009 (left panel) and 1.5″ x 1.5″ close up of the light echo (right panel) found at the SN location (green circle).

Lastly, M96 was imaged as part of *HST* Program 13364; P.I. D. Calzetti for LEGUS (Legacy ExtraGalactic UV Survey). Fortunately, the images of M96 included the location of the SN, and the light echoes were still visible, but clearly very faint. 2361s of exposure in F275W (UV wide), 1110s of exposure in F336W (Strömgren u), 956s of exposure in F438W (WFPC2 B), 1134s of exposure in F555W, and 980s of exposure in the F814W filter were obtained. The light echo was not detected in both the F275W and F814W filters. A color composite of the observations is shown in Figure 4.4, and images from the individual filters are shown in Figure 4.8. Again, the F814W filter was included in the figure for comparison. These echoes are the hardest to distinguish from the background, and the only bright spots are the artifacts located around the outer and inner ring. In these images, the outer ring is not azimuthally symmetric.

4.3 Photometry

Photometry of the 2003, 2006, 2009, and 2014 epochs of the echoes was determined using DAOPHOT in IRAF using the same procedure as discussed in Subsection 3.2.2. A coo.1 file, listing the location of the SN and any stellar artifacts that needed to be subtracted, was created. Due to the double structure of the echoes, several apertures were used. One summed the counts inside an area that encompassed both the outer and inner echoes. A different aperture was used to sum the counts of the interior echo. A larger than necessary aperture was used, and the stellar artifacts located right outside the inner echo were subtracted (see Figure 4.9). A small aperture (usually 2 pixels) was used

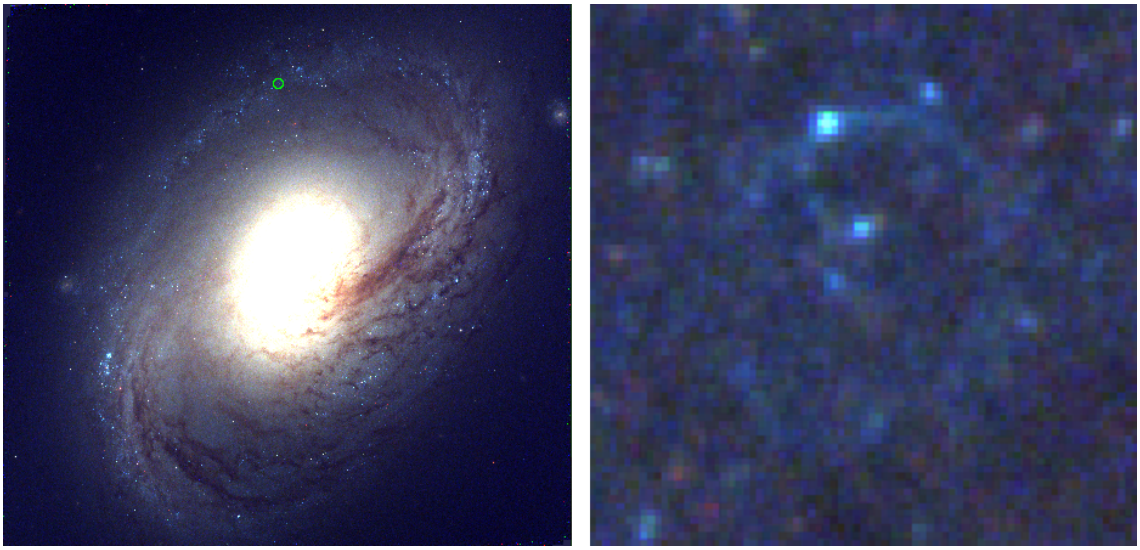

Figure 4.4: The color composite image of M96 from *HST* observations in 2014 (left panel) and 3.0″ x 3.0″ close up of the light echo (right panel). The green circle shows the SN location.

to determine the flux from the stellar artifacts to subtract from the total flux. The subtraction of the artifacts usually resulted in a change of 0.1 mag in the outer echo, but were considerably more problematic in the fainter inner echo. The VEGA zeropoints from the *HST* Instrument Handbook used for this analysis were 25.79 mag for F475W, 25.79 mag for F606W, 23.48 mag for F336W, 24.97 mag for F435W, and 25.82 mag for F555W.

Photometry was not performed on the polarized images from 2003 and 2006, as the polarization would affect the magnitude. Those images were used only for determinations of the angular size of the echo(s). Table 4.6 lists the photometry from the literature compared to our results. As is evident in the images themselves, the light echoes are growing fainter with time, which is as expected as more distant regions are being illuminated (Tylenda, 2004). Patat (2005) reports that the echo light curve will decline due to geometrical and forward scattering effects.

4.4 Dust Analysis

The angular size of the outer and inner echoes was determined by scaling the circular aperture in CIAO. For the outer echo, the circle was fit to the bright region of the ring, assuming symmetry. The varying illumination of the light echo rings suggests patchy areas of dust. The inner echo was more difficult to measure since only a partial ring is visible, which suggests that

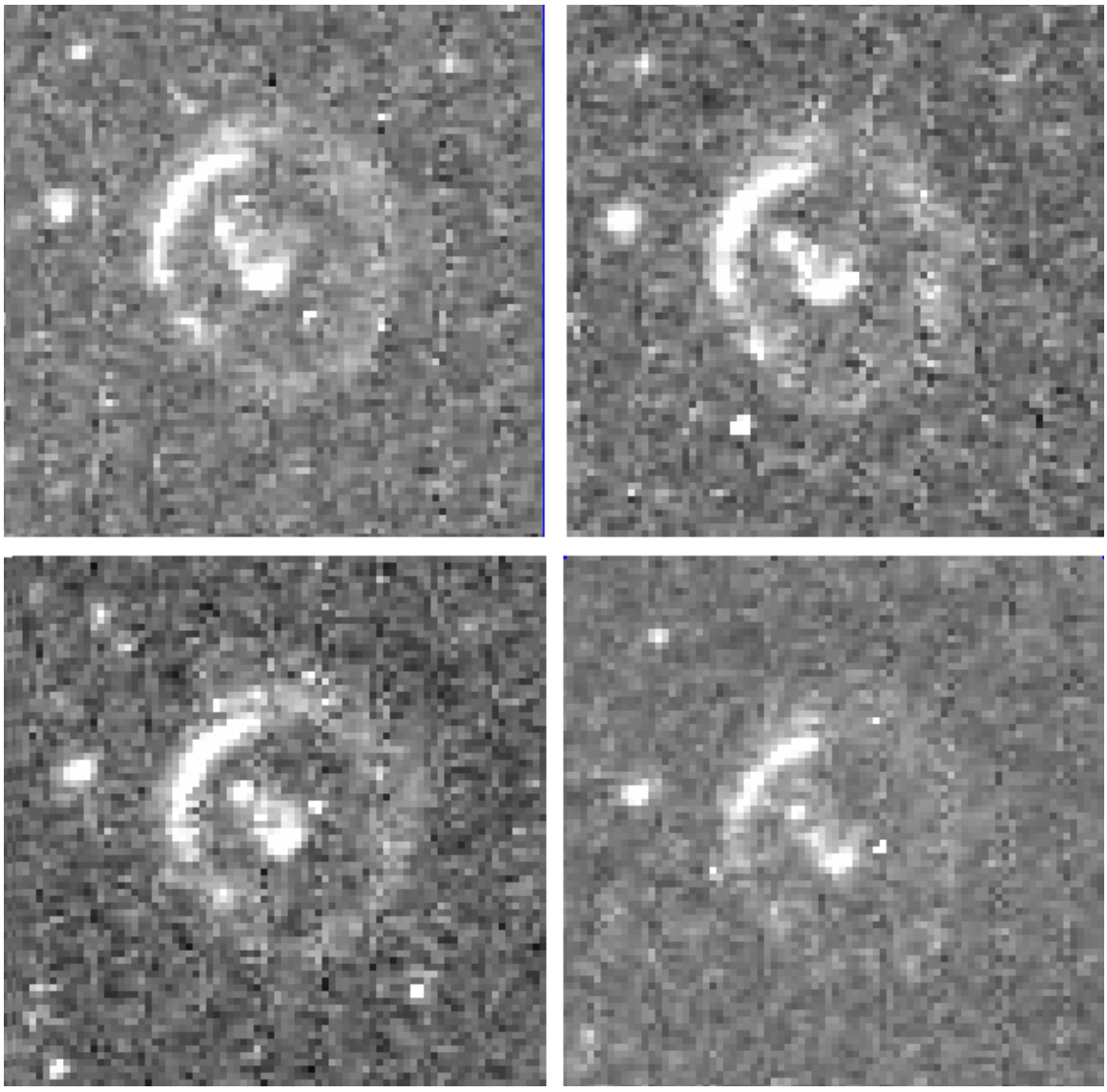

Figure 4.5: The 2.0″ x 2.0″ region of the light echo(s) of SN 1998bu in 2003. Upper left panel is the 0° UV polarized F435W band image, upper right panel is the 60° UV polarized F435W band image, bottom left is the 120° UV polarized F435W filter image, and bottom right panel is the F625W image.

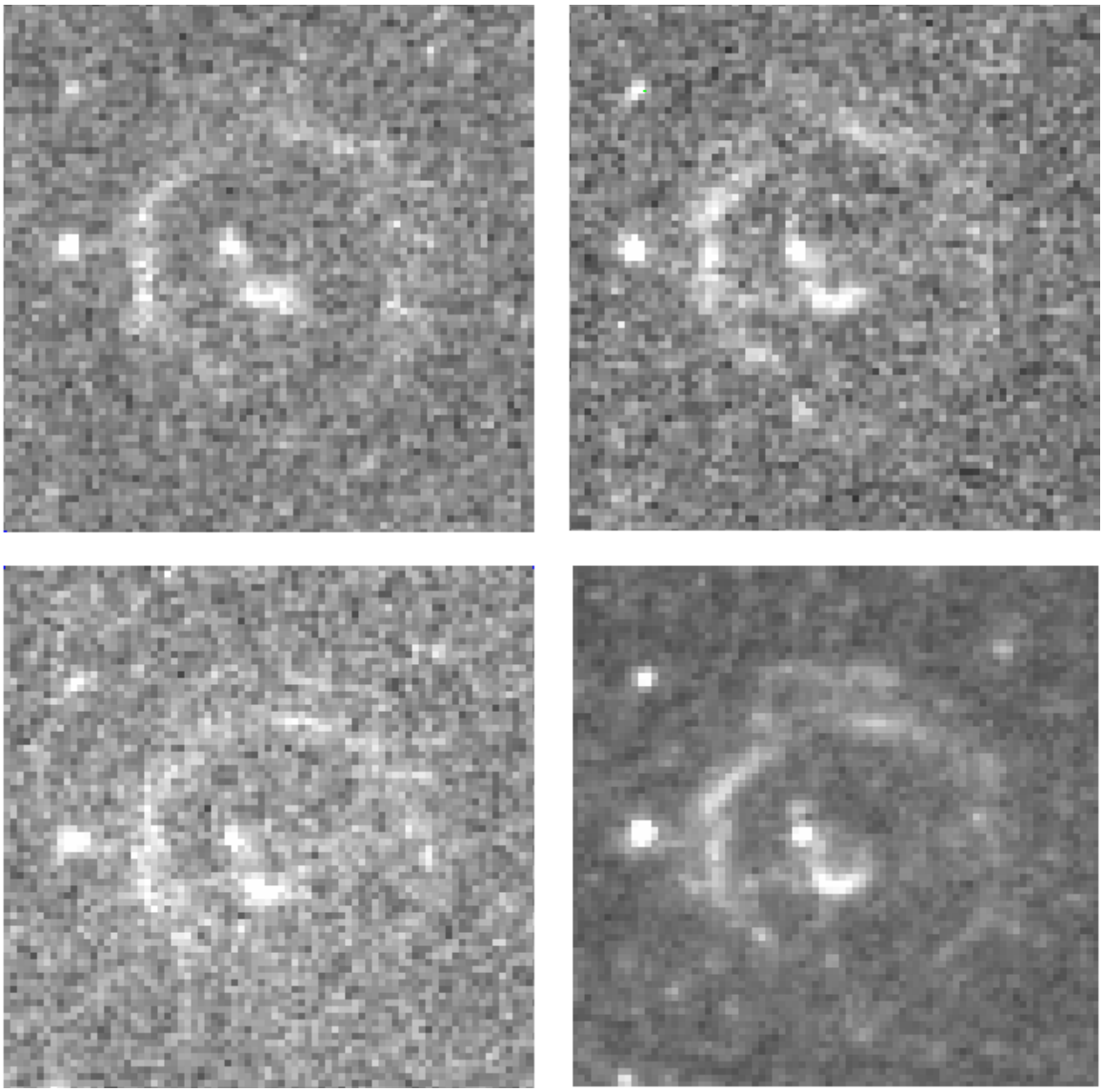

Figure 4.6: The 2.0″ x 2.0″ region of the light echo(s) of SN 1998bu in 2006. Upper left panel is the 0° UV polarized F435W band image, upper right panel is the 60° UV polarized F435W band image, bottom left is the 120° UV polarized F435W filter image, and bottom right panel is the F606W image.

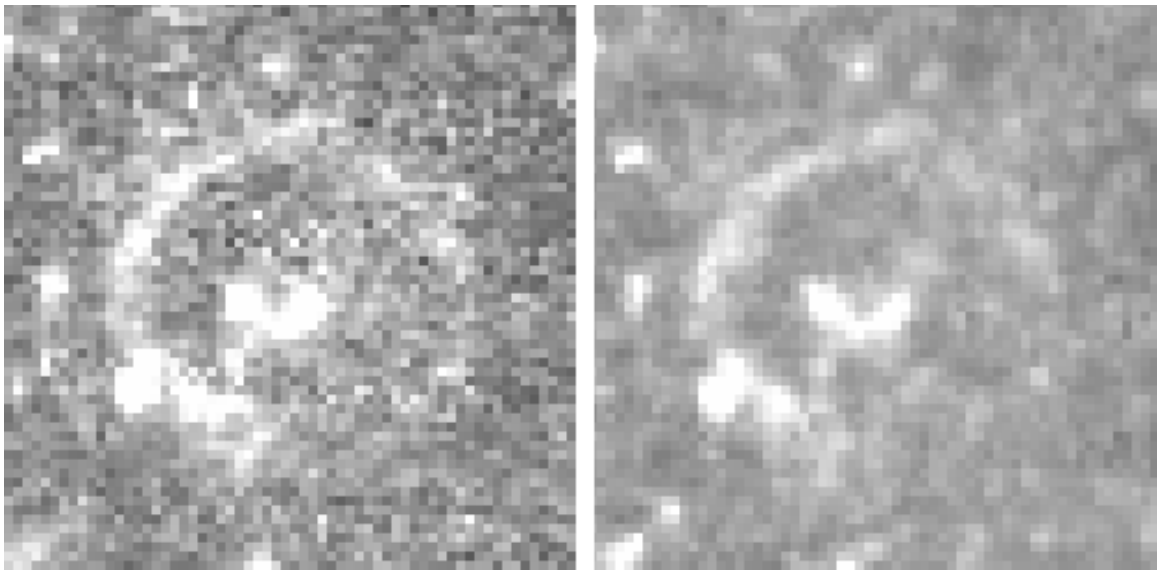

Figure 4.7: 2.5″ x 2.5″ region of the light echo(s) of SN 1998bu in 2009. On the left is the F475W band image, and the F606W observation is on the right.

Table 4.6: SN 1998bu Light Echo Photometry

Filter	Epoch (days past maximum)	m_{OE} (mag)	m_{IE} (mag)	m_{Tot} (mag)	Δm (mag)
V	500	...	...	20.8 ± 0.1	8.92
F555W	762	...	...	21.4	9.52
F625W	2010	22.1 ± 0.3	23.5 ± 0.4	21.9 ± 0.3	10.20
F606W	2800	21.9 ± 0.4	23.9 ± 0.5	21.7 ± 0.3	9.82
F475W	4200	21.9 ± 0.2	23.4 ± 0.3	21.6 ± 0.2	9.38
F606W	4200	21.9 ± 0.3	23.6 ± 0.3	21.7 ± 0.2	9.82
F336W	5800	21.3 ± 0.3	23.2 ± 0.4	20.9 ± 0.3	8.99
F438W	5800	22.3 ± 0.3	23.6 ± 0.4	21.9 ± 0.2	9.68
F555W	5800	22.2 ± 0.2	23.6 ± 0.3	21.7 ± 0.2	9.82

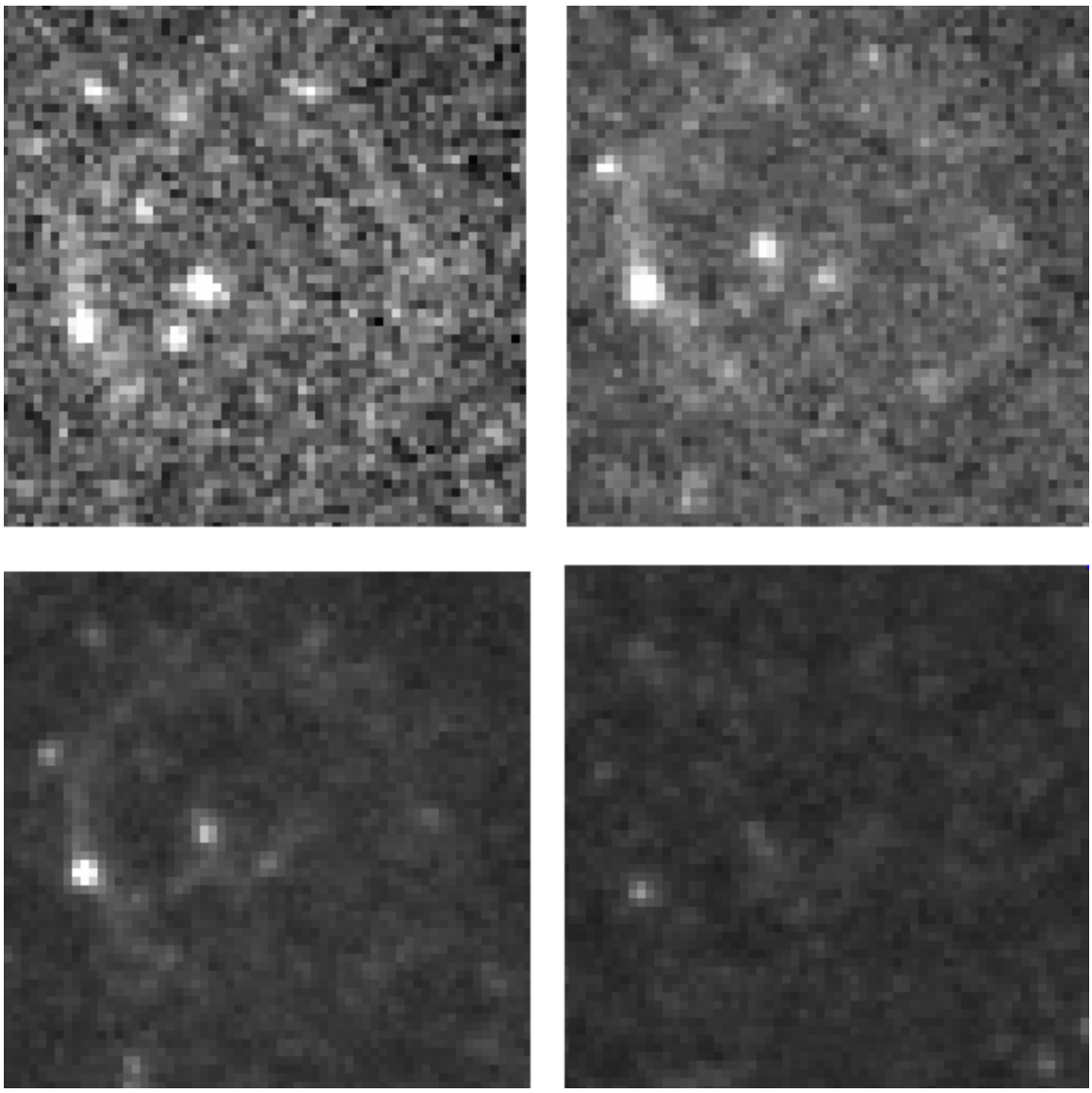

Figure 4.8: 2.5″ x 2.5″ region of the light echo(s) of SN 1998bu in 2014. Upper left panel is the F336W band image, upper right panel is the F438W band image, bottom left is the F555W filter image, and bottom right panel is the F814W image. The F814W image was not used in our analysis because of the low sensitivity and non-detection of the echo and was only included here for comparison purposes.

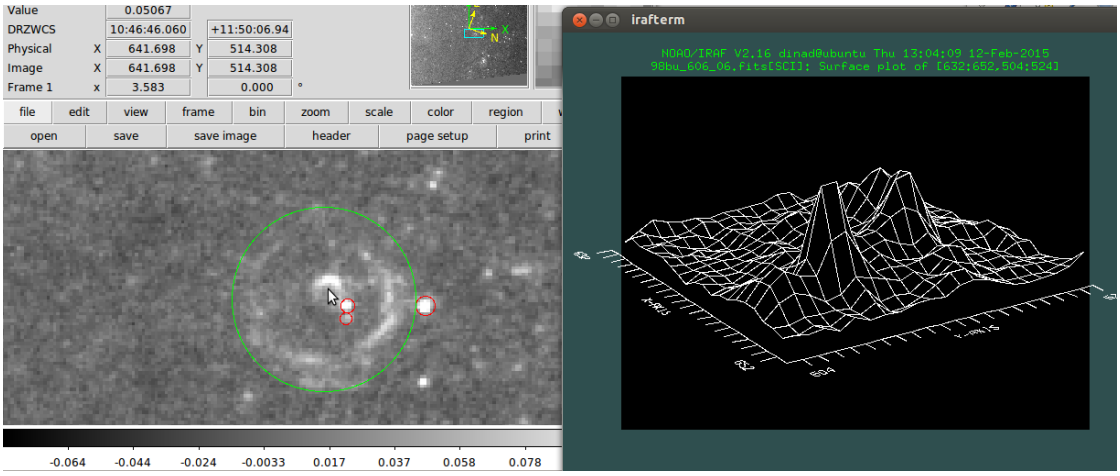

Figure 4.9: The surface plot of the SN 1998bu light echoes in the 2006 F606W observation shows the crowded field around the echoes. The flux of stellar sources (red) were subtracted from the flux of the circular aperture (green) when performing photometry.

only a partial dust sheet is intersecting the t paraboloid. Again, the circular aperture was fit to the arclet visible. The radius in pixels was converted to angular size (using the plate scale mentioned previously for each instrument). In the same convention as in the previous chapter, the θ^* column in Tables 4.7 and 4.8 refers to the PSF removed angular size. The t column shows the time since B maximum for the observations. The dust distances estimated from the angular size measurements in Garnavich et al. (2001) are reported in the first row of the tables.

Using the host galaxy distance to M96 of D = 10.5 Mpc, θ^*, and the t, the dust distances were estimated for the inner and outer echoes. Hernandez et al. (2000) lists the host galaxy distance as 11.2 $\pm$ 1.0 Mpc, which results in a $\sim$10% change in the dust distance. The average distance d between the SN and the dust for the outer echo is 190 $\pm$ 10 pc. The average distance d between the SN and the dust for the inner echo is 10 $\pm$ 3 pc. The dust distance estimate from Cappellaro et al. (2001) was $\sim$100pc for the outer echo. While the outer echo dust distances derived from our analysis are considerably larger than that reported in Garnavich et al. (2001), our inner echo values are consistent. The geometry of the echoes are shown in Figure 4.11, using the average distances derived from our analysis.

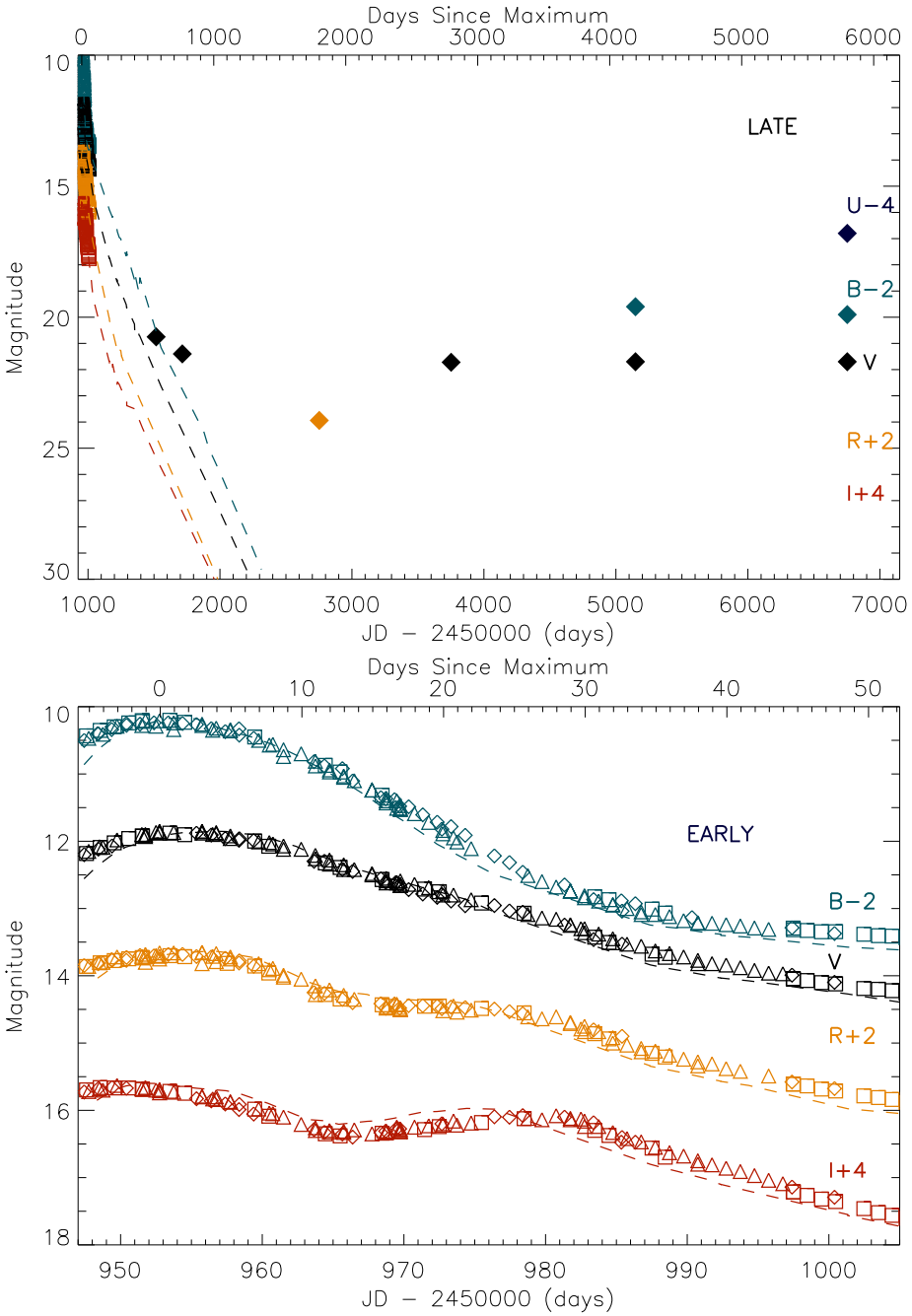

Figure 4.10: Early (lower panel)- and complete (upper panel) $BVRI$ light curves of SN 1998bu plotted over normal SN 1992A (dashed line) (Suntzeff, 1996). The early light curve only extends to ∼50 days past maximum, which is when monitoring of SN 1998bu ceased. All light echo data points are distinguished with filled diamonds, with the first two points from the literature (Cappellaro et al., 2001; Garnavich et al., 2001). Early SN 1998bu observations were taken from the literature: Hernandez et al. (2000) ($BVRI$-open diamonds), Jha et al. (1999) ($BVRI$-open triangles), and Suntzeff et al. (1999) ($BVRI$-open squares).

Table 4.7: SN 1998bu Outer Echo Sizes and Dust Distances

Filter	R(pix)	$\theta(''$)	$\theta(''$)*	t(yrs)	d(pc)
F555W	...	...	0.24 ± 0.01	2.09	120
POL0UV, F435W	19.5 ± 1.5	0.49 ± 0.04	0.46 ± 0.04	5.51	162
POL60UV, F435W	19.0 ± 1.0	0.48 ± 0.03	0.45 ± 0.03	5.51	155
POL120UV, F435W	18.9 ± 1.5	0.47 ± 0.04	0.44 ± 0.04	5.51	148
F625W, CLEAR2S	18.6 ± 1.0	0.47 ± 0.03	0.44 ± 0.03	5.51	148
POL0UV, F435W	23.5 ± 1.0	0.58 ± 0.03	0.55 ± 0.03	7.66	173
POL60UV, F435W	23.6 ± 1.5	0.59 ± 0.04	0.56 ± 0.04	7.66	173
POL120UV, F435W	23.4 ± 1.5	0.59 ± 0.04	0.56 ± 0.04	7.66	173
F606W, CLEAR2S	23.0 ± 2.0	0.58 ± 0.05	0.55 ± 0.05	7.66	166
F475W	20.8 ± 0.5	0.83 ± 0.02	0.78 ± 0.02	11.50	223
F606W	20.9 ± 0.5	0.83 ± 0.02	0.78 ± 0.02	11.50	223
F336W	24.5 ± 1.0	0.97 ± 0.04	0.93 ± 0.04	15.88	229
F438W	24.8 ± 1.0	0.98 ± 0.04	0.93 ± 0.04	15.88	229
F555W	24.5 ± 1.0	0.97 ± 0.04	0.92 ± 0.04	15.88	224

Table 4.8: SN 1998bu Inner Echo Sizes and Dust Distances

Filter	R(pix)	$\theta(''$)	$\theta(''$)*	t(yrs)	d(pc)
F555W	...	...	0.07 ± 0.01	2.09	10
POL0UV, F435W	5.21 ± 0.5	0.13 ± 0.01	0.10 ± 0.01	5.51	6.87
POL60UV, F435W	4.93 ± 0.4	0.12 ± 0.01	0.09 ± 0.01	5.51	5.40
POL120UV, F435W	5.02 ± 0.4	0.13 ± 0.01	0.10 ± 0.01	5.51	6.87
F625W, CLEAR2S	5.65 ± 0.5	0.14 ± 0.01	0.11 ± 0.01	5.51	8.49
POL0UV, F435W	7.17 ± 0.5	0.18 ± 0.01	0.15 ± 0.01	7.66	11.2
POL60UV, F435W	7.34 ± 0.4	0.18 ± 0.01	0.15 ± 0.01	7.66	11.2
POL120UV, F435W	7.31 ± 0.5	0.18 ± 0.01	0.15 ± 0.01	7.66	11.2
F606W, CLEAR2S	6.48 ± 0.4	0.16 ± 0.01	0.13 ± 0.01	7.66	8.14
F475W	6.10 ± 0.2	0.24 ± 0.01	0.19 ± 0.01	11.50	11.6
F606W	5.89 ± 0.2	0.24 ± 0.01	0.19 ± 0.01	11.50	11.6
F336W	6.63 ± 0.6	0.27 ± 0.02	0.23 ± 0.02	15.88	11.7
F438W	7.01 ± 0.5	0.28 ± 0.02	0.23 ± 0.02	15.88	11.7
F555W	6.98 ± 0.5	0.28 ± 0.02	0.23 ± 0.02	15.88	11.7

4.4.1 Inclined Dust Sheet

Following the discussion in Tylenda (2004), we measure the declination offset of the inner echo from the SN position in each image and average the results. Then, we calculate a from x_c/ct. Finally, we solve for the dust sheet inclination angle $\alpha = \tan a$. The results are shown in Figure 4.9. Again, the entries for the first row are taken from Garnavich et al. (2001) and are quite different from the values we derive. We do find the offset grows with time, but the values do have a larger uncertainty because of the lower brightness of the echoes at the later epochs. Since this is CSM dust which could be associated with the SN itself, the dust inclination could evolve with time as the dust expands outward.

Barberà et al. (2004) used Fourier analysis to deproject spiral galaxies, which included the host galaxy of SN 1998bu, M96, in their sample. They determined an inclination angle (the angle between the perpendicular to the plane of the galaxy and the line of sight) to be $50 \pm 1°$. Since this angle is nearly twice the dust sheet angle derived from our analysis, it is a further indication that the inner echo scattering material is associated with the SN and not the interstellar material.

Table 4.9: Dust Sheet Inclination Evolution

Epoch (yr)	Declination Offset ($''$)	Dust Sheet Inclination (°)
2.09	0.04	73
5.51	0.02 ± 0.01	31
7.66	0.03 ± 0.01	33
11.50	0.04 ± 0.02	30
15.88	0.05 ± 0.02	28

4.4.2 Echo Growth

Light echoes grow in time, if the dust is still intersecting the iso-delay surface, and the light echoes from SN 1998bu were captured in multiple epochs spanning over a decade. Thus, the evolution of the outer and inner echoes can be compared to the predicted growth in the dust sheet perpendicular to the line-of-sight approximation. Figure 4.12 plots the data versus the average distance between the SN and dust from our results. The first value is the Garnavich et al. (2001) measurement, while the four others are the average epoch measurements for the 2003, 2006, 2009, and 2014 observations we present.

The inner echo evolution is shown in Figure 4.13. The data is a good fit to the predicted

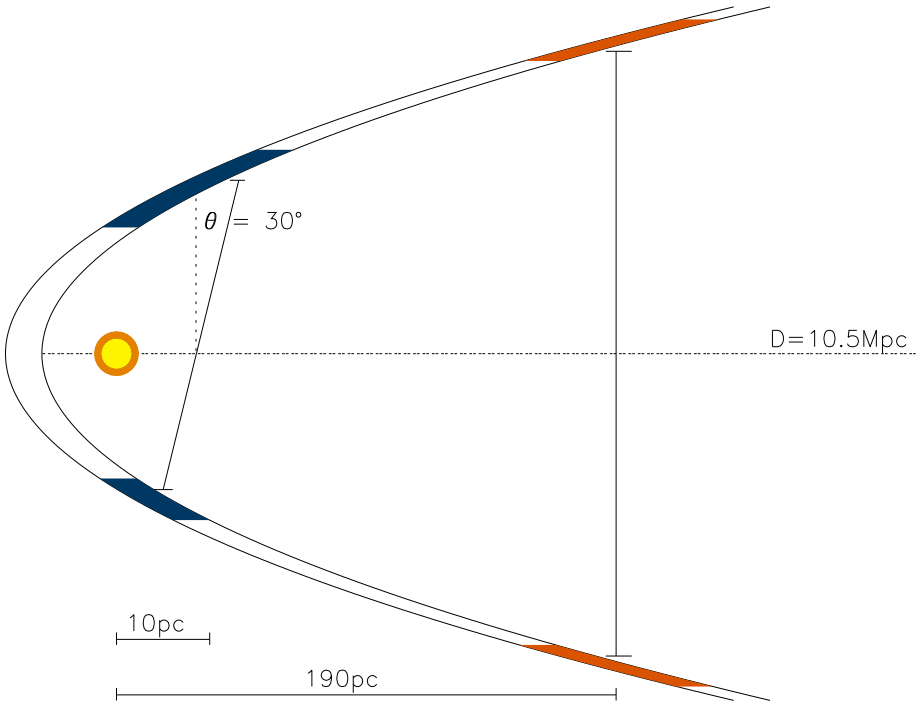

Figure 4.11: The geometry of the light echoes from SN 1998bu (not drawn to scale). The CSM inner echo (blue) is located 10pc in front of the SN, while the ISM outer echo (orange) is 190 pc away from the SN. The off-center shift of the inner echo ring, corresponds to a 30° decline of the dust sheet.

echo model based on the average dust distance derived from our data. The Garnavich et al. (2001) value is consistent with what has been derived from a decade of further observation of SN 1998bu.

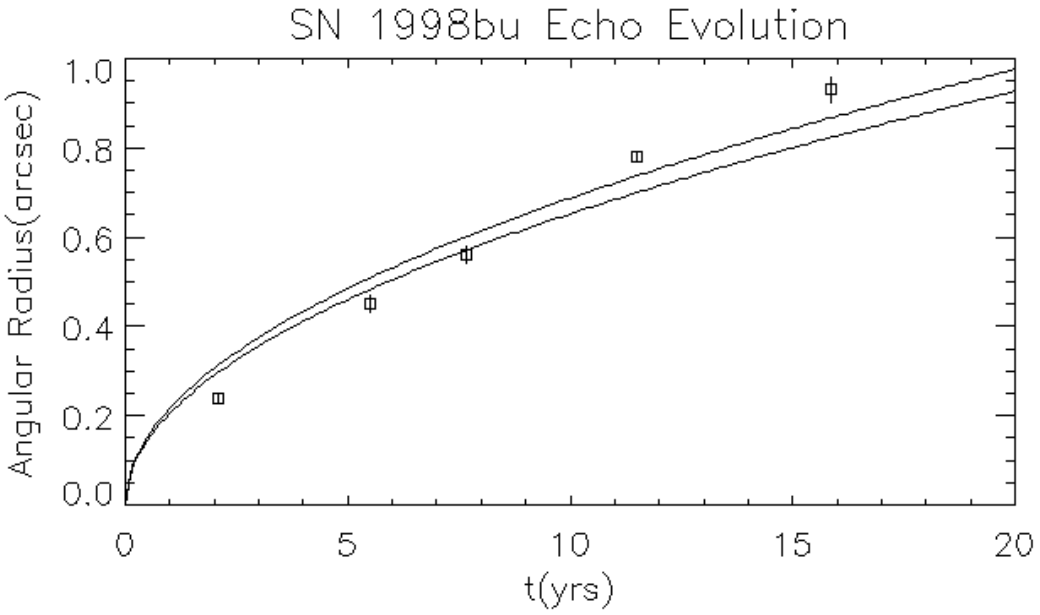

Figure 4.12: The angular size of the outer light echo from SN 1998bu is plotted versus time, spanning >15 years of observations. The models are the upper and lower limit to the average dust sheet distances derived from this research.

4.4.3 Optical Depth

The A_λ and peak magnitude information in Table 4.10 and Table 4.11 were reported from Suntzeff et al. (1999) and used to calculate the optical depth of the dust of the echoes from SN 1998bu. The A_B and A_V values are ∼0.2 mag different than reported in Jha et al. (1999), which resulted in a ∼0.02 change in the outer echo optical depth values (shown in Table 4.12).

4.4.4 Light Echo Color

We follow the same method for modeling the light echo color as in Subsection 3.4.2, using the filter throughputs from the ACS and WFC3 instrument handbooks. The peak spectrum was taken from the Weizmann Interactive Supernova data REPository (WISeREP) (Yaron and Gal-Yam, 2012). The spectrum, obtained by the Harvard Smithsonian team on the Fred Lawrence

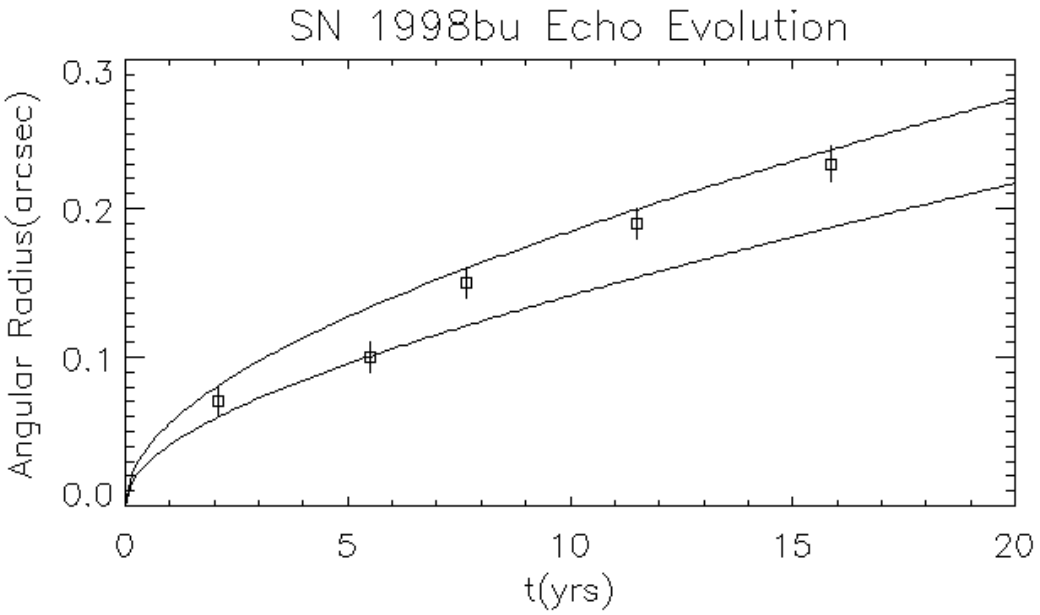

Figure 4.13: The inner light echo from SN 1998bu growth in time is consistent with the upper and lower limits derived from this research. The average dust sheet distance also matches the value estimated in Garnavich et al. (2001).

Table 4.10: Peak Photometry Magnitudes

Filter	JD_{Max} (day)	m (mag)
U	2450951.1 ± 0.5	11.91 ± 0.03
B	2450952.9 ± 0.5	12.20 ± 0.03
V	2450954.1 ± 0.5	11.88 ± 0.03
R	2450953.5 ± 0.5	11.70 ± 0.03
I	2450949.5 ± 1.0	11.67 ± 0.05

Table 4.11: Observed and Corrected Peak-Echo Magnitudes

	Inner Echo	Outer Echo		
Filter	Δm_{obs} (mag)	Δm_{obs} (mag)	A_λ	Δm_{corr}
U	11.29 ± 0.5	9.39 ± 0.5	1.80 ± 0.14	11.09 ± 0.5
B	11.28 ± 0.3	9.88 ± 0.3	1.50 ± 0.13	11.38 ± 0.3
V	11.82 ± 0.2	10.12 ± 0.2	1.14 ± 0.10	11.26 ± 0.2
R	11.80 ± 0.4	10.40 ± 0.5	0.92 ± 0.08	11.32 ± 0.5

Table 4.12: Optical Depth of Dust

Filter	τ_{OE}	τ_{IE}
F336W	0.08	3.3E-3
F438W	0.05	3.0E-3
F475W	0.07	3.7E-3
F555W	0.06	2.2E-3
F606W	0.07	2.0E-3
F625W	0.05	2.0E-3

Whipple Observatory 1.5m telescope using the FAST spectrograph on 1998 May 18 (one day before maximum) had a wavelength range of 3700 – 7540Å(Matheson et al., 2008). SN 1998bu was observed over a wavelength range of 3000 – 7200Å. We could not perform color analysis using F336W since no suitable peak spectrum of SN 1998bu covering wavelengths <3600Å was publicly available. The flash durations (Δt) used to scale the spectrum of SN 1998bu were estimated using the light curve and the log of observations from Jha et al. (1999). SN 1998bu was also a wider than normal SNe Ia, and the flash durations are as follows: 25.0 days (0.068 yr) in B, 34.7 days (0.095 yr) in V, and 39.7 days (0.109 yr) in R. The flash durations for SN 1998bu have a higher uncertainty due to fewer pre-maximum observations.

By comparing the colors of standard filters with the HST filters folded through the peak SN 1998bu and Vega spectrum, we determined the change in magnitudes between the filters for various dust types and scattering angles. Here, we use Bessell filters (Bessell, 1990) in all cases except the R filter, where we use a Cousins R standard filter (Cousins, 1974). The results are shown in Table 4.13. Figure 4.14 shows the normalized SN 1998bu spectrum with some of the WFC3 HST filter responses overplotted. The HST filters match the shape of the spectrum well, which is reflected in the small differences between the peak color predictions of the standard and HST filters as reported in Table 4.13.

In Table 4.14, we compare the ACS F606W – F625W echo color with our theoretical predictions using various dust cross-sections and scattering angles. All of the observed peak colors of SN 1998bu were taken from the literature (Suntzeff et al., 1999) and compared with the model predictions by folding the HST transmission filters into the peak SN 1998bu spectrum and comparing to the Vega spectrum. The peak F606W – F625W color matches the observed color within the uncertainty, and this is also reflected in the small magnitude difference between the V and F606W and

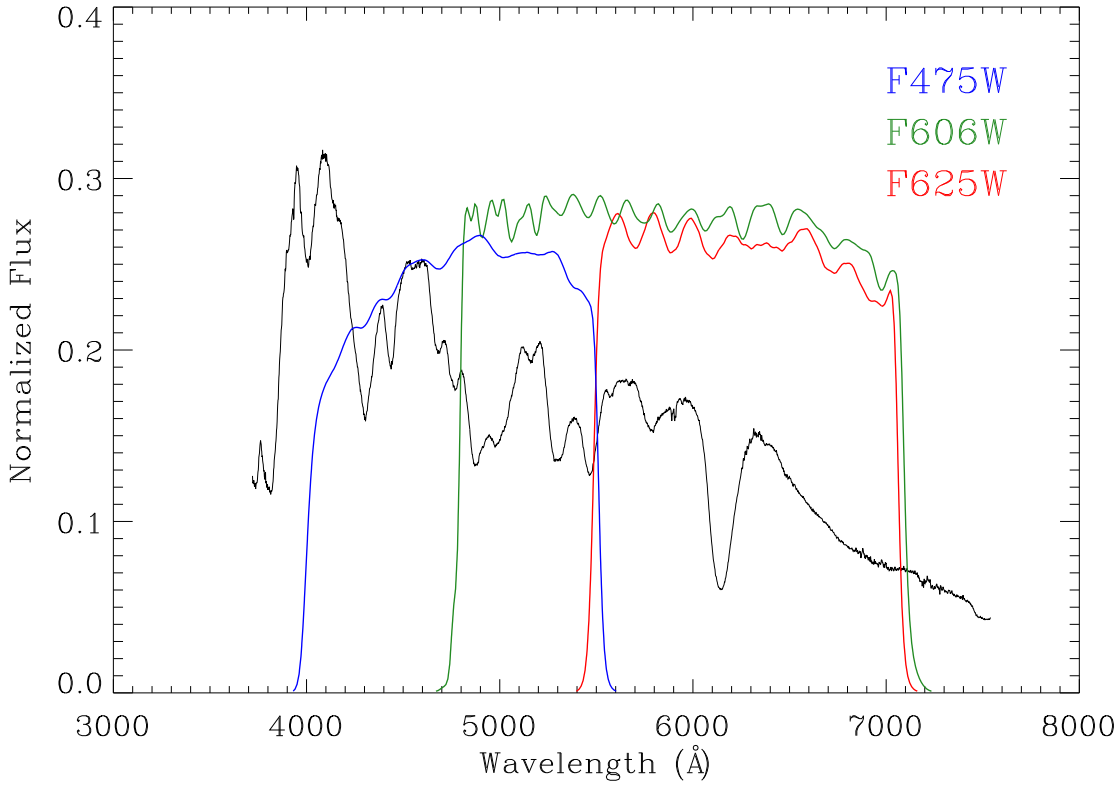

Figure 4.14: The normalized SN 1998bu spectrum (Matheson et al., 2008) is shown (black line) with the *HST* filter transmission curves (from the WFC3 instrument handbook) superimposed. The F475W (blue), F606W (green), and F625W (red) filter responses match the features in the SN Ia spectrum fairly well, which supports the output of the code, showing only minor differences between the *HST* and standard filters. These filters were chosen because they show the greatest change in magnitude between *HST* and standard filters.

R and F625W values shown in Table 4.13. Unfortunately, our high uncertainties in the magnitudes of the outer echo (OE) and inner echo (IE) prevent us from distinguishing between dust type and scattering angle.

Table 4.15 shows the 2009 WFC3 F475 – F606W color results. $(B-V)_{max} = 0.32 \pm 0.04$ mag, which is redder than a typical Type Ia supernovae. The color evolved to $(B-V)_{35d} = 1.48 \pm 0.04$ mag (Jha et al., 1999). The peak color is ∼0.1 mag different than that quoted from the literature and is most likely due to the difference between the standard and WFC3 filters. In this epoch, the error bars are smaller, and thus, we can make inferences about the dust type and scattering angle. The inner and outer echo colors seem most consistent with 0° scattering. Here, the outer and inner echo color matches closest with the color predicted by Milky Way-type dust.

Table 4.13: *HST* vs. Bessell Filters

Filter Names	Angle	Peak (mag)	R_V = 2.6 (mag)	R_V = 2.87 (mag)	R_V = 3.1 (mag)
B – F438W	0°	0.012	0.034	0.033	0.034
B – F438W	90°	0.012	0.022	0.024	0.019
B – F438W	180°	0.012	0.045	0.036	0.032
B – F475W	0°	0.045	-0.092	-0.111	-0.111
B – F475W	90°	0.045	-0.025	-0.050	-0.011
B – F475W	180°	0.045	-0.185	-0.138	-0.105
V – F555W	0°	-0.073	0.041	0.052	0.054
V – F555W	90°	-0.073	-0.024	-0.008	-0.038
V – F555W	180°	-0.073	0.092	0.048	0.015
V – F606W (HRC)	0°	0.028	-0.078	-0.076	-0.077
V – F606W (HRC)	90°	0.028	-0.017	-0.027	-0.005
V – F606W (HRC)	180°	0.028	-0.010	-0.015	0.009
V – F606W (WFC3)	0°	0.028	-0.080	-0.079	-0.081
V – F606W (WFC3)	90°	0.028	-0.018	-0.029	-0.006
V – F606W (WFC3)	180°	0.028	-0.017	-0.019	0.006
R – F625W	0°	0.065	0.094	0.094	0.095
R – F625W	90°	0.065	0.075	0.078	0.072
R – F625W	180°	0.065	0.083	0.080	0.073

Table 4.14: F606W – F625W Echo Color Predictions

	LMC R_V = 2.6 (mag)	SMC Bar R_V = 2.87 (mag)	MW R_V = 3.1 (mag)
Peak Color	Observed $V - R = 0.18 \pm 0.04$		Model F606W – F625W = 0.147
Light Echo Color	OE = -0.2 ± 0.5	IE = 0.4 ± 0.6	
0° Predictions	0.094	0.088	0.083
90° Predictions	0.216	0.195	0.240
180° Predictions	0.178	0.190	0.238

Table 4.15: F475W – F606W Echo Color Predictions

	LMC R_V = 2.6 (mag)	SMC Bar R_V = 2.87 (mag)	MW R_V = 3.1 (mag)
Peak Color	Observed $B - V = 0.32 \pm 0.04$		Model F475W – F606W = 0.246
Light Echo Color	OE = 0.0 ± 0.3	IE = -0.2 ± 0.5	
0° Predictions	0.164	0.133	0.126
90° Predictions	0.407	0.349	0.460
180° Predictions	0.100	0.206	0.323

Table 4.16 shows the 2014 F438W – F555W color results. Interestingly, the $B - V$ light echo color evolution has remained constant in the five years since the last observations. The peak color varies from the one reported in the literature, which is most likely due to differences between the standard and HST filters. 0° scattering matches the intrinsic light echo colors, but we cannot rule out backscattering, even though it is a much less probable scenario. All dust types are consistent with the inner light echo color due to the high uncertainties from the photometry.

Table 4.16: F438W – F555W Echo Color Predictions

	LMC $R_V = 2.6$ (mag)	SMC Bar $R_V = 2.87$ (mag)	MW $R_V = 3.1$ (mag)
Peak Color	Observed $B - V = 0.32 \pm 0.04$		Model F438W – F555W = 0.177
Light Echo Color	OE = 0.1 ± 0.3	IE = 0.0 ± 0.5	
0° Predictions	0.158	0.117	0.115
90° Predictions	0.352	0.293	0.397
180° Predictions	-0.022	0.098	0.193

A trend we notice at each epoch is that the outer and inner light echo colors are consistent with one another (within the error bars), which suggests the same dust mechanism for each (type and scattering scenario). This is very different from the results for the light echoes from SN 2007af. An $R_V = 3.1$ was assumed at peak (Jha et al., 1999), and our results are consistent with both light echoes being created from that same type of dust. We also conclude that 0° scattering is the most favorable scattering scenario since it matches our observed echo colors and is the most efficient method of light scattering.

The largest difference calculated between standard and HST filters is only ∼0.1 mag, which is the reason some authors choose to simply use their names interchangeably. We caution against this practice, since it only works well (based on our results) in the case of normal Type Ia supernovae. In the previous Chapter, we showed how this breaks down for unusual SNe, like the heavily reddened SN 2006X (see Subsection 3.4.2).

Chapter 5

SN 2009ig

In this chapter, we will discuss our early- and late-epoch observations of SN 2009ig and the light echo phenomenon first discovered in Large Binocular Telescope (LBT) images. We will also introduce the continued late-epoch monitoring of SN 2009ig with *HST*, but the bulk of the analysis of those images will continue after the completion of the dissertation.

SN 2009ig was discovered in SBa galaxy NGC 1015 (D = 39.1 Mpc) on 2009 August 20.48 by the Lick Observatory Supernova Search using the 0.76-m KAIT (Kleiser et al., 2009). The SN was located at $\alpha = 2^h38^m11^m.61$, δ = -11°18′45″.1. The spectra had strong absorption features, implying a high expansion velocity of 24,500 km s^{-1}, suggesting the Type Ia supernova was detected shortly after explosion (∼17 hours). Being an equatorial target, SN 2009ig was intensively studied by a variety of teams (see Figure 5.2).

5.1 Early Observations

Foley et al. (2012) reported 55 photometry epochs of SN 2009ig (Tables 5.1 and 5.2) taken with KAIT at Lick Observatory (Ganeshalingam et al., 2010). The observing campaign began 2009 August 21.5, two weeks before maximum. KAIT observed SN 2009ig with a nightly cadence to determine the rise time with great precision. The cadence was changed to every 3–4 days two weeks after peak light. The data were pipeline reduced using a KAIT automated process (Ganeshalingam et al., 2010). The images were bias- and flat-corrected. Host galaxy subtraction was performed with templates produced from images taken over a year past maximum. The local field of SN 2009ig

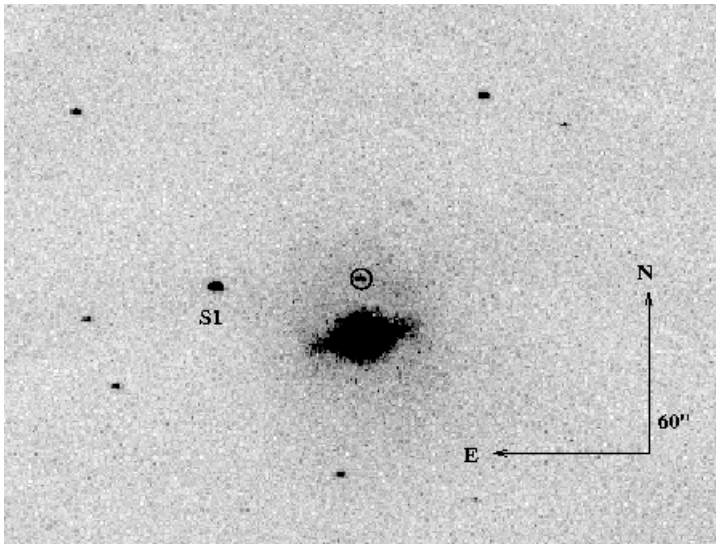

Figure 5.1: Discovery image of SN 2009ig in host galaxy NGC 1015 (Kleiser et al., 2009).

had very few local stars that could be measured reliably without saturation, which is the reason only one field star was used in calibrating SN 2009ig. This could result in photometric errors. The photometry package DAOPHOT in IRAF was used to determine the magnitudes by comparing the flux of the field star and the SN using a PSF fitting function. Instrumental magnitudes were calibrated using the Landolt (1992) system using the averages determined from 7 photometric nights (Ganeshalingam et al., 2010).

Target-of-opportunity observations taken by the *Swift* team began 2009 August 21.8 using the Ultraviolet/Optical Telescope (Table 5.3). Digital image subtraction was performed on all of the UVOT data using a template created from the last epoch observation for host galaxy subtraction. The UBV data were reduced using the method described in Milne et al. (2013).

SN 2009ig reached maximum B light on 2455080.54 ± 0.3 (2009 September 6.0) at 13.66 ± 0.03 mag Foley et al. (2012). It had a slower than normal SN Ia decline, and the MLCS2k2 fit to the light curve was consistent with a host galaxy extinction of $A_V = 0.01 \pm 0.01$ mag. This result is in conflict with the value we derive from Steward Observatory images, and is surprising in light of the light echo detection at late-epochs. The SN was found to be redder than template light curves and spectra. Peak magnitude information taken from Foley et al. (2012) can be found in Table 5.4.

Foley et al. (2012) reported on the high velocity features seen in the spectra of SN 2009ig. Two velocity components were found in the Si II (6355Å) feature. The higher feature corresponds

Table 5.1: SN 2009ig KAIT Observations

JD	B (mag)	err(B) (mag)	V (mag)	err(V) (mag)	R (mag)	err(R) (mag)	I (mag)	err(I) (mag)
2455065.01	17.304	0.039	16.865	0.033	16.957	0.034	16.889	0.092
2455065.96	16.519	0.036	16.216	0.035	16.309	0.029	16.346	0.038
2455068.02	15.115	0.036	15.151	0.028	15.117	0.035	15.273	0.037
2455069.00	14.748	0.036	14.790	0.031	14.858	0.034	14.892	0.037
2455070.00	14.614	0.037	14.546	0.029	14.592	0.029	14.652	0.037
2455071.94	14.120	0.037	14.199	0.072	14.220	0.032	14.232	0.043
2455072.96	13.972	0.037	14.042	0.028	14.137	0.029	14.146	0.037
2455073.99	13.847	0.036	13.937	0.035	14.057	0.031	14.103	0.037
2455074.94	13.825	0.036	13.851	0.028	13.986	0.029	14.059	0.037
2455076.02	13.738	0.036	13.672	0.031	13.855	0.029	13.935	0.038
2455077.00	13.609	0.036	13.623	0.028	...	...	13.870	0.038
2455077.93	13.643	0.036	13.592	0.029	13.779	0.029	13.918	0.037
2455079.89	13.629	0.036	13.537	0.028	13.692	0.029	13.880	0.037
2455081.01	13.583	0.036	13.451	0.028	13.637	0.029	13.875	0.037
2455081.92	13.622	0.036	13.494	0.030	13.695	0.029	13.940	0.37
2455082.94	13.669	0.039	13.555	0.028	13.708	0.029	13.939	0.037
2455083.94	13.595	0.036	13.487	0.039	13.663	0.034	13.942	0.039
2455084.99	13.765	0.036	13.586	0.029	13.749	0.029	14.032	0.040
2455085.93	13.769	0.037	13.602	0.028	13.782	0.029	14.080	0.037
2455087.94	13.861	0.037	13.629	0.028	13.941	0.029	14.179	0.038
2455089.97	...	...	13.651	0.029	13.900	0.029	14.295	0.037
2455090.92	13.989	0.036	13.768	0.028	14.006	0.029	14.337	0.038
2455091.92	14.047	0.046	13.739	0.044	13.965	0.041	14.311	0.038
2455092.96	14.123	0.038	13.815	0.034	14.125	0.029	14.438	0.037
2455093.99	14.359	0.039	...	...	14.258	0.032	14.618	0.037
2455094.87	14.416	0.037	14.055	0.028	14.334	0.029	14.625	0.037
2455095.95	14.537	0.036	14.115	0.028	14.394	0.029	14.615	0.037
2455097.02	14.639	0.038	14.085	0.030	14.345	0.029	14.606	0.037
2455097.90	14.776	0.038	14.238	0.028	14.460	0.029	14.663	0.037
2455098.93	14.885	0.036	14.203	0.028	14.482	0.029	14.621	0.037
2455099.94	15.000	0.036	14.301	0.029	14.470	0.029	14.601	0.037
2455100.93	15.113	0.042	...	...	14.444	0.031	14.515	0.037
2455101.98	15.145	0.037	14.330	0.028	14.476	0.029	14.461	0.040
2455102.96	15.175	0.036	14.335	0.028	14.425	0.029	14.435	0.037
2455104.96	15.381	0.036	14.413	0.028	14.403	0.029	14.394	0.037
2455106.87	15.591	0.039	14.524	0.029	14.425	0.029	14.434	0.037
2455112.91	16.076	0.044	14.825	0.028	14.666	0.030	...	...
2455114.90	16.112	0.037	14.928	0.038	14.781	0.029	14.430	0.037
2455116.96	16.206	0.091	15.104	0.029	14.916	0.029	14.544	0.037
2455120.93	16.288	0.036	15.292	0.028	15.066	0.031	14.754	0.037
2455123.89	16.480	0.039	15.388	0.028	15.337	0.029	15.049	0.037
2455126.91	16.418	0.036	15.448	0.043	15.363	0.030	15.169	0.037
2455129.81	16.514	0.036	15.636	0.029	15.532	0.029	15.325	0.037

Table 5.2: SN 2009ig KAIT Observations Continued

JD	B (mag)	err(B) (mag)	V (mag)	err(V) (mag)	R (mag)	err(R) (mag)	I (mag)	err(I) (mag)
2455132.86	16.619	0.047	15.721	0.031	15.572	0.029	15.442	0.038
2455133.85	16.546	0.040	15.704	0.029	15.544	0.034	15.509	0.037
2455139.91	16.716	0.063	15.941	0.044	15.809	0.088	15.880	0.061
2455143.81	17.001	0.148	16.088	0.043	15.935	0.031	15.973	0.047
2455148.89	16.792	0.044	16.081	0.038	16.074	0.029	16.063	0.037
2455154.82	16.974	0.037	16.316	0.029	16.326	0.029	16.397	0.038
2455159.77	16.983	0.036	16.376	0.029	16.402	0.029	16.490	0.040
2455168.81	17.187	0.045	16.682	0.033	...	...	16.820	0.038
2455173.83	17.295	0.037	16.745	0.030	16.835	0.030	16.981	0.040
2455182.76	17.286	0.036	16.994	0.030	17.066	0.041	17.385	0.127
2455188.71	17.527	0.036	17.095	0.033	17.263	0.031	17.509	0.069
2455196.79	17.589	0.061	...	...	...	...	...	...

Table 5.3: SN 2009ig Swift/UVOT Observations

JD	U (mag)	err(U) (mag)	B (mag)	err(B) (mag)	V (mag)	err(V) (mag)
2455065.33	17.896	0.068	17.079	0.040	16.546	0.052
2455066.58	16.712	0.042	16.113	0.032	15.827	0.042
2455068.58	15.163	0.021	14.961	0.025	14.926	0.031
2455070.50	14.257	0.015	14.403	0.024	14.411	0.028
2455072.96	13.741	0.011	14.048	0.022	14.010	0.024
2455075.13	13.504	0.011	13.776	0.022	13.816	0.024
2455076.58	13.498	0.012	13.714	0.023	13.697	0.025
2455079.33	13.517	0.012	13.613	0.022	13.561	0.024
2455081.00	13.702	0.006	13.666	0.022	13.568	0.024
2455084.42	13.827	0.012	13.720	0.022	13.602	0.024
2455086.75	13.994	0.012	13.842	0.022	13.654	0.024
2455088.92	14.264	0.005	...	...	...	...
2455089.50	14.289	0.015	14.002	0.023	13.748	0.025
2455098.96	15.385	0.024	14.845	0.025	14.273	0.028
2455105.96	...	...	15.483	0.028	14.515	0.029
2455107.88	...	...	15.626	0.030	14.631	0.030
2455113.79	...	...	16.015	0.030	14.925	0.031
2455116.88	...	...	16.188	0.033	15.199	0.034

Table 5.4: SN 2009ig Peak Values

Filter	U	B	V	R	I
Peak Light	2455076.57 ±0.08	2455080.54 ± 0.04	2455082.17 ±0.03	2455081.33 ±0.29	2455078.26± 0.25
Peak (mag)	13.46 ± 0.01	13.66 ± 0.03	13.52 ±0.02	13.64 ± 0.02	13.88 ± 0.03
Δm_{15}(mag)	0.95 ± 0.01	0.89 ± 0.02	0.58 ± 0.01	0.69 ± 0.01	0.63 ± 0.02

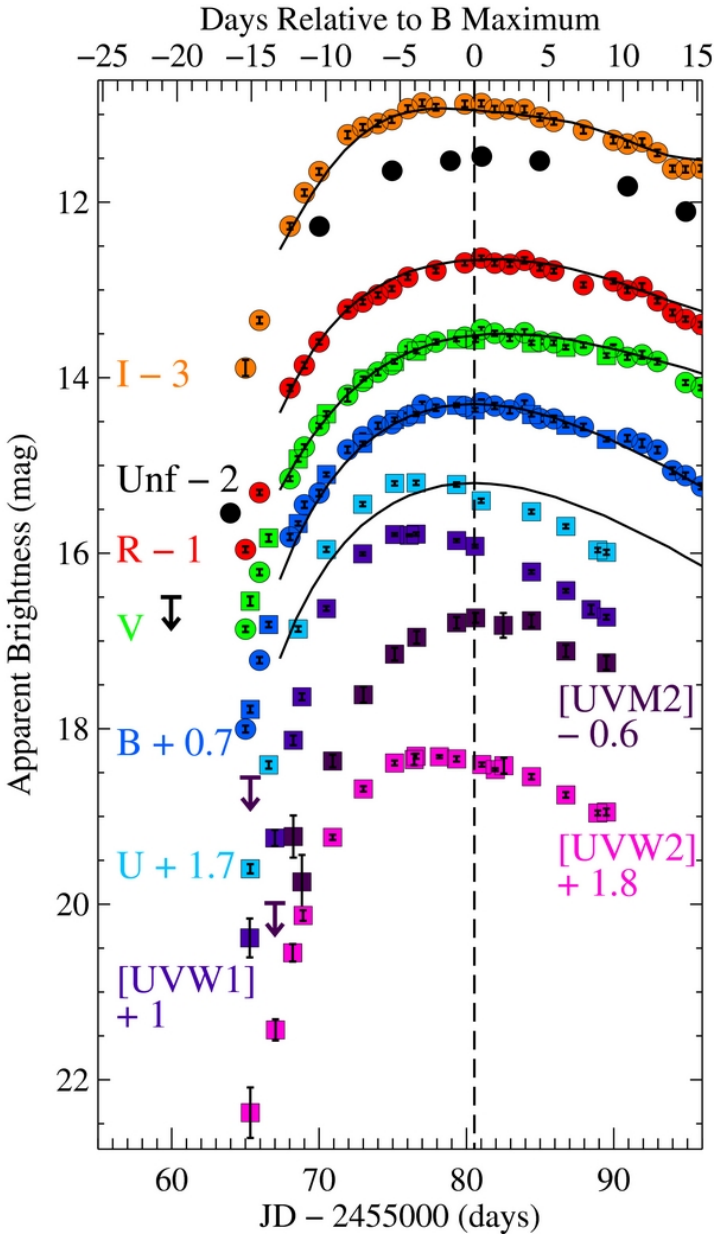

Figure 5.2: Light curves from Foley et al. (2012) showing $UVW2$ (fuchsia), $UVM2$ (purple), $UVW1$ (navy) $UBVRI$ (cyan, blue, green, red, and orange, respectively) superimposed on template SN 2005cf (black line) light curves (Wang et al., 2009). Circles are KAIT observations, and $Swift$/UVOT are distinguished by squares. Unfiltered observations are shown in black.

to the highest ejecta velocity value for a SN Ia. The strengths of the features change significantly from t = -13 days to t = -9 days (Figure 5.4). The figures show the change of the features over time. In the first spectrum, there seem to be two components, with the blue dominating. The spectra shift, with the t = -12.2 d have equal strengths. Then, in the t = -11.2 d, the redder component dominates. The blue component is barely distinguishable in the final spectra.

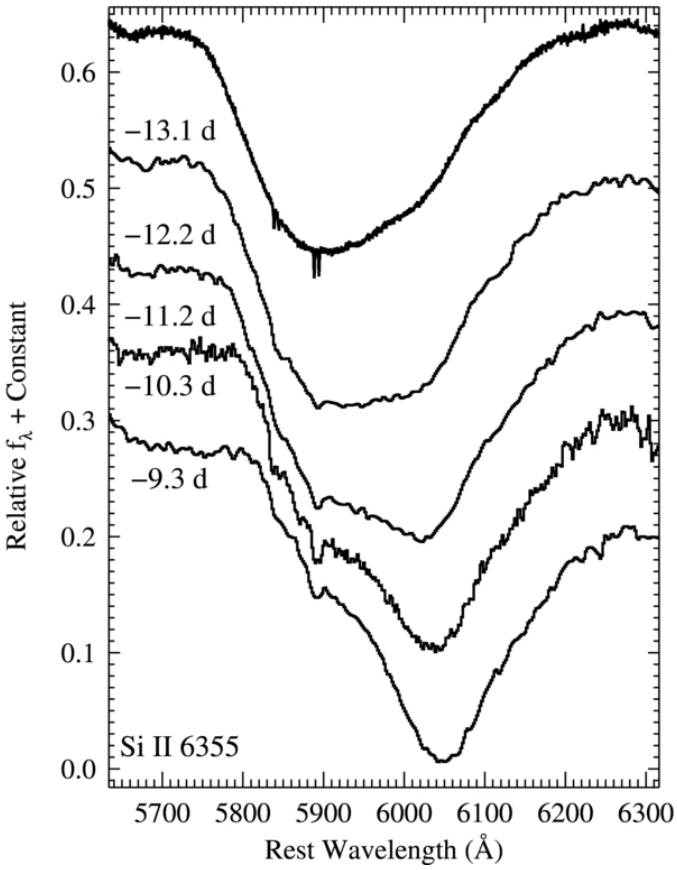

Figure 5.3: Spectra from Foley et al. (2012) showing the evolution of the high-velocity components of Si II at λ=6355Å.

Marion et al. (2013) continues the discussion of the spectral evolution of SN 2009ig to include spectra obtained at t = -14 d to t = +13 days. SN 2009ig had an unusually high number of lines with detectable high-velocity features (HVF), and these spectra observe the transition from HVF to photospheric-velocity features (PVF). HVF features could be created from the interaction between the SN ejecta and the surrounding medium (Gerardy et al., 2004). The shock from the SN explosion sweeps up CSM as it expands, leading to the formation of HVF features in the SN spectra. This

material could possibly cause the light echo discovered at late-epochs. Other theories include an enhancement in the abundance or changes in the ionization state of intermediate-mass elements in the outermost ejecta layers (Blondin et al., 2013; Mazzali et al., 2005; Tanaka et al., 2008).

5.2 Steward and Kitt Peak Observations

SN 2009ig was included in our late-epoch monitoring due to its slightly peculiar nature at peak, nearby host galaxy, and early detection. The SN was also located far-removed from the center of the host galaxy, making easy identification of SN detections. The telescope, instrument information, and reduction procedures for the Steward Observatory and Kitt Peak images can be found in Subsection 2.1.1. We add two late epochs of observations using MOSAIC on the Mayall-4m on January 11, 2011 and January 25, 2014 (>1500 days past maximum). The last epoch (light echo) required numerous stacked long exposures, which resulted in the high uncertainty shown in Table 5.5.

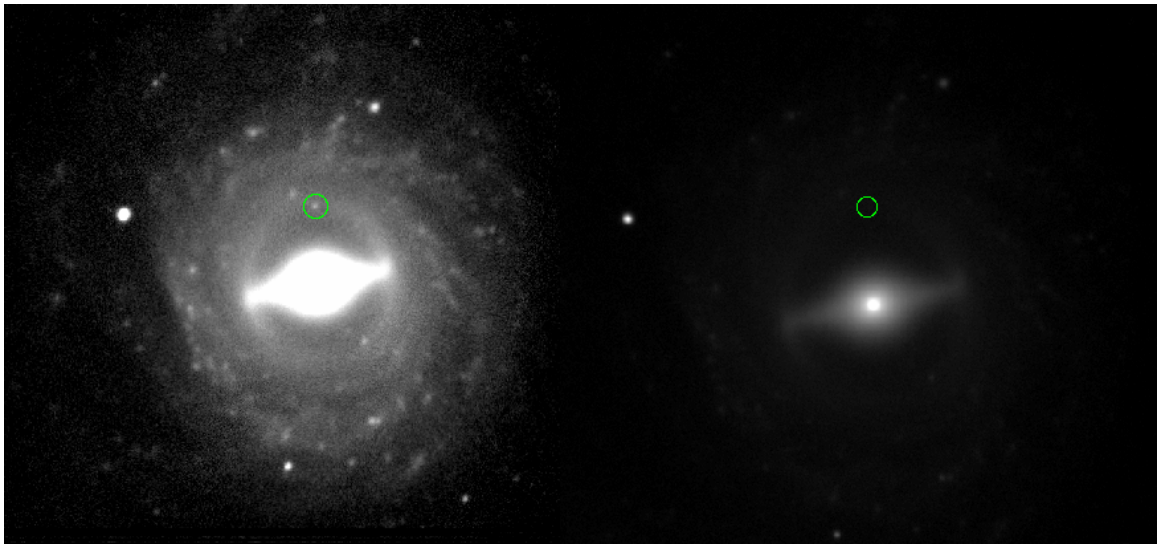

Figure 5.4: MOSAIC *B* observations of SN 2009ig on the Mayall-4m from January 2011 (left panel) and January 2014 (right panel). The green circle shows the SN position in NGC 1015, where the left panel shows the intrinsic SN emission before the light echo emerged. The images shows the comparison of the fields and seeing during these two epochs. The faintness of the echo at the late epoch is clear to see, which resulted in a large uncertainty in the magnitude.

5.3 Light Echo Observations

Late-time observations of SN 2009ig were obtained with the LBT using the Large Binocular Camera (Peter Garnavich, private communication), and the SN magnitudes are shown in Table 5.6. The first observation (∼390 days past maximum) was the result of three 60s exposures obtained through Bessell B and V filters. The second epoch at ∼750 days past maximum had five dithered 300s images. The same observing program obtained images at ∼800 and ∼850 days past maximum. A template of the bias levels was created from the overscanned sections in the images and subtracted. All data was flat corrected using twilight images and combined with a min-max rejection algorithm in IRAF.

As is the case of SN 2007af, NGC 1015 was imaged as part of a *HST* Cepheid variable observing program (Program ID 12880: P.I. A. Riess). NGC 1015 was selected as a new host galaxy target due to the location of SN 2009ig, which will then be used to measure the Hubble constant to ∼1.9% accuracy. The observing campaign used the same filters as SN 2007af (F160W: wide IR, F350LP: a white-light filter, F555W: wide V, and F814W: wide I) to collect the data at a rate 3 times faster (more frequent imaging) than that used for SN 2007af. The observing program ran from June 30, 2013 – October 8, 2013, obtaining images at 2 – 3 epochs per month. Due to the sheer volume of images from this campaign (Table 5.7), we are unable to present all of the data and analysis from the *HST* observations at this time, and we will simply discuss the preliminary results of the first epoch (see Figures 5.5 and 5.6).

Photometry of the *HST* images was performed using the same method as described in earlier chapters using the same VEGA magnitude zeropoints as mentioned for SN 2007af. In the *HST* field, we do have a local star that was previously calibrated with ground-based observations of standard stars at $\alpha = 2^h38^m8^s.377$, δ = -1°17′46″40. The location of the field star in the image poses many challenges since it is on the edge of the field. Thus, it was not imaged in each exposure that was then stacked. Therefore, it has a net exposure time that is less than the rest of the image. The star has magnitudes of $B = 19.513 \pm 0.004$ mag, $V = 17.960 \pm 0.002$ mag, $R = 16.641 \pm 0.003$ mag, and $I = 15.928 \pm 0.003$ mag, which agree well with the calibration from another team ($B = 19.55 \pm 0.05$ mag and $V = 18.10 \pm 0.05$ mag (Peter Garnavich, private communication).

The light curves of SN 2009ig are shown in Figure 5.7. Foley et al. (2012) (open circles), Steward Observatory (filled squares), Kitt Peak (filled triangles), *HST* (open squares) and light

Table 5.5: SN 2009ig Steward and Kitt Peak Observations

JD	B (mag)	err(B) (mag)	V (mag)	err(V) (mag)	R (mag)	err(R) (mag)	I (mag)	err(I) (mag)
2455251	18.503		18.209		18.575		18.974	
2455252	18.547		18.159		18.732		19.016	
2455400	20.639		20.362		20.662		...	...
2455439	21.279		20.649		20.949		20.600	
2455483	...	...	21.216		21.917		...	...
2455487	22.054		...	...	21.923		...	...
2455572.65	22.645	0.08	22.400	0.04	22.343	0.09	22.874	0.10
2456681.71	23.841	0.73	23.401	0.60	...	...	...	...

Table 5.6: SN 2009ig LBT Observations

JD	B (mag)	err(B) (mag)	V (mag)	err(V) (mag)
2455470.8	21.28	0.06	21.07	0.06
2455828.9	23.17	0.07	...	...
2455882.9	23.30	0.07	23.45	0.07
2455924.6	23.28	0.06	23.50	0.07

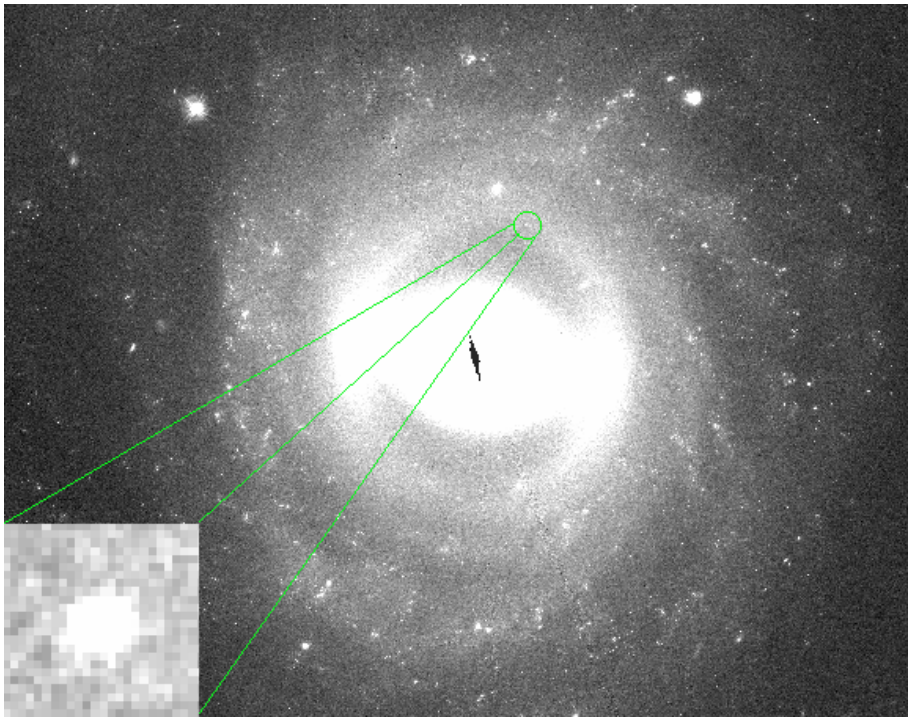

Figure 5.5: The full F555W image from June, 30, 2013. The light echo is distinguished with a green circle, and the 1″ x 1″ inset of the echo is shown at bottom left.

Table 5.7: SN 2009ig HST Observations

Date	Filter	Exptime (s)	Magnitude
2013-06-30	F350LP	2288	24.44 ± 0.12
2013-06-30	F160W	1306	...
2013-06-30	F555W	480	24.47 ± 0.02
2013-06-30	F814W	600	26.24 ± 0.29
2013-07-11	F350LP	2288	
2013-07-11	F160W	1306	
2013-07-11	F555W	480	
2013-07-11	F814W	600	
2013-07-20	F350LP	2288	
2013-07-20	F160W	1306	
2013-07-20	F555W	480	
2013-07-20	F814W	600	
2013-07-30	F350LP	2288	
2013-07-30	F160W	1306	
2013-07-30	F555W	480	
2013-07-30	F814W	600	
2013-08-08	F350LP	2288	
2013-08-08	F160W	1306	
2013-08-08	F555W	480	
2013-08-08	F814W	600	
2013-08-16	F350LP	2288	
2013-08-21	F350LP	2288	
2013-08-22	F160W	1306	
2013-08-21	F555W	480	
2013-08-21	F814W	600	
2013-08-31	F350LP	2288	
2013-08-31	F160W	1306	
2013-08-31	F555W	480	
2013-08-31	F814W	600	
2013-09-09	F350LP	2288	
2013-09-09	F160W	1306	
2013-09-09	F555W	480	
2013-09-09	F814W	600	
2013-09-16	F350LP	2288	
2013-09-16	F160W	1306	
2013-09-16	F555W	480	
2013-09-16	F814W	600	
2013-09-26	F350LP	2288	
2013-09-26	F160W	1306	
2013-09-26	F555W	480	
2013-09-26	F814W	600	
2013-10-08	F350LP	2288	
2013-10-08	F160W	1306	
2013-10-08	F555W	480	
2013-10-08	F814W	600	

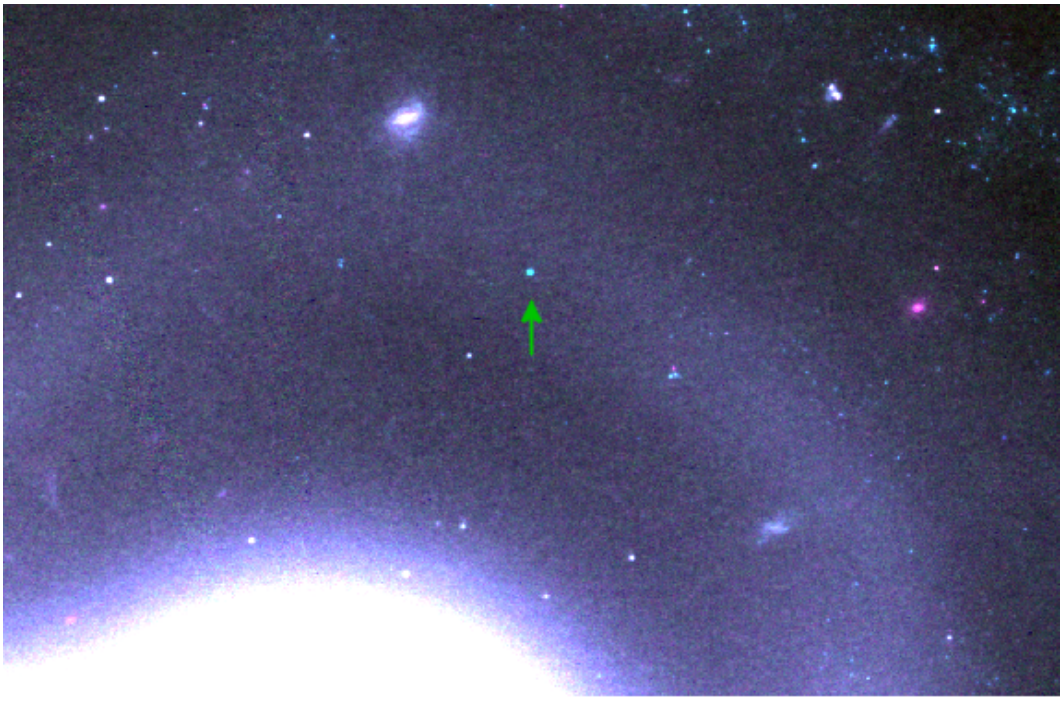

Figure 5.6: Color composite image created from WFC3 F350LP, F555W, and F814W observations from June 30, 2013. The green arrow points to the light echo, which appears bluer because of the faintness of the echo in the F814W (red) component of the color composite.

echo LBT images (Peter Garnavich, private communication) (filled circles) are plotted against SN 1992A (Suntzeff, 1996). It is clear, SN 2009ig is much broader at peak than SN 1992A and does not match the template well. At late-epochs, BV start to decline normally, while R is brighter at $\sim$500 days past maximum. The light echo observations show the clear deviation from the normal decline of a SN. We include the error bars in our very late-epoch Kitt Peak observations to show the general fading behavior of the echo.

5.4 Dust Analysis

In this section, we present the preliminary results of comparing the FWHM of local stars to that of the light echo. We also determine the angular size and thus, distance between the dust and the SN, and discuss the predicted versus observed light echo color for SN 2009ig based on our first epoch of HST observations.

5.4.1 Extended FWHM

Because the echo is located in an area free of artifacts, the same FWHM test as described in Subsection 2.2.1 was performed successfully. Comparing the light echo to the FWHM of local field stars in the F350LP and F555W filters resulted in a 2.4 times FWHM extended object. The FWHM of the echo in F814W was 2.0 times the FWHM of field stars (see Figure 5.8 for radial plot). This, combined with the unique dip feature of the surface plots of the images (Figure 5.9 for F555W) strengthens the argument of a light echo detection explanation of the source at the SN position.

5.4.2 Angular Size and Distance

As can be seen from the radial and surface plots, the angular size of the echo can be readily determined by fitting a region around the source. The radius of the echo is 4.19 $\pm$ 0.25 pixels in F350LP, 4.28 $\pm$ 0.20 pixels in F555W, and 3.45 $\pm$ 0.21 pixels in F814W. The echo is hardest to distinguish from the background in F814W, which is the same trend observed for SN 2007af. The PSF subtracted angular size of the echoes (using the WFC3 pixel scale of $0.04''\text{pix}^{-1}$) are 0.12 $\pm$ $0.02''$, 0.12 $\pm$ $0.01''$, and 0.09 $\pm$ $0.02''$, respectively. Adopting a host galaxy distance of 39.09 Mpc (Foley et al., 2012), and the time since B peak (3.81 yr), this translates to an average dust distance of 190 $\pm$ 40 pc. This is consistent with the dust distance derivations of <300 pc from the ground-

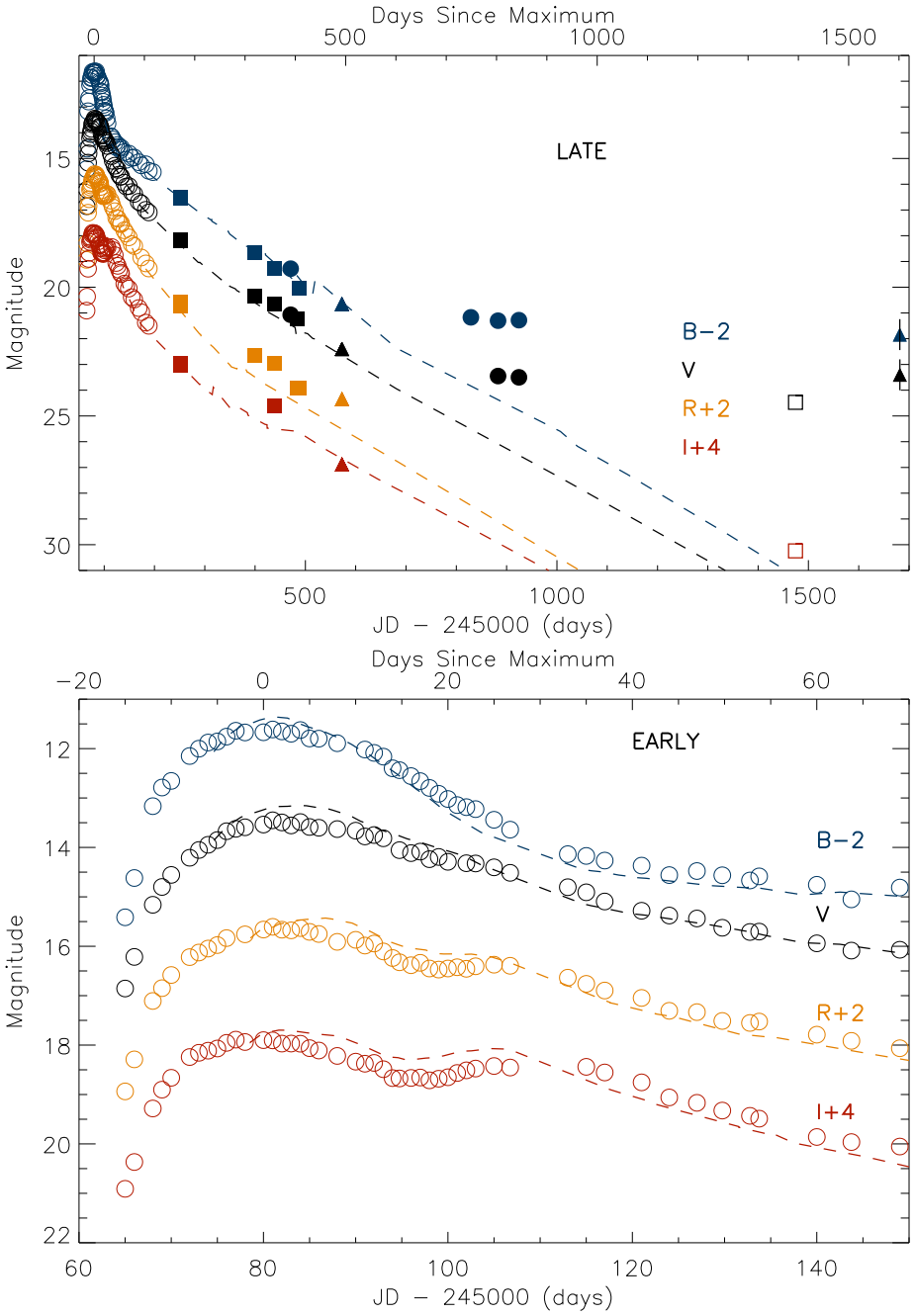

Figure 5.7: *BVRI* data (open circles) from Foley et al. (2012) are overplotted against the dashed template of SN 1992A (Suntzeff, 1996). *BVRI* filled squares and triangles are the Steward Observatory and 4-m additions, respectively, and the filled circles are the *BV* LBT observations (Peter Garnavich, private communication). As is clear from the fit of the template SN, SN 2009ig was a broad SN at peak. Open squares are the first epoch of the Cepheid campaign with *HST*.

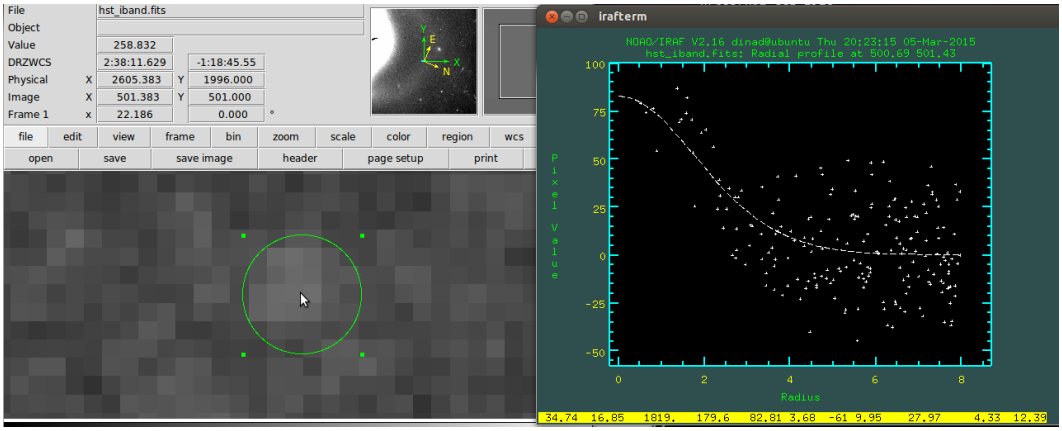

Figure 5.8: The IMEXAMINE radial plot of the F814W image of the echo of SN 2009ig from June 2013, showing the large scatter and faintness of the echo.

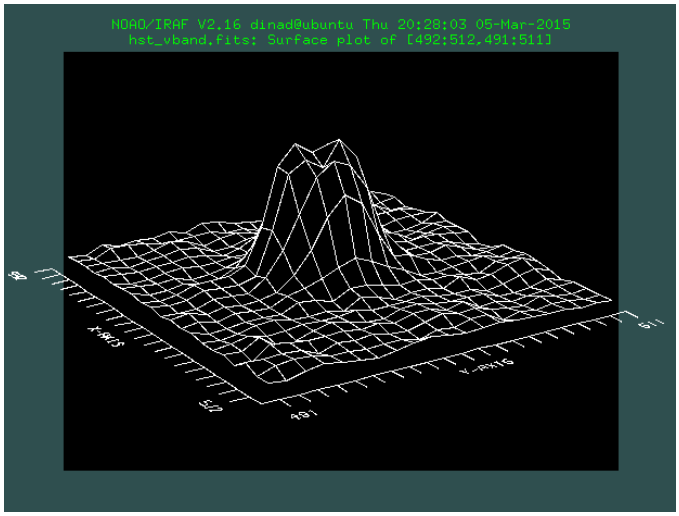

Figure 5.9: The IMEXAMINE surface plot of the June 2013 F555W filter observation. A dip in the peak is clearly visible adding strength to the light echo argument. Stars in the field feature a sharp peak with no dip in the middle.

based LBT images (Peter Garnavich, private communication). The schematic of the light echo (not drawn to scale) is shown in Figure 5.10.

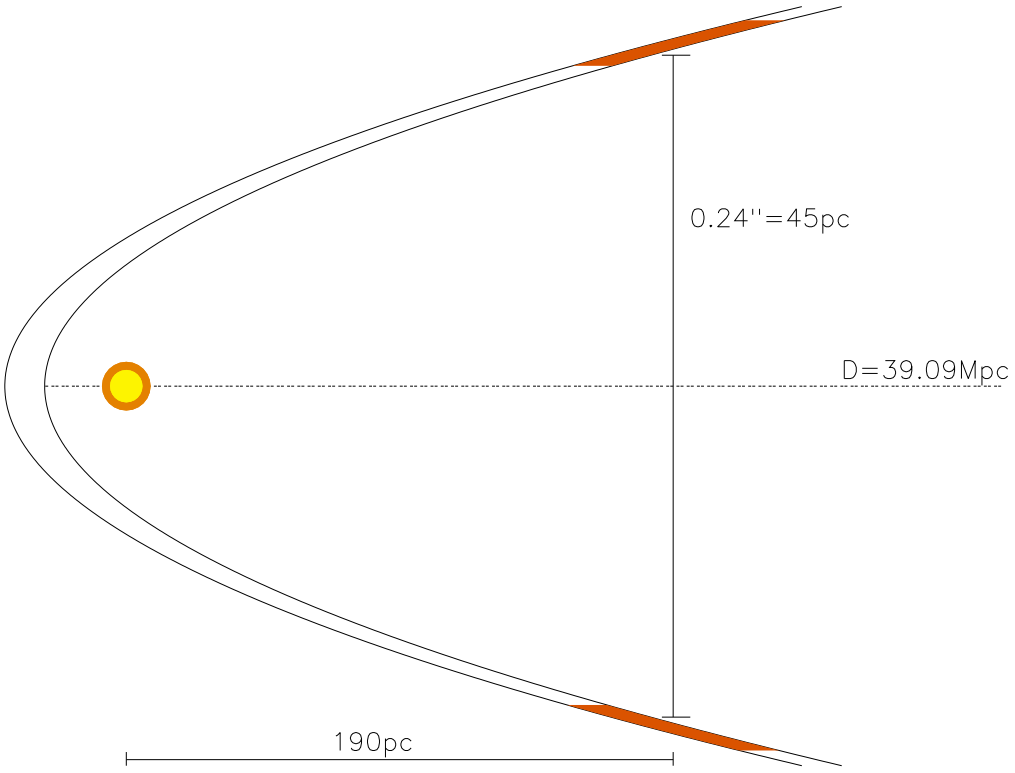

Figure 5.10: The geometry of the echo (not to scale) as derived from the June 30, 2013 *HST* observation. The echo (shown in orange) was created from a dust sheet located ∼190 pc in front of the SN.

5.4.3 Light Echo Color

We obtained a peak spectrum (-0.4d) of SN 2009ig from Foley et al. (2012), which covered a wavelength range of 4200 – 10000Å. Since the spectrum did not cover UV wavelengths, we only present the F555W – F814W color. A *Swift* spectrum is available at nearly the same epoch, but only covers a wavelength range of 2000 – 5000Å. The optical spectrum was obtained with 450s exposure on the Low Resolution Spectrograph on the Hobby-Eberly Telescope by S. Odewahn. We show the results of our dust color predictions in Table 5.8. The flash duration estimates from the light curve and observations of SN 2009ig from Foley et al. (2012) were 36.9 days (0.101 yr) for

V and 52.2 days (0.143 yr) for I. We show the normalized peak spectrum with the HST filters overplotted in Figure 5.11.

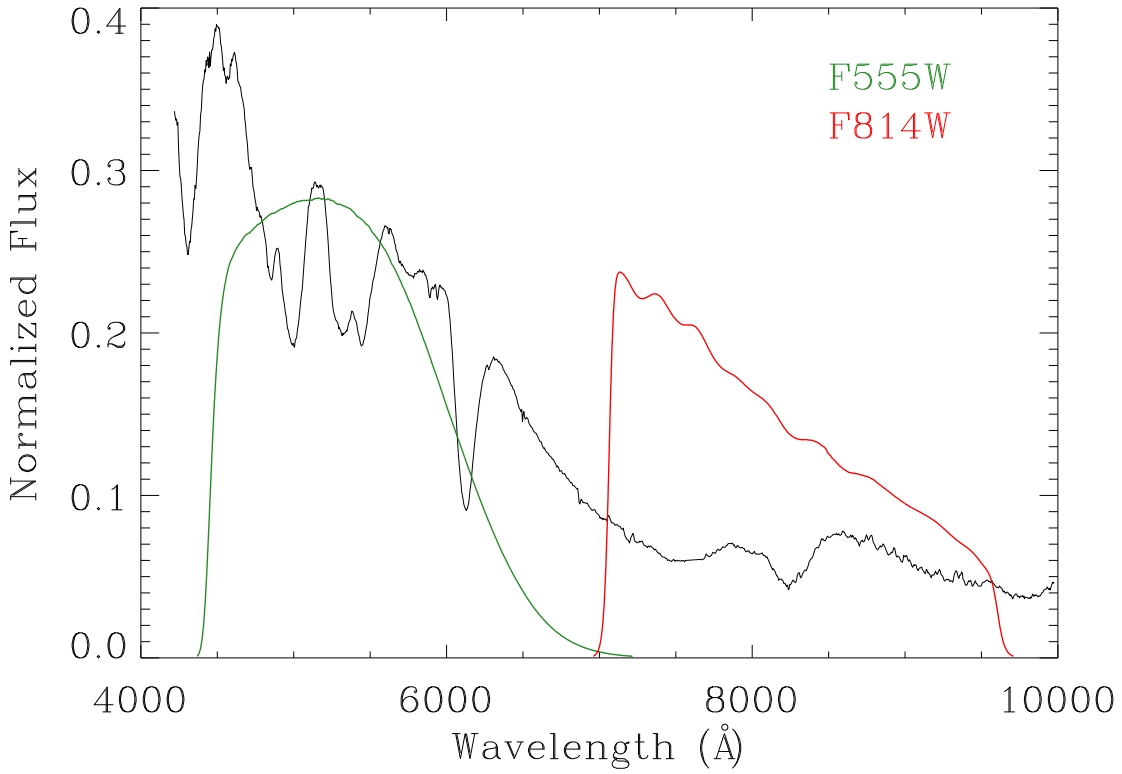

Figure 5.11: The normalized SN 2009ig spectrum (Foley et al., 2012) is shown (black line) with the HST filter transmission curves (from the WFC3 instrument handbook) superimposed. The F555W (green) and F814W (red) filter responses match the normal SN Ia spectrum fairly well, which supports the output of the code, showing only minor differences between the HST and standard filters.

It is readily apparent from even our one epoch of HST observations, that the F555W – 814W color is extremely blue (-1.77 ± 0.30 mag). This light echo exhibits a color that is even bluer than SN 2007af, which suggests a very unusual dust type. However, the spectrum of SN 2009ig did show large high velocity and photospheric absorption features, which could possibly account for some of the blueness seen in the echo color (Foley et al., 2012; Marion et al., 2013). Even in these redder wavelengths, the predicted color was a poor match to the observed peak and light echo color. However, from this analysis, we can rule out 90° and 180° scattering, but cannot discriminate between dust types.

Table 5.8: F555W – F814W Echo Color Predictions

	LMC R_V = 2.6 (mag)	SMC Bar R_V = 2.87 (mag)	MW R_V = 3.1 (mag)
Peak Color	Observed $V - I$ = -0.36 ± 0.02		Model F555W – F814W = -0.092
Light Echo Color		-1.77 ± 0.30	
0° Predictions	-0.883	-0.885	-0.881
90° Predictions	-0.138	-0.260	-0.075
180° Predictions	-0.285	-0.279	-0.023

By integrating the SN 2009ig spectrum folded with the *HST* transmission filters and Bessell filters compared to the Vega spectrum folded with the same filters and integrating over the wavelength range of the Bessell filters (4300 – 7500Å for V and 7000 – 9000Å for I), we can calculate the magnitude differences. We compare the differences between the *HST* and standard filters in Table 5.9. The largest differences amount to ∼0.1 mag in the V filter. Since the filter differences are relatively small (especially compared to the findings for SN 2006X), the color mismatch between the theoretical and observed predictions could be due to either abnormal dust or some other complex mechanism. We must also rerun the photometry of SN 2009ig using calibrations from more local stars to improve our photometry.

Table 5.9: *HST* vs. Bessell Filters

Filter Names	Scattering Angle	Peak (mag)	R_V = 2.6 (mag)	R_V = 2.87 (mag)	R_V = 3.1 (mag)
V – F555W	0°	-0.045	0.076	0.088	0.091
V – F555W	90°	-0.045	0.008	0.024	-0.007
V – F555W	180°	-0.045	0.131	0.083	0.048
I – F814W	0°	-0.047	0.026	0.023	0.021
I – F814W	90°	-0.047	-0.026	-0.020	-0.025
I – F814W	180°	-0.047	-0.036	-0.027	-0.038

Due to the large uncertainties in our ground-based light echo observations and *HST* archive pipeline reduction issues, we leave the completion of the analysis of the SN 2009ig light echo to future work, which we discuss in Section 7.1.

Chapter 6

Comparisons

The comparison of Type Ia supernova echoes is challenging due to the different time delays and dust geometries. First, we will consider similar cases. We begin by comparing SN 1991T and SN 1998bu. These were the first SN Ia light echo detections and have been rigorously studied together for their peak and echo similarities, and they both were monitored >1000 days past maximum. We continue this discussion with the addition of the new late-epoch observations. Next, we will compare SN 2007af to SN 1998bu, which is the only other clear case of a dual-feature light echo in a SN Ia, and the inner echo was also proposed of circumstellar dust origin (Garnavich et al., 2001). Unfortunately, SN 1998bu was not captured with the I filter, but we will outline the various parallels and differences between the echoes.

SN 2006X was observed in an I filter (F775W), but shows a different color dependence than SN 2007af, implying a different dust. The echo from SN 2006X showed a distinct wavelength dependence, with more light scattered from shorter wavelengths. W08 credits this trend to small dust size. This pattern is also observed in SN 2007af and SN 1998bu and can be explained with shorter wavelengths being more efficient scatterers. We will conclude with comparing and contrasting the small sample size of SN Ia light echo discoveries from the literature and from the late-time archival *Hubble Space Telescope* observations featured in this dissertation.

6.1 SN 1991T vs. SN 1998bu

At ∼600 days past maximum, the magnitude of SN 1991T plateaued due to the existence of a light echo (Sparks, 1994). SN 1991T was one of the first SNe Ia to be monitored to very late epochs (>1000 days) due to its nearby host galaxy NGC 4527 (D = 15 Mpc using Cepheid calibration) and strange behavior at peak (Sparks et al., 1999). SN 1991T was also the first SN Ia light echo detection, showing the success of monitoring peculiar SNe for light echo searches. The SN had a very slow decline rate of $\Delta m_{15}(B) = 0.94 \pm 0.05$ mag (Phillips et al., 1999), which is similar to the value derived for SN 1998bu of 1.01 ± 0.05 mag (Jha et al., 1999). The late-time observations from 750 – 950 days past maximum showed a rate of decline consistent with 0.01 ± 0.03 mag per 100 days. In spectra obtained using the Multiple Mirror Telescope spectrograph 752 days past maximum, the emission shifted blueward of 4500Å, which is typical of a light echo signature.

The light echo from SN 1998bu was found at a similar epoch (∼500 days past maximum), and the nebular spectrum obtained using the ESO 3.6-m telescope had also shifted to a blue continuum (Cappellaro et al., 2001). SN 1998bu featured a much higher optical depth than SN 1991T, which implies more material along the line of sight. Polarization measurements were obtained for both echoes, but the results were only published for SN 1991T. Figure 6.1 shows the spectral comparison of both SNe at two epochs. The spectra show remarkable similarity to each other. Figure 6.2 shows the V absolute magnitude light curve of both echoes. SN 1991T is slightly brighter at late-epochs (∼0.8 mag), but the same light echo signature is observed. The late-epoch echo magnitudes of SN 1991T are compared to our SN 1998bu combined echo magnitudes in Table 6.1. F342W is a comparable U filter to F336W. The SN 1991T values from Sparks et al. (1999) are shown in the first four rows, which are consistent with the values determined in our analysis for SN 1998bu.

Table 6.1: SN 1991T vs. SN 1998bu Light Echo Magnitudes

Date	Epoch (days since B_{peak})	Filter	Light Echo Magnitude
1996 Dec 07	2050	F606W	21.9
1996 Dec 22	2065	F342W	21.2
1997 Dec 28	2436	F342W	21.3
1998 May 10	2581	F342W	21.5
2006 Jan 16	2800	F606W	21.7 ± 0.1
2009 Nov 12	4200	F606W	21.7 ± 0.1
2014 Apr 05	4200	F336W	20.9 ± 0.3

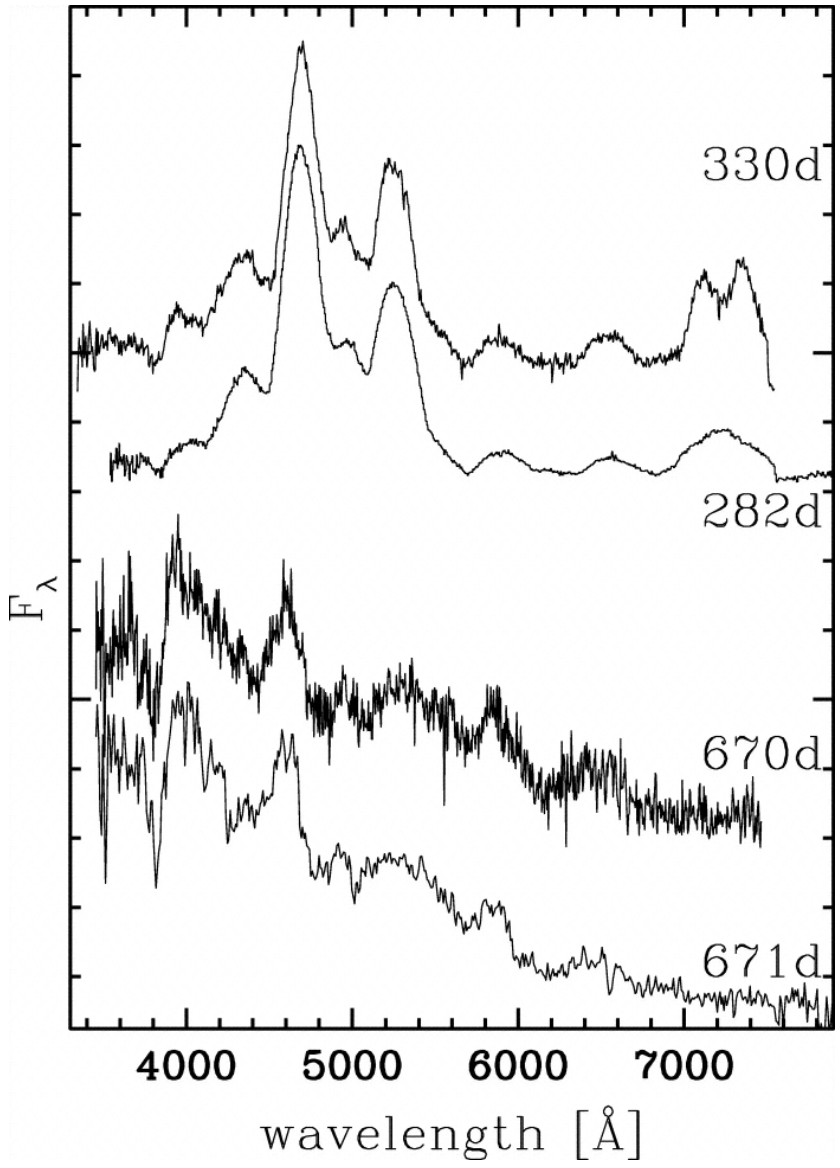

Figure 6.1: The spectra of SN 1998bu (thick) and SN 1991T (thin) at ∼1 and ∼2 yrs after explosion (Cappellaro et al., 2001). The nebular spectra ∼300 days past maximum are dominated by strong emission lines of Fe II and Fe III, while the echo spectra have broad absorption and emission features.

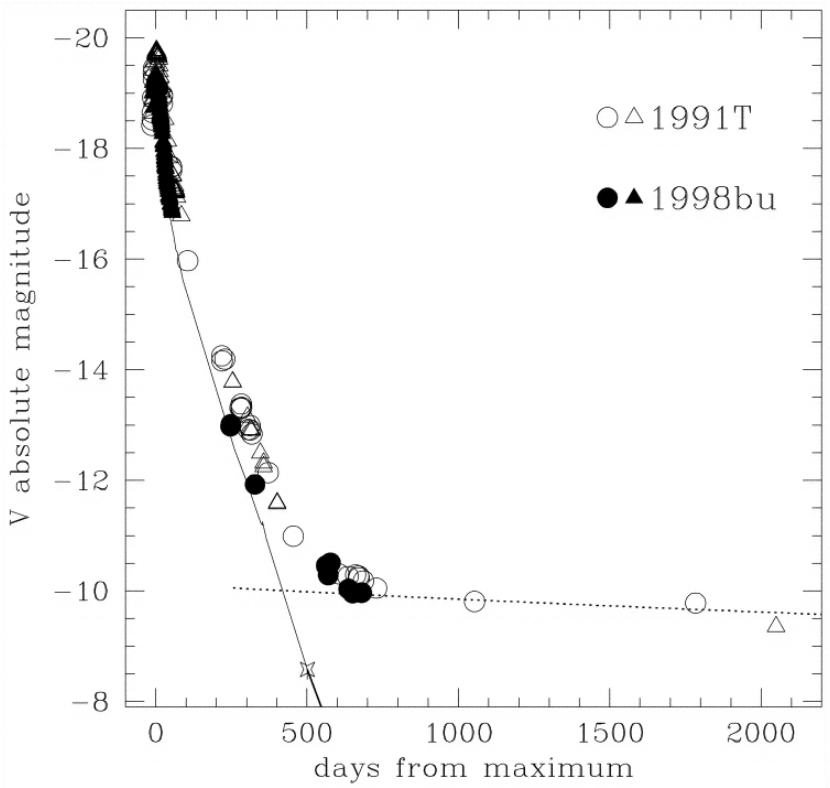

Figure 6.2: The V band light curve comparison of SN 1991T (open circles and triangles) and SN 1998bu (filled circles and triangles) from Cappellaro et al. (2001). Although this figure only includes the first light echo observations of SN 1998bu, the agreement between the two echoes is striking. The solid line is the normal decline of SN 1996X.

These first two SN Ia light echoes detections were monitored for over a decade and showcase the importance of light echo detections and extensive monitoring for observing the evolution of the echoes to astronomy. In future light echo searches, late-epoch observations of SN 1991T-like SNe should be the focus.

6.2 SN 2007af vs. SN 1998bu

Both of these SNe were classified as normal SNe Ia at peak by their spectra. However, SN 1998bu differed greatly from SN 2007af at peak. It featured a slow decline at maximum, and suffered more extinction ($A_V = 0.86$ mag compared to $A_V = 0.39$ mag for SN 2007af) (Cappellaro et al., 2001; Simon et al., 2007). While both SNe featured multiple echoes, the cases are very different. SN 1998bu was detected at a much earlier epoch, but since it was one of the first SNe Ia to be monitored to nebular epochs (due to the previous calibration of the host galaxy distance using Cepheid variable stars), the early detection is not surprising. Both SNe showed the characteristic flattening of the light curve due to an echo in each observed filter. *Hubble Space Telescope* observations confirmed the existence of both echoes, and in the case of SN 1998bu, spectra were also used to confirm the echo.

While for both SNe, the outer echoes have a larger optical depth, the similarities end there. The light echo rings are also not uniformly illuminated for SN 1998bu, suggesting patchy dust. In the case of two forward-scattered light echoes, the dust sheet distances are much further away from the source for SN 2007af (800 pc and 100 pc compared to 200 pc and 10 pc, respectively for SN 1998bu). SN 1998bu also featured an inner echo produced from an inclined dust sheet. The light echo colors are also quite different between outer and inner echoes for these SNe. SN 2007af featured echo colors that differed by $\sim$0.6 mag, while the echoes from SN 1998bu produced similar colors at each epoch. Although the SN 1998bu echo colors had a higher uncertainty, the values were more consistent with a typical forward-scattered Milky Way dust origin of the echoes. For SN 2007af, the outer echo color was not replicable using a forward-scattered scenario, but the inner echo was replicable by Mily Way-type dust.

Considerably more information can be inferred from the light echoes of SN 1998bu since the SN was observed six times as long as SN 2007af. With more observations of SN 2007af, more in-depth comparisons could be made. The echoes from SN 1998bu were unique because of their

extensive monitoring, and this case shows the importance of late-epoch observations of SNe Ia. With this work, the evolution of the echoes was further analyzed and compared to previous results from multiple teams. Further proposals to observe SN 2007af will be submitted in the future.

6.3 All SN Ia Light Echoes

I compare all of the Type Ia supernova light echo detections to date in Table 6.2. In the case of multiple echoes, the multiple distance values derived are listed, with the inner echo value coming first (for the case of SN 2007af, we quote the ISM value derived). The detection dates and ages of the SNe were taken from the literature: (SN 1991T (Sparks et al., 1999), SN 1995E (Quinn et al., 2006), SN 1998bu (Cappellaro et al., 2001), SN 2006X (W08), SN 2007af (Simon et al., 2007), 2009ig (Garnavich et al., 2013), and SN 2014J (Crotts, 2014)). When applicable, we list the dust distances derived from this research.

Table 6.2: SN Ia Light Echo Detections

SN	Echo Discovery	Epoch (days since B_{peak})	Dust Distance (pc)
SN 1991T	January 26, 1993	639	50
SN 1995E	September 4, 2001	2355	207 ± 35
SN 1998bu	December 4, 1999	554	10 ± 3, 190 ± 10
SN 2006X	December 24, 2006	308	80 ± 5
SN 2007af	January 8, 2010	1031	90 ± 20, 790 ± 60
SN 2009ig	November 17, 2011	802	190 ± 40
SN 2014J	September 9, 2014	234	80, 300

6.3.1 Change in Magnitude vs. Extinction

A relation between E(B – V) and Δm, the peak-echo magnitude difference accounting for extinction, can be determined, assuming the relationship between scattering and absorption is known. Table 6.3 lists the values of all reported SNe Ia light echoes including SN 2007af (using R_V = 2.6). A lower R_V was adopted after the dust analysis results. The combined magnitude for SN 2007af converted to standard Bessell magnitudes was used for this analysis (Bessell, 1990). The first three rows were taken from Quinn et al. (2006), and the SN 2006X E($B - V$) value was reported in W08. E(B – V) for SN 2007af comes from Simon et al. (2007). The ΔV values for SN 1998bu, SN 2006X, SN 2007af, and SN 2009ig were adopted from our analysis, where the total magnitude was also used

for SN 1998bu. The values are plotted in Figure 6.3, showing the excellent agreement between all of the SNe except SN 2014J and the Patat (2005) model for single and multiple scattering. For low optical depth values ($\tau \leq 1.0$), the light echo phenomenon is well described by single scattering. Auto-absorption and attenuation becomes significant for $\tau > 1.0$, and multiple scattering must be considered.

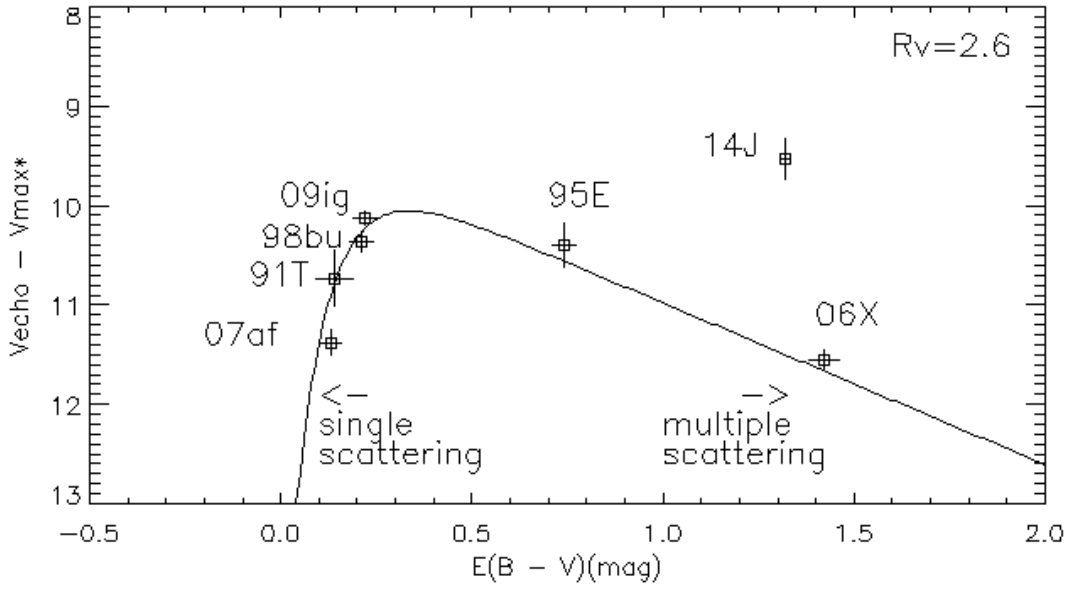

Figure 6.3: The difference in extinction corrected V peak to echo magnitude (total magnitude in the case of SN 2007af and SN 1998bu) compared to the Patat (2005) model for single and multiple scattering using a dust law of $R_V = 2.6$. The figure shows the similarity between the SNe Ia echoes and the excellent agreement to the model. SN 2014J is the only outlier in the plot (within the uncertainties).

SN 2007af featured a lower E(B – V) at peak than average SNe Ia and the lowest value of all light echo candidates to date. The fact that a significant portion of the sample of SNe Ia found with light echoes have low extinction values is surprising. SN 2007af showed nothing in its peak behavior to suggest the possibility of an echo at late epochs. The production of a light echo from such environments needs to be further explored. SN 2007af and SN 2006X both had colors not replicable by our model although they are at the opposite extremes of the extinction spectrum. For SN 2006X, the extreme peak colors and highly extinct spectrum are most likely the cause, but for SN 2007af, more in-depth analysis is needed.

We typically expect to see light echoes from highly reddened SNe since the peak behavior

Table 6.3: SN Ia Light Echo Comparisons

Supernova	E(B – V)(mag)	ΔV(mag)
SN 1991T	0.14 ± 0.05	10.73 ± 0.28
SN 1998bu	0.21 ± 0.04	10.37 ± 0.10
SN 1995E	0.74 ± 0.03	10.40 ± 0.22
SN 2006X	1.42 ± 0.04	11.55 ± 0.10
SN 2007af	0.13 ± 0.03	11.38 ± 0.13
SN 2009ig	0.22 ± 0.04	10.13 ± 0.07
SN 2014J	1.32 ± 0.01	9.53 ± 0.20

demonstrates the large amount of dust in the vicinity. However, only two out of the seven extra-galactic cases comes from a highly reddened SN. This could be a bias due to the lack of late-epoch monitoring of these SNe combined with the small sample size, but it is an interesting thing to note.

6.3.2 Host Galaxy Morphology

Following the discussion from Patat (2003) and Quinn et al. (2006) on the link between host galaxy morphology and SN type, we compare the host galaxies of known light echoes in this subsection.

Both SN 1991T and SN 1998bu featured a slow decline and exploded in SAB-liner (low-ionization nuclear emission-line region) galaxies. The host galaxies of these SNe (NGC 4527 and NGC 3368, respectively) have an enhanced star forming rate. Recent studies have shown evidence for a relationship between SN type and host galaxy classification. The peak brightness of SN Ia correlate with host galaxy morphology and star-formation history (Hamuy et al., 1996; Gallagher et al., 2005). Faint SNe usually occur in early-type galaxies (E/S0), and bright SNe (1991T-like) usually occur in spiral (Sbc or later) galaxies (Hakobyan et al., 2012).

SN 1995E and SN 2007af both exploded in Sc spiral galaxies (NGC 2441 and NGC 5584, respectively). The host galaxy of SN 2009ig was NGC 1015, a face-on Sb spiral galaxy. The explosion site was nearby a young and compact star cluster. SN 2006X and SN 2014J both exploded in starburst galaxies (M100, a grand-design spiral galaxy and M82, and edge-on irregular starburst galaxy). Interestingly, all of the host galaxies have large regions of star formation associated with them, and all except one are spiral galaxies. Since brighter SNe are found in spirals, which consist of large star-forming and dusty regions, these are the prime targets for future light echo searches.

Chapter 7

Conclusions

In this dissertation, we continue our late-epoch investigation of light echoes in Type Ia supernovae. We present the analysis of light echoes from four SNe Ia using ground-based images taken from Steward Observatory, Kitt Peak National Observatory, Mount Graham International Observatory, and space-based images taken from the *Hubble Space Telescope* data archive. We summarize our publication on the light echo from SN 2007af (Drozdov et al., 2014) and discuss the recent improvements to the work since Drozdov (2013). We introduce the light echo from SN 2009ig and continue the work of multiple teams in our analysis of the light echoes from SN 2006X and SN 1998bu.

We discuss the improved techniques and findings on the light echoes from SN 2007af in NGC 5584, which was recently accepted into the Astrophysical Journal. We also added ground-based compliments to our 2010 HST light echo observations from Steward and Kitt Peak National Observatory. We developed a new code to map the location of the light echo to accurately attribute counts to the correct source (outer echo, inner echo, background, or artifact), which improved our photometry. We used the WFC3 Instrument Handbook standard procedures in determining the VEGA magnitudes of our echoes using VEGA zeropoints of the appropriate filters (this was the same method used for all of our echo magnitudes). The code was also used to better constrain the angular sizes of our echoes, which were consistent with our previous results for the outer echo, while the inner echo size changed by $\sim 0.5''$. The distance determined between the dust and the SN were as follows: 800 ± 60 pc for the outer echo, 90 ± 20 pc for the inner echo using an ISM scenario, and 0.45 ± 0.01 pc using a CSM scenario.

We also developed another code to predict the light echo colors of a SN using various dust types and scattering scenarios. The inputs of the code were the peak SN spectrum, transmission filters of the desired filters from the *HST* Instrument Handbook, standard Vega spectrum (used for comparison), and the dust cross-sections from Draine (2003) for various dust types and scattering angles. The transmission filters were folded into the interpolated peak SN spectrum, scattered, and compared to the Vega spectrum. Then, the spectra were integrated over the full filter range. The magnitude of the color was determined in the standard method of converting from flux to magnitude. This process was used for all of our SNe. We also used the code to predict the peak color of the SN (which we compared to the observed color from the literature) and the magnitude differences between the standard and *HST* filters.

The outer echo color (F555W – F814W) of SN 2007af in VEGA magnitudes was very similar to peak value $V - I$ (-0.3 mag) reported, but the color could not be replicated by our three dust types in either the forward or back-scattering regime. On the other hand, the inner echo color (-0.9 mag) was consistent with forward scattering, but due to large uncertainties, we were not able to distinguish between types. Because SN 2007af was a normal SN Ia, the differences between the VEGA magnitudes and standard magnitudes were minor. Future work remains to understand the outer echo, and with deeper observations, we would be able to monitor the growth of the outer echo ring and observe the evolution.

After searching the *Hubble Space Telescope* archive, unpublished public observations of the light echoes from SN 2006X and SN 1998bu were discovered. For SN 2006X, only three images (F475W, F555W, and F775W) in 2009 (>1300days past maximum) were found. For SN 1998bu, we were able to obtain observations in the F336W, F438W, F475W, F555W, F606W, and F625W filters taken with the ACS and WFC3 from 2003 – 2014. Photometry of both SNe echoes (and SN 2009ig) was determined using DAOPHOT in IRAF. Because these two cases were previously detected by multiple teams, we were able to compare and contrast our findings.

The magnitudes of the light echo from SN 2006X were 22.3 ± 0.1 mag for F475W, 21.9 ± 0.1 mag for F555W, and 21.7 ± 0.1 mag for F775W. Using the angular size of $\sim 0.2''$ and the distance to NGC 4321 of 15.2 Mpc, the dust was calculated to be 80 ± 5 pc in front of the SN. The heavily reddened nature of SN 2006X at peak (E(B – V) = 1.42 mag) proved problematic in our dust color analysis. After obtaining a peak spectrum of SN 2006X from the Asiago Supernova Catalogue, our dust color predictions were radically different from the observed peak and light echo colors at shorter

wavelengths (0.4 ± 0.01 mag for F475W – F555W). However, the code did produce reliable results in the F555W – F775W regime, where not only did the peak theoretical color match, but also, the most favorable prediction to match the 0.2 ± 0.01 mag color observed was forward-scattering of our lowest R_V value dust type (LMC). From this SN, we illustrated that the spectra of a source dramatically affects the filter colors, and simply labeling the *HST* filters by their conventional nomenclature (i.e. *V*) results in as much as ∼0.5 mag of difference in these heavily reddened SNe.

SN 1998bu resulted in the best comparable case to SN 2007af because of the similar multi-echo structure. Due to the wealth of observations of this SN, the evolution of the echo was extensively monitored, and the angular size of both echoes grew at a rate consistent with a dust distance of 190 ± 10 pc and 10 ± 3 pc for the outer and inner echo, respectively. The inner echo was shown to be slightly off center from the SN explosion site, resulting in an inclination of the dust sheet of ∼30°. The brightness of both echoes is clearly fading, which is visually evident in the 2014 images. We obtained a peak spectrum of SN 1998bu from the WISeREP archive. Unfortunately, the spectrum did not include the UV wavelengths, and thus, we were unable to include the F336W color in our analysis. While SN 1998bu exhibited normal SN Ia behavior at peak, which was reflected in the spectrum, our high uncertainties made it impossible to discriminate between dust types. However, we do conclude that the most favorable scenario was 0° scattering of MW-type dust. This is consistent with the line-of-sight reddening value assumed at peak. The light echo(s) from SN 1998bu showed many similarities to the light echo from SN 1991T, and we also discuss those findings.

We briefly introduce the new light echo detection of SN 2009ig, which was discovered in late-epoch LBT observations. We add Steward and Kitt Peak National Observatory observations to the late-light curve of the SN. Just like in the case of SN 2007af, the host galaxy of SN 2009ig, NGC 1015 was included in a Cepheid campaign from June – October 2013 in the F160W, F350LP, F555W, and F814W filters. Unfortunately, issues with the *HST* archive retrieval system resulted in our completed analysis of only the first epoch of observations. Adopting a host galaxy distance of 39 Mpc, we determined the distance of the dust to be 190 ± 40 pc in front of the SN. The echo had a FWHM 2.4 times extended than the local field stars. The magnitudes of the *HST* observations were determined to be 24.4 ± 0.12 for the F350LP filter, 24.5 ± 0.02 for the F555W filter, and 26.2 ± 0.30 for the F814W filter. Clearly, the echo is very blue, and the extreme color was not replicable with our analysis using a peak spectrum from Foley et al. (2012). However, the small magnitude differences between the *HST* and standard filters suggests that abnormal dust or photometry issues

are responsible for the dispersion between the values in this case. When all of the HST data is finally analyzed, we will have the best light echo comparison case to SN 2007af.

In our last chapter, we compare all of the light echo cases to date, and discuss the similarities and differences between them. All of the light echo cases follow the trend of the single- and multiple-scattering Patat (2005) model, except for SN 2014J. Because of the early detection of that light echo, further observations are necessary, once the intrinsic SN emission has declined to confirm the echo discovery. In this dissertation, we further investigate 4 out of a total 7 extragalactic light echo detections in Type Ia supernovae. With further late-epoch monitoring of prime light echo candidates in SNe Ia, we aim to add discoveries to this small sample and increase our understanding of these exploding stars.

7.1 Future Work

While we present a detailed summary and continued monitoring for multiple Type Ia supernova light echoes, more work remains. With more data publicly available for some of these SNe, we have more observations to analyze and use to answer the questions that have arisen during our findings. In particular, the dust color of the light echoes from SN 2007af, SN 2006X, and SN 2009ig needs to be further explored. Further observations need to be analyzed for SN 1998bu and SN 2009ig.

7.1.1 SN 2007af

The extreme blue color of the outer echo from SN 2007af was not replicable by our analysis. First, we must consider atypical dust. Because the outer echo is faint in contrast to the complex background, careful host galaxy subtraction is needed to eliminate background contamination to improve photometry. Preliminary attempts proved unsuccessful, and more rigorous algorithms and higher caliber subtractions images will be used in the future. In particular, we want to utilize the host galaxy subtraction software, the High Order Transform of PSF and Template Subtraction (HOTPANTS), for this work.[7] More deep observations of SN 2007af are necessary to investigate the color further and monitor the evolution and growth of both echoes.

[7] http://www.astro.washington.edu/users/becker/hotpants.html

7.1.2 SN 2006X

The $B - V$ (F475W – F555W) color of SN 2006X needs further attention. The color output from the code was even incorrect in predicting the peak color, which suggests more complex processes needs to be implemented. Due to the large line-of-sight extinction seen at peak for SN 2006X, multiple scattering needs to be considered in the dust color analysis, which could possibly account for the extreme color differences between the observed and theoretical color of this light echo. Following the work of Patat (2005), we need to modify our code to include multiple scattering.

7.1.3 SN 1998bu

The light echoes from SN 1998bu have been investigated for >15 years, yet previously unpublished public data is still available. More observations in the *Hubble Space Telescope* archive exist and need to be downloaded, analyzed, and compared with the findings of this dissertation. Observations taken in the F450W, F555W, and F606W filters in 2001 and 2002 are in the archive, waiting for analysis. We also need to develop a way to use the polarization images obtained with the ACS in 2003 and 2006 in our analysis. Photometry using the polarization images for the light echo from SN 1991T (from the same *HST* proposal) have been published (Sparks et al., 1999), and that paper needs to be studied in detail to follow the same procedure with the polarization observations of SN 1998bu for magnitude determinations. Next, we could also use those images to attempt to search for polarization detections, which in turn, could be used to estimate the distance to the host galaxy of SN 1998bu in the same method as was used for SN 1991T.

7.1.4 SN 2009ig

In this dissertation, we simply introduced the light echo from SN 2009ig, and as was mentioned in Chapter 5, plenty of images remain to be analyzed. The major hurdle for our future work for SN 2009ig is to download the final fully reduced and calibrated images from the *HST* archive. Unfortunately, several attempts of this have resulted in peculiar images that appeared to not have been drizzled (see Figure 7.1). Photometry on these images produced values dissimilar to the ones presented in this dissertation. We either need to figure out a way to finish calibrating these images ourselves using standard *HST* software, DrizzlePac (Gonzaga and et al., 2012), or ask for the entire data set from our collaborators. We also need to recalibrate the field of SN 2009ig using our early

ground-based calibrations to include the magnitudes of more local stars in the HST field to improve the accuracy of our photometry.

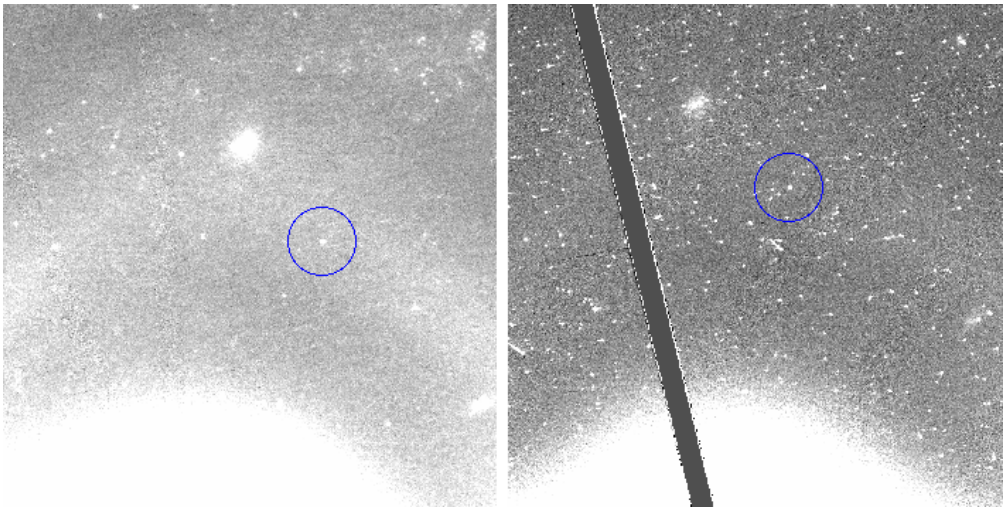

Figure 7.1: Side-by-side 30″ x 30″ images of NGC 1015 taken in the F555W filter on June 30, 2013 showing the stark contrast between archived data (right panel) and fully reduced and calibrated data (left panel). The left panel was given to us from a collaborator, while the right panel shows the fully reduced image downloaded directly from the HST archive. The light echo is shown in the 2″ blue outlined region.

Once we have access to the fully reduced images, we can continue our angular size, photometry, dust distance derivations, and light echo color analysis for all epochs in the Cepheid campaign. After this is completed, we will have the best comparable case to SN 2007af since both were captured with the same filters using the same instrument on HST. The results of the first epoch of the Cepheid campaign show a similar color dependence as SN 2007af, so this work is of utmost importance in our future endeavors. The dust color predictions did not match our one epoch of observations. We must continue our analysis on the full data, to see if the same color relationship holds throughout. We also have a $Swift$ spectrum at a comparable epoch, and we need to investigate if there is a method to combine our spectra to widen the wavelength range. Then, we would be able to discuss results of the F350LP – F555W color as well. We have already shown that assuming a normal SN Ia peak spectrum can alter the results of the dust color work drastically, so having the actual SN spectrum is vital for this part of the work. Also, as is clear from the light curve, SN 2009ig did deviate from the normal template pretty significantly, which is another reason why we cannot simply substitute a template (like in the case of SN 2007af). SN 2009ig had high velocity features in

the spectrum, which would not be replicable if we simply used a template. Our collaborators have already started working on the paper to publish the results from the light echo from SN 2009ig.

Appendices

Appendix A Ground- Versus Space-Based Filter Differences

In the literature, the *Hubble Space Telescope* WFC3 filters are often referred to as $UBVRI$ filters, but in reality, the filters are quite different. In this appendix, we compare the WFC3 filters with various standard systems (Bessell, Johnson-Cousins, Strömgren, and Sloan digital Sky Survey (SDSS)), showing the systematic differences between them. The magnitude difference between the standard and WFC3 filters depends on the spectrum of the target object. Thus, these values only hold for normal Type Ia supernovae.

Using the same method as described in our dust analysis section (see Subsection 3.4.2), we calculate the differences between standard $UBVRI$ Bessell filters (Bessell, 1990) and the HST WFC3 $UVIS$ filters using a peak Branch normal SN Ia spectrum (Nugent et al., 2002) compared to the spectrum of Vega (Table 1). Unlike our dust analysis, the response functions were simply folded with the spectra and not scattered. The WFC3 filter responses and filter specifics were taken from the WFC3 Instrument Handbook (note in the WFC3 convention, W stands for *wide-band*, LP stands for *long pass*, M stands for *medium-band*, and X stands for *extremely wide*). As defined in the instrument handbook, the filter widths listed are, "passband rectangular widths, defined as the equivalent width divided by the maximum throughput within the filter bandpass. Equivalent width is the integral with respect to wavelength of the throughput across the filter passband."

Table 1: WFC3 – Bessell Filter Differences

WFC3 Filter Names	Filter Description	Filter Width Å	Difference (mag)
F225W	UV wide	467	U – F225W = -0.118
F275W	UV wide	398	U – F275W = -0.326
F336W	Strömgren u	511	U – F336W = 0.228
F350LP	Long Pass	4758	U – F350LP = -0.134
F410M	Strömgren v	172	B – F410M = 0.180
F438W	WFPC2 B	618	B – F438W = 0.033
F467M	Strömgren b	201	B – F467M = -0.154
F475W	SDSS g	1344	B – F475W = -0.080
F475X	Extremely Wide Blue	2056	B – F475X = -0.036
F547M	Strömgren y	650	V – F547M = 0.030
F555W	WFPC2 V	1562	V – F555W = -0.022
F606W	WFPC2 Wide V	2182	V – F606W = -0.014
F600LP	Long Pass	2292	R – F600LP = -0.102
F625W	SDSS r	1463	R – F625W = 0.062
F775W	SDSS i	1171	I – F775W = -0.160
F814W	WFPC2 Wide I	1536	I – F814W = 0.005
F850LP	SDSS z	1182	I – F850LP = 0.116

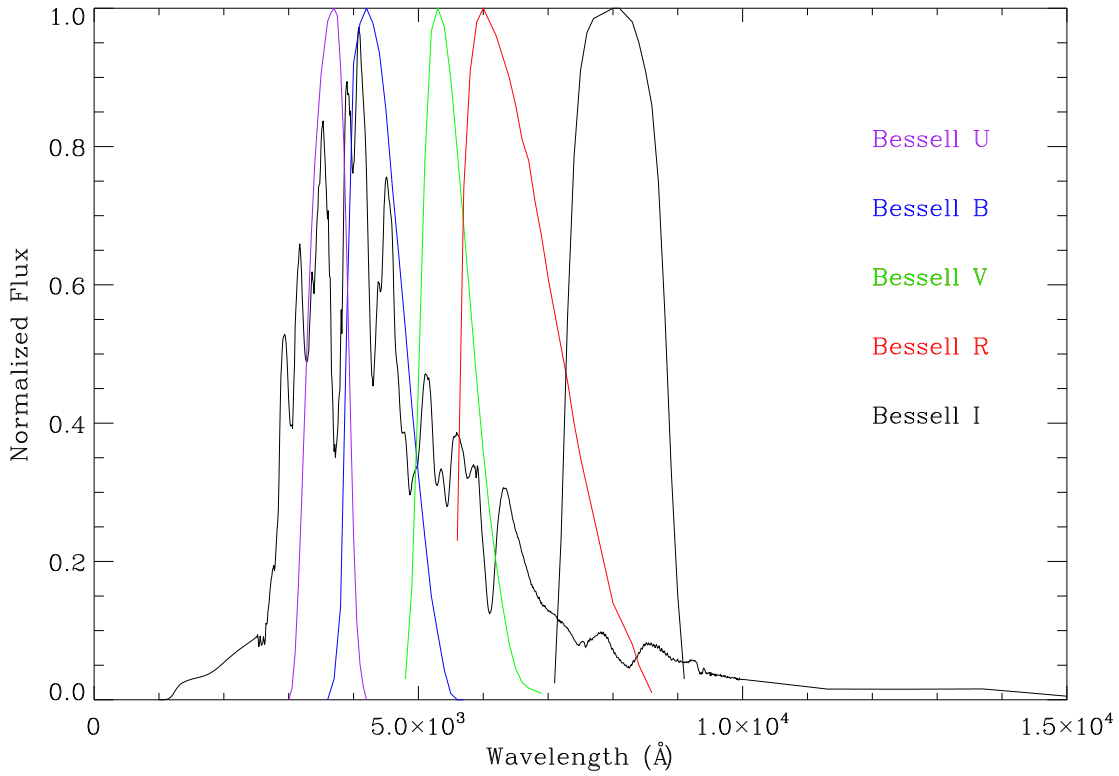

Figure 2: The standard $UBVRI$ Bessell filters (Bessell, 1990) are overplotted on a peak Branch normal Type Ia supernova, where the flux has been normalized (Nugent et al., 2002).

Next, we present the results of the WFC3 magnitude differences with the UBV Johnson and RI Cousins standard filters in Table 2 (Johnson and Morgan, 1951; Cousins, 1974). Both the Bessell and Johnson-Cousins filters are broadband filters, and other than the wide U filters, the differences between the wide WFC3 and standard filters are typically <0.1 mag. The U filters show the largest deviation from the standard filters. These results illustrate how erroneous simply calling HST filters by their standard equivalents can be for Type Ia supernovae.

In Table 3, we compare the Strömgren *uvby* standard filters with the WFC3 Strömgren equivalent filters. The Strömgren filter throughputs were taken from the Kitt Peak National Observatory filter data. As is evident in the results, the differences amount to ∼0.1 mag in some cases, showing that even in the HST equivalent of the standard filters, there are still systematic differences between the filters. This same trend is shown in the SDSS filter differences (Table 4). The SDSS filter throughputs were taken from Gunn et al. (1998). We plot both the standard filters compared

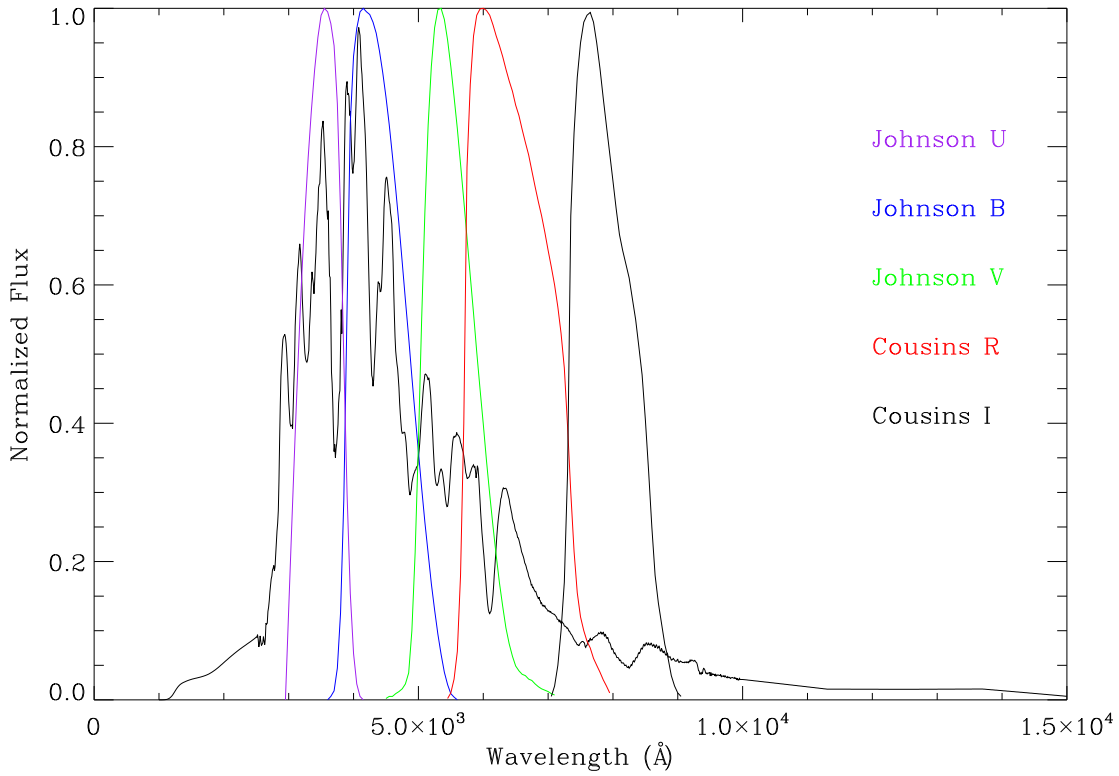

Figure 3: In this plot, we show the standard UVBRI Johnson-Cousins filters overimposed on the normalizes SN Ia peak spectrum (Nugent et al., 2002). These filters are very similar to the Bessell UBVRI standard filters.

Table 2: WFC3 – Johnson-Cousins Filter Differences

WFC3 Filter Names	Filter Description	Difference (mag)
F225W	UV wide	U – F225W = -0.195
F275W	UV wide	U – F275W = -0.303
F336W	Strömgren u	U – F336W = 0.158
F350LP	Long Pass	U – F350LP = -0.178
F410M	Strömgren v	B – F410M = 0.181
F438W	WFPC2 B	B – F438W = 0.034
F467M	Strömgren b	B – F467M = -0.153
F475W	SDSS g	B – F475W = -0.079
F475X	Extremely Wide Blue	B – F475X = -0.041
F547M	Strömgren y	V – F547M = 0.086
F555W	WFPC2 V	V – F555W = 0.051
F606W	WFPC2 Wide V	V – F606W = 0.013
F600LP	Long Pass	R – F600LP = -0.080
F625W	SDSS r	R – F625W = 0.051
F775W	SDSS i	I – F775W = 0.014
F814W	WFPC2 Wide I	I – F814W = 0.036
F850LP	SDSS z	I – F850LP = 0.171

to their WFC3 equivalents in Figures 4 and 5. The Strömgren filters are most visibly different from their WFC3 UVIS equivalents, especially in the u, where the F336W filter is actually shifted from the the standard filter center (this is also true to a lesser extent for F467M). The F547M is also much wider than its standard counterpart. On the other hand, the SDSS filters show good agreement with their WFC3 UVIS equivalents, which can be clearly seen in the comparison between their filter responses.

Table 3: WFC3 – Strömgren Filter Differences

WFC3 Filter Names	Filter Description	Difference (mag)
F336W	Strömgren u	Strömgren u – F336W = -0.113
F410M	Strömgren v	Strömgren v – F410M = -0.019
F467M	Strömgren b	Strömgren b – F467M = 0.101
F547M	Strömgren y	Strömgren y – F547M = -0.004

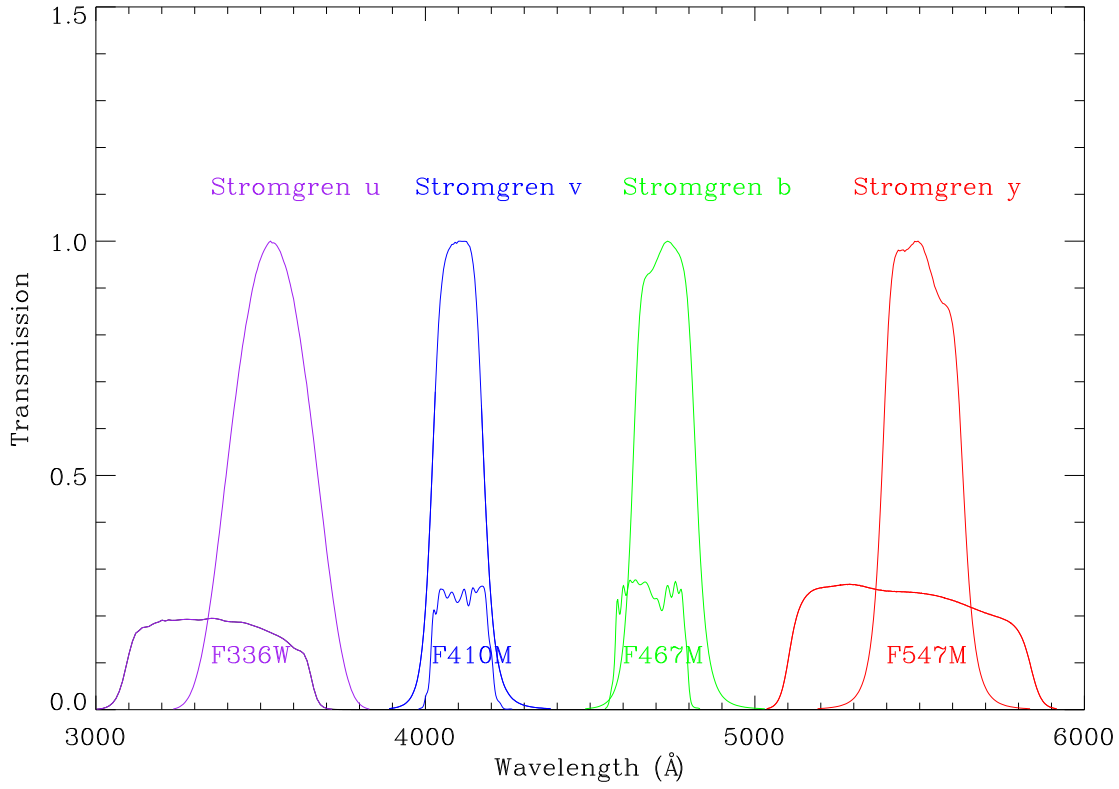

Figure 4: This plot shows the WFC3 and Strömgren transmission filter curves taken from the WFC3 and Kitt Peak instrument handbooks. The most noticeable mismatch between the Strömgren standard filter and WFC3 equivalent is in the u, where a wide filter is used. This also corresponds to the largest magnitude difference from our code. The F467M filter is shifted slightly off-center from that of the standard equivalent, which corresponds to a $\sim$0.1 mag difference.

Table 4: WFC3 – SDSS Filter Differences

WFC3 Filter Names	Filter Description	Difference (mag)
F475W	SDSS g	SDSS g – F475W = -0.017
F625W	SDSS r	SDSS r – F625W = -0.026
F775W	SDSS i	SDSS i – F775W = -0.025
F850LP	SDSS z	SDSS z – F850LP = -0.015

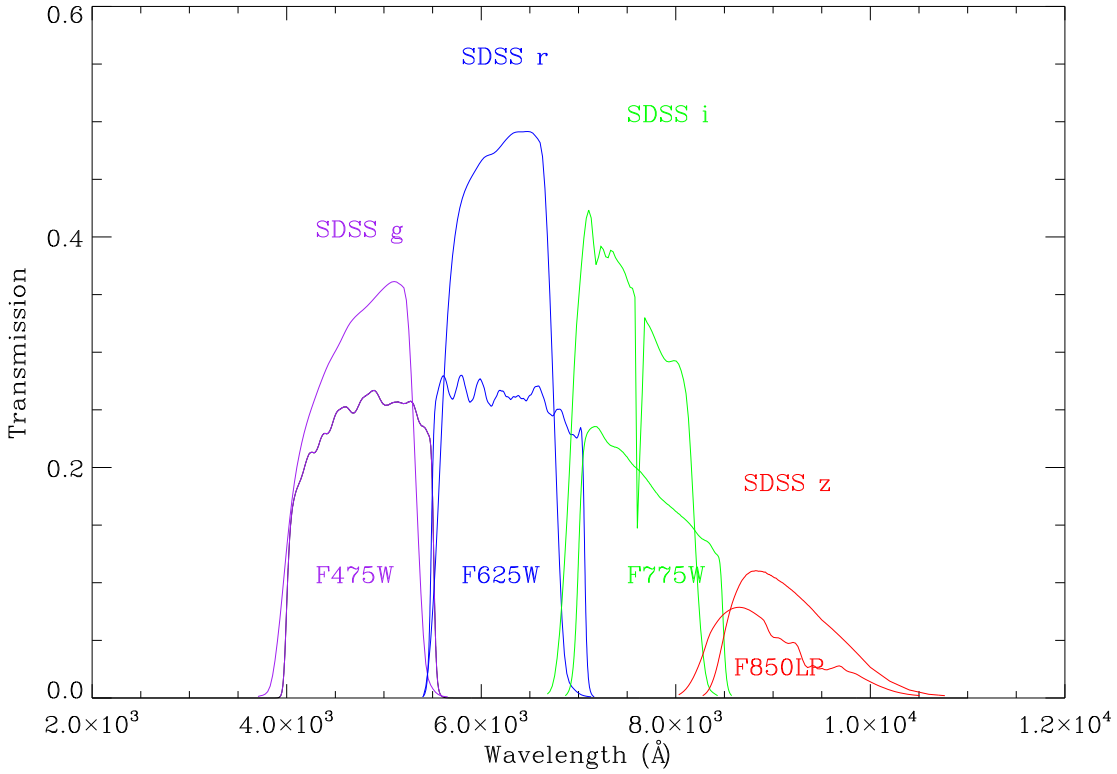

Figure 5: This plot shows the WFC3 and SDSS transmission filter curves taken from the WFC3 instrument handbook and Gunn et al. (1998). The figure shows the subtle differences between the WFC3-SDSS filter equivalents and the actual SDSS filters. As is shown by the magnitude differences between them, the SDSS filter equivalents in *HST* reproduce the standard filters very well, and the filter centers are aligned.

Bibliography

Ayani, K., Nakatani, H., Yamaoka, H., Meikle, P., Hernandez, M., Fassia, A., Iglesias, J., Skiff, B. A., Faranda, Jr., C., Spratt, C. E., Baransky, A., and Hornoch, K. 1998. Supernova 1998bu in NGC 3368. *International Astronomical Union Circulars 6905*, 1.

Barberà, C., Athanassoula, E., and García-Gómez, C. 2004. Deprojecting spiral galaxies using Fourier analysis. Application to the Frei sample. *Astronomy and Astrophysics 415*, 849–861.

Barbon, R., Buondí, V., Cappellaro, E., and Turatto, M. 1999. The Asiago Supernova Catalogue - 10 years after. *Astronomy and Astrophysics, Supplement 139*, 531–536.

Benetti, S., Meikle, P., Stehle, M., Altavilla, G., Desidera, S., Folatelli, G., Goobar, A., Mattila, S., Mendez, J., Navasardyan, H., Pastorello, A., Patat, F., Riello, M., Ruiz-Lapuente, P., Tsvetkov, D., Turatto, M., Mazzali, P., and Hillebrandt, W. 2004. Supernova 2002bo: inadequacy of the single parameter description. *Monthly Notices of the Royal Astronomical Society 348*, 261–278.

Bessell, M. S. 1990. UBVRI passbands. *Publications of the Astronomical Society of the Pacifics 102*, 1181–1199.

Blondin, S., Dessart, L., Hillier, D. J., and Khokhlov, A. M. 2013. One-dimensional delayed-detonation models of Type Ia supernovae: confrontation to observations at bolometric maximum. *Monthly Notices of the Royal Astronomical Society 429*, 2127–2142.

Boffi, F. R., Sparks, W. B., and Macchetto, F. D. 1999. A search for candidate light echoes: Photometry of supernova environments. *Astronomy and Astrophysics, Supplement 138*, 253–266.

Bond, H. E., Henden, A., Levay, Z. G., Panagia, N., Sparks, W. B., Starrfield, S., Wagner, R. M., Corradi, R. L. M., and Munari, U. 2003. An energetic stellar outburst accompanied by circumstellar light echoes. *Nature 422*, 405–408.

Brown, P. J., Dawson, K. S., de Pasquale, M., Gronwall, C., Holland, S., Immler, S., Kuin, P., Mazzali, P., Milne, P., Oates, S., and Siegel, M. 2012. A Swift Look at SN 2011fe: The Earliest Ultraviolet Observations of a Type Ia Supernova. *Astrophysical Journal 753*, 22.

Cappellaro, E., Patat, F., Mazzali, P. A., Benetti, S., Danziger, J. I., Pastorello, A., Rizzi, L., Salvo, M., and Turatto, M. 2001. Detection of a Light Echo from SN 1998BU. *Astrophysical Journal, Letters 549*, L215–L218.

Chan, K.-W. and Lingenfelter, R. E. 1993. Positrons from supernovae. *Astrophysical Journal 405*, 614–636.

Contreras, C., Hamuy, M., Phillips, M. M., Folatelli, G., Suntzeff, N. B., Persson, S. E., Stritzinger, M., Boldt, L., González, S., Krzeminski, W., Morrell, N., Roth, M., Salgado, F., José Maureira, M., Burns, C. R., Freedman, W. L., Madore, B. F., Murphy, D., Wyatt, P., Li, W., and Filippenko, A. V. 2010. The Carnegie Supernova Project: First Photometry Data Release of Low-Redshift Type Ia Supernovae. *Astronomical Journal 139*, 519–539.

Couderc, P. 1939. Les auréoles lumineuses des novae. *Annales d'Astrophysique 2*, 271.

Cousins, A. W. J. 1974. Standard Stars for VRI Photometry with S25 Response Photocathodes [Errata: 1974MNSSA..33....1C]. *Monthly Notes of the Astronomical Society of South Africa 33*, 149.

Crause, L. A., Lawson, W. A., Menzies, J. W., and Marang, F. 2005. V838 Mon: light echo evolution and distance estimate. *Monthly Notices of the Royal Astronomical Society 358*, 1352–1360.

Crotts, A. 2014. Light Echoes From Supernova 2014J in M82. *ArXiv e-prints*.

Crotts, A. P. S. and Yourdon, D. 2008. The Nature and Geometry of the Light Echo from SN 2006X. *Astrophysical Journal 689*, 1186–1190.

Dittmann, J. A., Soderberg, A. M., Chomiuk, L., Margutti, R., Goss, W. M., Milisavljevic, D., and Chevalier, R. A. 2014. A Mid-life Crisis? Sudden Changes in Radio and X-Ray Emission from Supernova 1970G. *Astrophysical Journal 788*, 38.

Dolphin, A. E. 2000. The Charge-Transfer Efficiency and Calibration of WFPC2. *Publications of the Astronomical Society of the Pacific 112*, 1397–1410.

Draine, B. T. 2003. Scattering by Interstellar Dust Grains. I. Optical and Ultraviolet. *Astrophysical Journal 598*, 1017–1025.

Drozdov, D. 2013. The Detection of a Light Echo from SN 2007af. M.S. thesis, Clemson University.

Drozdov, D., Leising, M. D., Milne, P. A., Pearcy, J., Riess, A. G., Macri, L. M., Bryngelson, G. L., and Garnavich, P. M. 2014. Detection of a Light Echo from the Otherwise Normal SN 2007af. *ArXiv e-prints*.

Foley, R. J., Challis, P. J., Filippenko, A. V., Ganeshalingam, M., Landsman, W., Li, W., Marion, G. H., Silverman, J. M., Beaton, R. L., Bennert, V. N., Cenko, S. B., Childress, M., Guhathakurta, P., Jiang, L., Kalirai, J. S., Kirshner, R. P., Stockton, A., Tollerud, E. J., Vinkó, J., Wheeler, J. C., and Woo, J.-H. 2012. Very Early Ultraviolet and Optical Observations of the Type Ia Supernova 2009ig. *Astrophysical Journal 744*, 38.

Förster, F., González-Gaitán, S., Folatelli, G., and Morrell, N. 2013. On the Lira Law and the Nature of Extinction toward Type Ia Supernovae. *Astrophysical Journal 772*, 19.

Fruscione, A., McDowell, J. C., Allen, G. E., Brickhouse, N. S., Burke, D. J., Davis, J. E., Durham, N., Elvis, M., Galle, E. C., Harris, D. E., Huenemoerder, D. P., Houck, J. C., Ishibashi, B., Karovska, M., Nicastro, F., Noble, M. S., Nowak, M. A., Primini, F. A., Siemiginowska, A., Smith, R. K., and Wise, M. 2006. CIAO: Chandra's data analysis system. In *Society of Photo-Optical Instrumentation Engineers (SPIE) Conference Series*. Society of Photo-Optical Instrumentation Engineers (SPIE) Conference Series, vol. 6270.

Gallagher, J. S., Garnavich, P. M., Berlind, P., Challis, P., Jha, S., and Kirshner, R. P. 2005. Chemistry and Star Formation in the Host Galaxies of Type Ia Supernovae. *Astrophysical Journal 634*, 210–226.

Ganeshalingam, M., Li, W., Filippenko, A. V., Anderson, C., Foster, G., Gates, E. L., Griffith, C. V., Grigsby, B. J., Joubert, N., Leja, J., Lowe, T. B., Macomber, B., Pritchard, T., Thrasher, P., and Winslow, D. 2010. Light curves for 165 SNe (Ganeshalingam+, 2010). *VizieR Online Data Catalog 219*, 418.

Garnavich, P. M., Kirshner, R. P., Challis, P., Jha, S., Branch, D., Chevalier, R., Filippenko, A. V., Li, W., Fransson, C., Lundqvist, P., McCray, R., Panagia, N., Phillips, M. M., Pun, C. S. J., Sonneborn, G., Schmidt, B. P., Suntzeff, N. B., Wheeler, J. C., and Supernova INtensive Study SINS Collaboration. 2001. Echos of SN 1998bu. In *American Astronomical Society Meeting Abstracts*. Bulletin of the American Astronomical Society, vol. 33. 1370.

Garnavich, P. M., Milne, P., Bryngelson, G. L., and Leising, M. D. 2013. A Light Echo Candidate from Supernova 2009ig. In *American Astronomical Society Meeting Abstracts*. American Astronomical Society Meeting Abstracts, vol. 222. 209.04.

Gerardy, C. L., Höflich, P., Fesen, R. A., Marion, G. H., Nomoto, K., Quimby, R., Schaefer, B. E., Wang, L., and Wheeler, J. C. 2004. SN 2003du: Signatures of the Circumstellar Environment in a Normal Type Ia Supernova? *Astrophysical Journal 607*, 391–405.

Gonzaga, S. and et al. 2012. *The DrizzlePac Handbook*.

Goobar, A. 2008. Low R_V from Circumstellar Dust around Supernovae. *Astrophysical Journal, Letters 686*, L103–L106.

Gunn, J. E., Carr, M., Rockosi, C., Sekiguchi, M., Berry, K., Elms, B., de Haas, E., Ivezić, Ž., Knapp, G., Lupton, R., Pauls, G., Simcoe, R., Hirsch, R., Sanford, D., Wang, S., York, D., Harris, F., Annis, J., Bartozek, L., Boroski, W., Bakken, J., Haldeman, M., Kent, S., Holm, S., Holmgren, D., Petravick, D., Prosapio, A., Rechenmacher, R., Doi, M., Fukugita, M., Shimasaku, K., Okada, N., Hull, C., Siegmund, W., Mannery, E., Blouke, M., Heidtman, D., Schneider, D., Lucinio, R., and Brinkman, J. 1998. The Sloan Digital Sky Survey Photometric Camera. *Astronomical Journal 116*, 3040–3081.

Hakobyan, A. A., Adibekyan, V. Z., Aramyan, L. S., Petrosian, A. R., Gomes, J. M., Mamon, G. A., Kunth, D., and Turatto, M. 2012. Supernovae and their host galaxies. I. The SDSS DR8 database and statistics. *Astronomy and Astrophysics 544*, A81.

Hamuy, M., Phillips, M. M., Suntzeff, N. B., Schommer, R. A., Maza, J., Smith, R. C., Lira, P., and Aviles, R. 1996. The Morphology of Type IA Supernovae Light Curves. *Astronomical Journal 112*, 2438.

Hernandez, M., Meikle, W. P. S., Aparicio, A., Benn, C. R., Burleigh, M. R., Chrysostomou, A. C., Fernandes, A. J. L., Geballe, T. R., Hammersley, P. L., Iglesias-Paramo, J., James, D. J., James, P. A., Kemp, S. N., Lister, T. A., Martinez-Delgado, D., Oscoz, A., Pollacco, D. L., Rozas, M., Smartt, S. J., Sorensen, P., Swaters, R. A., Telting, J. H., Vacca, W. D., Walton, N. A., and Zapatero-Osorio, M. R. 2000. An early-time infrared and optical study of the Type Ia Supernova 1998bu in M96. *Monthly Notices of the Royal Astronomical Society 319*, 223–234.

Hicken, M., Challis, P., Jha, S., Kirshner, R. P., Matheson, T., Modjaz, M., Rest, A., Wood-Vasey, W. M., Bakos, G., Barton, E. J., Berlind, P., Bragg, A., Briceño, C., Brown, W. R., Caldwell, N., Calkins, M., Cho, R., Ciupik, L., Contreras, M., Dendy, K.-C., Dosaj, A., Durham, N., Eriksen, K., Esquerdo, G., Everett, M., Falco, E., Fernandez, J., Gaba, A., Garnavich, P., Graves, G., Green, P., Groner, T., Hergenrother, C., Holman, M. J., Hradecky, V., Huchra, J., Hutchison, B., Jerius, D., Jordan, A., Kilgard, R., Krauss, M., Luhman, K., Macri, L., Marrone, D., McDowell, J., McIntosh, D., McNamara, B., Megeath, T., Mochejska, B., Munoz, D., Muzerolle, J., Naranjo, O., Narayan, G., Pahre, M., Peters, W., Peterson, D., Rines, K., Ripman, B., Roussanova, A., Schild, R., Sicilia-Aguilar, A., Sokoloski, J., Smalley, K., Smith, A., Spahr, T., Stanek, K. Z., Barmby, P., Blondin, S., Stubbs, C. W., Szentgyorgyi, A., Torres, M. A. P., Vaz, A., Vikhlinin, A., Wang, Z., Westover, M., Woods, D., and Zhao, P. 2009. CfA3: 185 Type Ia Supernova Light Curves from the CfA. *Astrophysical Journal 700*, 331–357.

Humphreys, E. M. L., Reid, M. J., Moran, J. M., Greenhill, L. J., and Argon, A. L. 2013. Toward a New Geometric Distance to the Active Galaxy NGC 4258. III. Final Results and the Hubble Constant. *Astrophysical Journal 775*, 13.

Hwang, U., Laming, J. M., Badenes, C., Berendse, F., Blondin, J., Cioffi, D., DeLaney, T., Dewey, D., Fesen, R., Flanagan, K. A., Fryer, C. L., Ghavamian, P., Hughes, J. P., Morse, J. A., Plucinsky, P. P., Petre, R., Pohl, M., Rudnick, L., Sankrit, R., Slane, P. O., Smith, R. K., Vink, J., and Warren, J. S. 2004. A Million Second Chandra View of Cassiopeia A. *Astrophysical Journal, Letters 615*, L117–L120.

Jha, S., Garnavich, P. M., Kirshner, R. P., Challis, P., Soderberg, A. M., Macri, L. M., Huchra, J. P., Barmby, P., Barton, E. J., Berlind, P., Brown, W. R., Caldwell, N., Calkins, M. L., Kannappan, S. J., Koranyi, D. M., Pahre, M. A., Rines, K. J., Stanek, K. Z., Stefanik, R. P., Szentgyorgyi, A. H., Väisänen, P., Wang, Z., Zajac, J. M., Riess, A. G., Filippenko, A. V., Li, W., Modjaz, M., Treffers, R. R., Hergenrother, C. W., Grebel, E. K., Seitzer, P., Jacoby, G. H., Benson, P. J., Rizvi, A., Marschall, L. A., Goldader, J. D., Beasley, M., Vacca, W. D., Leibundgut, B., Spyromilio, J., Schmidt, B. P., and Wood, P. R. 1999. The Type IA Supernova 1998BU in M96 and the Hubble Constant. *Astrophysical Journal, Supplement 125*, 73–97.

Johnson, H. L. and Morgan, W. W. 1951. On the Color-Magnitude Diagram of the Pleiades. *Astrophysical Journal 114*, 522.

Kleiser, I., Cenko, S., Li, W., and Filippenko, A. V. 2009. Supernova 2009ig in NGC 1015. *Central Bureau for Astronomical Telegrams 1918*, 1.

Krause, O., Tanaka, M., Usuda, T., Hattori, T., Goto, M., Birkmann, S., and Nomoto, K. 2008. Tycho Brahe's 1572 supernova as a standard type Ia as revealed by its light-echo spectrum. *Nature 456*, 617–619.

Lair, J. C., Leising, M. D., Milne, P. A., and Williams, G. G. 2006. Late Light Curves of Normal Type Ia Supernovae. *Astronomical Journal 132*, 2024–2033.

Landolt, A. U. 1992. UBVRI photometric standard stars in the magnitude range 11.5-16.0 around the celestial equator. *Astronomical Journal 104*, 340–371.

Lee, M. G. and Jang, I. S. 2013. The Tip of the Red Giant Branch Distances to Type Ia Supernova Host Galaxies. II. M66 and M96 in the Leo I Group. *Astrophysical Journal 773*, 13.

Marion, G. H., Sand, D. J., Hsiao, E. Y., Banerjee, D. P. K., Valenti, S., Stritzinger, M. D., Vinkó, J., Joshi, V., Venkataraman, V., Ashok, N. M., Amanullah, R., Binzel, R. P., Bochanski, J. J., Bryngelson, G. L., Burns, C. R., Drozdov, D., Fieber-Beyer, S. K., Graham, M. L., Howell, D. A., Johansson, J., Kirshner, R. P., Milne, P. A., Parrent, J., Silverman, J. M., Vervack, Jr., R. J., and Wheeler, J. C. 2015. Early Observations and Analysis of the Type Ia SN 2014J in M82. *Astrophysical Journal 798*, 39.

Marion, G. H., Vinko, J., Wheeler, J. C., Foley, R. J., Hsiao, E. Y., Brown, P. J., Challis, P., Filippenko, A. V., Garnavich, P., Kirshner, R. P., Landsman, W. B., Parrent, J. T., Pritchard, T. A., Roming, P. W. A., Silverman, J. M., and Wang, X. 2013. High-velocity Line Forming Regions in the Type Ia Supernova 2009ig. *Astrophysical Journal 777*, 40.

Matheson, T., Kirshner, R. P., Challis, P., Jha, S., Garnavich, P. M., Berlind, P., Calkins, M. L., Blondin, S., Balog, Z., Bragg, A. E., Caldwell, N., Dendy Concannon, K., Falco, E. E., Graves, G. J. M., Huchra, J. P., Kuraszkiewicz, J., Mader, J. A., Mahdavi, A., Phelps, M., Rines, K., Song, I., and Wilkes, B. J. 2008. Optical Spectroscopy of Type ia Supernovae. *Astronomical Journal 135*, 1598–1615.

Mazzali, P. A., Benetti, S., Altavilla, G., Blanc, G., Cappellaro, E., Elias-Rosa, N., Garavini, G., Goobar, A., Harutyunyan, A., Kotak, R., Leibundgut, B., Lundqvist, P., Mattila, S., Mendez, J., Nobili, S., Pain, R., Pastorello, A., Patat, F., Pignata, G., Podsiadlowski, P., Ruiz-Lapuente, P., Salvo, M., Schmidt, B. P., Sollerman, J., Stanishev, V., Stehle, M., Tout, C., Turatto, M., and Hillebrandt, W. 2005. High-Velocity Features: A Ubiquitous Property of Type Ia Supernovae. *Astrophysical Journal, Letters 623*, L37–L40.

Meikle, P. and Hernandez, M. 2000. Infrared and optical study of the type Ia SN 1998bu in M96. *Mem. Societa Astronomica Italiana 71*, 299–306.

Miller, A. A., Smith, N., Li, W., Bloom, J. S., Chornock, R., Filippenko, A. V., and Prochaska, J. X. 2010. New Observations of the Very Luminous Supernova 2006gy: Evidence for Echoes. *Astronomical Journal 139*, 2218–2229.

Milne, P. A., Brown, P. J., Roming, P. W. A., Bufano, F., and Gehrels, N. 2013. Grouping Normal Type Ia Supernovae by UV to Optical Color Differences. *Astrophysical Journal 779*, 23.

Milne, P. A., The, L.-S., and Leising, M. D. 1999. Positron Escape from Type IA Supernovae. *Astrophysical Journal, Supplement 124*, 503–526.

Munari, U., Barbon, R., Tomasella, L., Rejkuba, M., Evans, R., Wild, W., Boschini, L., Hanzl, D., Masi, G., Baransky, A., Hornoch, K., Monard, B., and Kiss, L. 1998. Supernova 1998bu in NGC 3368. *International Astronomical Union Circulars 6902*, 1.

Nobili, S. and Goobar, A. 2008. The colour-lightcurve shape relation of type Ia supernovae and the reddening law. *Astronomy and Astrophysics 487*, 19–31.

Nomoto, K., Thielemann, F.-K., and Yokoi, K. 1984. Accreting white dwarf models of Type I supernovae. III - Carbon deflagration supernovae. *Astrophysical Journal 286*, 644–658.

Nugent, P., Kim, A., and Perlmutter, S. 2002. K-Corrections and Extinction Corrections for Type Ia Supernovae. *Publications of the Astronomical Society of the Pacific 114*, 803–819.

Patat, F. 2003. Light Echoes in Type Ia Supernovae. In *From Twilight to Highlight: The Physics of Supernovae*, W. Hillebrandt and B. Leibundgut, Eds. 321.

Patat, F. 2005. Reflections on reflexions i. light echoes in type ia supernovae. *Monthly Notices of the Royal Astronomical Society 357,* 4, 1161–1177.

Patat, F., Benetti, S., Cappellaro, E., and Turatto, M. 2006. Reflections on reflexions - II. Effects of light echoes on the luminosity and spectra of Type Ia supernovae. *Monthly Notices of the Royal Astronomy 369*, 1949–1960.

Patat, F., Chandra, P., Chevalier, R., Justham, S., Podsiadlowski, P., Wolf, C., Gal-Yam, A., Pasquini, L., Crawford, I. A., Mazzali, P. A., Pauldrach, A. W. A., Nomoto, K., Benetti, S., Cappellaro, E., Elias-Rosa, N., Hillebrandt, W., Leonard, D. C., Pastorello, A., Renzini, A., Sabbadin, F., Simon, J. D., and Turatto, M. 2007. Detection of Circumstellar Material in a Normal Type Ia Supernova. *Science 317*, 924–.

Perlmutter, S., Aldering, G., Goldhaber, G., Knop, R. A., Nugent, P., Castro, P. G., Deustua, S., Fabbro, S., Goobar, A., Groom, D. E., Hook, I. M., Kim, A. G., Kim, M. Y., Lee, J. C., Nunes, N. J., Pain, R., Pennypacker, C. R., Quimby, R., Lidman, C., Ellis, R. S., Irwin, M., McMahon, R. G., Ruiz-Lapuente, P., Walton, N., Schaefer, B., Boyle, B. J., Filippenko, A. V., Matheson, T., Fruchter, A. S., Panagia, N., Newberg, H. J. M., Couch, W. J., and Supernova Cosmology Project. 1999. Measurements of Omega and Lambda from 42 High-Redshift Supernovae. *Astrophysical Journal 517*, 565–586.

Phillips, M. M., Lira, P., Suntzeff, N. B., Schommer, R. A., Hamuy, M., and Maza, J. 1999. The Reddening-Free Decline Rate Versus Luminosity Relationship for Type IA Supernovae. *Astronomical Journal 118*, 1766–1776.

Planck Collaboration, Ade, P. A. R., Aghanim, N., Armitage-Caplan, C., Arnaud, M., Ashdown, M., Atrio-Barandela, F., Aumont, J., Baccigalupi, C., Banday, A. J., and et al. 2014. Planck 2013 results. XVI. Cosmological parameters. *Astronomy and Astrophysics 571*, A16.

Quimby, R., Brown, P., Gerardy, C., Odewahn, S. C., and Rostopchin, S. 2006. Supernova 2006X in NGC 4321. *Central Bureau Electronic Telegrams 393*, 1.

Quinn, J. L., Garnavich, P. M., Li, W., Panagia, N., Riess, A., Schmidt, B. P., and Della Valle, M. 2006. A Light Echo from Type Ia SN 1995E? *Astrophysical Journal 652*, 512–517.

Rest, A., Foley, R. J., Sinnott, B., Welch, D. L., Badenes, C., Filippenko, A. V., Bergmann, M., Bhatti, W. A., Blondin, S., Challis, P., Damke, G., Finley, H., Huber, M. E., Kasen, D., Kirshner, R. P., Matheson, T., Mazzali, P., Minniti, D., Nakajima, R., Narayan, G., Olsen, K., Sauer, D., Smith, R. C., and Suntzeff, N. B. 2011. Direct Confirmation of the Asymmetry of the Cas A Supernova with Light Echoes. *Astrophysical Journal 732*, 3.

Rest, A., Matheson, T., Blondin, S., Bergmann, M., Welch, D. L., Suntzeff, N. B., Smith, R. C., Olsen, K., Prieto, J. L., Garg, A., Challis, P., Stubbs, C., Hicken, M., Modjaz, M., Wood-Vasey, W. M., Zenteno, A., Damke, G., Newman, A., Huber, M., Cook, K. H., Nikolaev, S., Becker, A. C., Miceli, A., Covarrubias, R., Morelli, L., Pignata, G., Clocchiatti, A., Minniti, D., and Foley, R. J. 2008. Spectral Identification of an Ancient Supernova Using Light Echoes in the Large Magellanic Cloud. *Astrophysical Journal 680*, 1137–1148.

Rest, A., Prieto, J. L., Walborn, N. R., Smith, N., Bianco, F. B., Chornock, R., Welch, D. L., Howell, D. A., Huber, M. E., Foley, R. J., Fong, W., Sinnott, B., Bond, H. E., Smith, R. C., Toledo, I., Minniti, D., and Mandel, K. 2012. Light echoes reveal an unexpectedly cool ηCarinae during its nineteenth-century Great Eruption. *Nature 482*, 375–378.

Rest, A., Suntzeff, N. B., Olsen, K., Prieto, J. L., Smith, R. C., Welch, D. L., Becker, A., Bergmann, M., Clocchiatti, A., Cook, K., Garg, A., Huber, M., Miknaitis, G., Minniti, D., Nikolaev, S., and Stubbs, C. 2005. Light echoes from ancient supernovae in the Large Magellanic Cloud. *Nature 438*, 1132–1134.

Riess, A. G., Filippenko, A. V., Challis, P., Clocchiatti, A., Diercks, A., Garnavich, P. M., Gilliland, R. L., Hogan, C. J., Jha, S., Kirshner, R. P., Leibundgut, B., Phillips, M. M., Reiss, D., Schmidt, B. P., Schommer, R. A., Smith, R. C., Spyromilio, J., Stubbs, C., Suntzeff, N. B., and Tonry, J. 1998. Observational Evidence from Supernovae for an Accelerating Universe and a Cosmological Constant. *Astronomical Journal 116*, 1009–1038.

Riess, A. G., Macri, L., Casertano, S., Lampeitl, H., Ferguson, H. C., Filippenko, A. V., Jha, S. W., Li, W., and Chornock, R. 2011. A 3% Solution: Determination of the Hubble Constant with the Hubble Space Telescope and Wide Field Camera 3. *Astrophysical Journal 730*, 119.

Romaniello, M., Patat, F., Panagia, N., Sparks, W. B., Gilmozzi, R., and Spyromilio, J. 2005. Very Large Telescope FORS1 Imaging Polarimetry of M83 (NGC 5236). I. Search for Light Echoes from Historical Supernovae. *Astrophysical Journal 5*, 250–258.

Saha, A., Sandage, A., Thim, F., Labhardt, L., Tammann, G. A., Christensen, J., Panagia, N., and Macchetto, F. D. 2001. Cepheid Calibration of the Peak Brightness of Type IA Supernovae. X. SN 1991T in NGC 4527. *Astrophysical Journal 551*, 973–1015.

Schmidt, B. P., Kirshner, R. P., Leibundgut, B., Wells, L. A., Porter, A. C., Ruiz-Lapuente, P., Challis, P., and Filippenko, A. V. 1994. SN 1991T: Reflections of past glory. *Astrophysical Journal, Letters 434*, L19–L23.

Simon, J. D., Gal-Yam, A., Penprase, B. E., Li, W., Quimby, R. M., Silverman, J. M., Allende Prieto, C., Wheeler, J. C., Filippenko, A. V., Martinez, I. T., Beeler, D. J., and Patat, F. 2007. Constraints on Circumstellar Material around the Type Ia Supernova 2007af. *Astrophysical Journal, Letters 671*, L25–L28.

Sirianni, M., Jee, M. J., Benítez, N., Blakeslee, J. P., Martel, A. R., Meurer, G., Clampin, M., De Marchi, G., Ford, H. C., Gilliland, R., Hartig, G. F., Illingworth, G. D., Mack, J., and McCann, W. J. 2005. The Photometric Performance and Calibration of the Hubble Space Telescope Advanced Camera for Surveys. *Publications of the Astronomical Society of the Pacific 117*, 1049–1112.

Sollerman, J., Lindahl, J., Kozma, C., Challis, P., Filippenko, A. V., Fransson, C., Garnavich, P. M., Leibundgut, B., Li, W., Lundqvist, P., Milne, P., Spyromilio, J., and Kirshner, R. P. 2004. The late-time light curve of the type Ia supernova 2000cx. *Astronomy and Astrophysics 428*, 555–568.

Sparks, W. B. 1994. A direct way to measure the distances of galaxies. *Astrophysical Journal 433*, 19–28.

Sparks, W. B. 1996. Geometric Distance Measurement. II. *Astrophysical Journal 470*, 195.

Sparks, W. B., Macchetto, F., Panagia, N., Boffi, F. R., Branch, D., Hazen, M. L., and Della Valle, M. 1999. Evolution of the Light Echo of SN 1991T. *Astrophysical Journal 523*, 585–592.

Sugerman, B. E. K. 2003. Observability of Scattered-Light Echoes around Variable Stars and Cataclysmic Events. *Astronomical Journal 126*, 1939–1959.

Suntzeff, N. B. 1996. Observations of Type IA Supernovae. In *International Astronomical Union Colloquia 145: Supernovae and Supernova Remnants*, T. S. Kuhn, Ed. 41.

Suntzeff, N. B., Phillips, M. M., Covarrubias, R., Navarrete, M., Pérez, J. J., Guerra, A., Acevedo, M. T., Doyle, L. R., Harrison, T., Kane, S., Long, K. S., Maza, J., Miller, S., Piatti, A. E., Clariá, J. J., Ahumada, A. V., Pritzl, B., and Winkler, P. F. 1999. Optical Light Curve of the Type IA Supernova 1998BU in M96 and the Supernova Calibration of the Hubble Constant. *Astrophysical Journal 117*, 1175–1184.

Suzuki, S. and Magliardi, M. 2006. IAUC. *International Astronomical Union Circulars 8667*.

Tanaka, M., Mazzali, P. A., Benetti, S., Nomoto, K., Elias-Rosa, N., Kotak, R., Pignata, G., Stanishev, V., and Hachinger, S. 2008. The Outermost Ejecta of Type Ia Supernovae. *Astrophysical Journal 677*, 448–460.

Tody, D. 1986. The IRAF Data Reduction and Analysis System. In *Instrumentation in astronomy VI*, D. L. Crawford, Ed. Society of Photo-Optical Instrumentation Engineers (SPIE) Conference Series, vol. 627. 733.

Tsvetkov, D. Y., Shugarov, S. Y., Volkov, I. M., Goranskij, V. P., Pavlyuk, N. N., Katysheva, N. A., Barsukova, E. A., and Valeev, A. F. 2013. Optical observations of SN 2011fe. *Contributions of the Astronomical Observatory Skalnate Pleso 43*, 94–108.

Tylenda, R. 2004. On the light echo in V838 Mon. *Astronomy and Astrophysics 414*, 223–233.

Villi, M., Nakano, S., Aoki, M., Skiff, B. A., and Hanzl, D. 1998. Supernova 1998bu in NGC 3368. *International Astronomical Union Circulars 6899*, 1.

Wang, L. 2005. Dust around Type Ia Supernovae. *Astrophysical Journal, Letters 635*, L33–L36.

Wang, X., Li, W., Filippenko, A. V., Foley, R. J., Kirshner, R. P., Modjaz, M., Bloom, J., Brown, P. J., Carter, D., Friedman, A. S., Gal-Yam, A., Ganeshalingam, M., Hicken, M., Krisciunas, K., Milne, P., Silverman, J. M., Suntzeff, N. B., Wood-Vasey, W. M., Cenko, S. B., Challis, P., Fox, D. B., Kirkman, D., Li, J. Z., Li, T. P., Malkan, M. A., Moore, M. R., Reitzel, D. B., Rich, R. M., Serduke, F. J. D., Shang, R. C., Steele, T. N., Swift, B. J., Tao, C., Wong, D. S., and Zhang, S. N. 2009. The Golden Standard Type Ia Supernova 2005cf: Observations from the Ultraviolet to the Near-Infrared Wavebands. *Astrophysical Journal 697*, 380–408.

Wang, X., Li, W., Filippenko, A. V., Foley, R. J., Smith, N., and Wang, L. 2008. The Detection of a Light Echo from the Type Ia Supernova 2006X in M100. *Astrophysical Journal 677*, 1060–1068.

Wang, X., Li, W., Filippenko, A. V., Krisciunas, K., Suntzeff, N. B., Li, J., Zhang, T., Deng, J., Foley, R. J., Ganeshalingam, M., Li, T., Lou, Y., Qiu, Y., Shang, R., Silverman, J. M., Zhang, S., and Zhang, Y. 2008. Optical and Near-Infrared Observations of the Highly Reddened, Rapidly Expanding Type Ia Supernova SN 2006X in M100. *Astrophysical Journal 675*, 626–643.

Yamanaka, M., Naito, H., Kinugasa, K., Takanashi, N., Tanaka, M., Kawabata, K. S., Ozaki, S., Narusawa, S.-Y., and Sadakane Kozo. 2009. Early Spectral Evolution of the Rapidly Expanding Type Ia Supernova 2006X. *Publications of the Astronomical Society of the Pacific 61*, 713–.

Yaron, O. and Gal-Yam, A. 2012. WISeREP - An Interactive Supernova Data Repository. *Publications of the Astronomical Society of the Pacific 124*, 668–681.